Numerical study of a confined thermal plume at different flow regimes under the influence of gas radiation

Ying Wang

La Rochelle Université

ÉCOLE DOCTORALE
EUCLIDE

Laboratoire des Sciences de l'Ingénieur pour l'Environnement (LaSIE)

THÈSE

présentée par :

Ying WANG

Soutenue le 24 Février 2020
pour l'obtention du grade de Docteur de La Rochelle Université

Spécialité : Énergétique et Thermique

Numerical study of a confined thermal plume at different flow regimes under the influence of gas radiation

JURY :

M. Eric CHÉNIER	MCF HdR, Université Gustave Eiffel, Rapporteur
M. Shihe XIN	Professeur, INSA de Lyon, Rapporteur
M. Patrick Le QUÉRÉ	DR-CNRS, LIMSI-Orsay, Examinateur
M. Didier SAURY	Professeur, ISAE-ENSMA, Examinateur
M. Laurent SOUCASSE	MCF, CentraleSupélec, Université Paris Saclay, Examinateur
Mme Anne SERGENT	MCF HdR, LIMSI-Sorbonne Université, Co-directrice
M. Patrice JOUBERT	Professeur, La Rochelle Université, Directeur de thèse
M. Denis LEMONNIER	DR-CNRS, ISAE-ENSMA, Co-directeur

La Rochelle Université
Laboratoire LaSIE
UMR CNRS 7356, Avenue Michel Crépeau, 17042 La Rochelle Cedex 1 - France

Acknowledgement

I am very much pleased to acknowledge some people who deserve special mention for their assistance and support in the development of this work in various ways.

My thanks go firstly to my supervisor, Prof. Patrice JOUBERT in La Rochelle, for his imparted knowledge, kind assistance, and regular suggestions during the completion of this work. Without his enlightening instruction, impressive kindness and patience, I could not complete my thesis. Secondly, I am very pleased to thank my co-supervisor, Mrs. Anne SERGENT (MCF HdR in Paris), for her useful advices in numerical aspects and for providing me with many valuable comments on this work. Thirdly, I would thank to Prof. Didier SAURY in Poitiers, who is not in the official supervision team, but has followed my thesis for three years and provided essential support. Fourthly, I am very grateful to thank my co-director, Mr. Denis Lemonnier (DNRS Director in Poitiers) for his support in understanding the domain of thermal radiation. I will never forget his important help when I started my PhD study and his proposal on this thesis subject.

I want to acknowledge IDRIS, the French national supercomputing center, without which it would not be possible to perform the large calculations in this work. I would also thank Dr. Y. Fraigneau (Research engineer in LIMISI) for his help in using the code SUNFLUIDH, and Dr. L. Cadet for his assistance in the radiative module and for guiding me to master the numerical code.

I am thankful to my colleagues in the laboratory for their help in my study and happy time together. I also express my thanks to all my Chinese friends in France who encouraged and supported me in these three years. Because of your company, I didn't feel lonely even during some traditional Chinese festivals.

Finally, thanks to my sponsors, the China Scholarship Council (CSC) and the Civil Aviation University of China (CAUC) who financially supported me throughout this study so that I can have this wonderful experience in France. And on a personal note, the most important thanks to my parents for consistently encouraging me to be brave, independent and optimistic, and I appreciate your support and love in these years.

Ying WANG

January 2020

Contents

Nomenclature

Roman symbols

a	Weighting factor
C	Absorption cross-section [$m^2.mol^{-1}$]
c_p	Thermal capacity at constant pressure [$J.kg^{-1}.K^{-1}$]
E_b	Integrated blackbody emissive power [$W.m^{-2}.sr^{-1}$]
F	Absorption-line blackbody distribution function
f	Dimensionless oscillating frequency [-]
G	Incident radiative flux [$W.m^{-2}$]
g	Gravity acceleration [$m.s^{-2}$]
H	Domain size [m] or hemispherical irradiation [$W.m^{-2}$]
h	Dipole height [-]
I	Total radiative intensity [$W.m^{-2}.sr^{-1}$]
k	Wave number [-]
N	Molar density [$mol.m^{-3}$]
N_g	Total number of gray gases [-]
Nu	Nusselt number [-]
$\boldsymbol{n}$	Surface normal unit vector [-]
Pl	Planck number [-]
Pr	Prandtl number [-]
p	Pressure [Pa]
Q'	Energy source term per unit length [$W.m^{-1}$]
Q'''	Energy source term per unit volume [$W.m^{-3}$]
Q_r^{net}	Net radiative flux at the walls [$W.m^{-2}$]
q_r^{net}	Dimensionless net radiative flux at the walls [-]

Ra	Rayleigh number [-]
Re	Reynolds number [-]
S	Strain-rate tensor [-]
$\boldsymbol{s}$	Propagation direction unit vector [-]
T	Temperature [K]
t	Dimensionless time [-]
U , V , W	Velocity components [$m.s^{-1}$]
u , v , w	Dimensionless velocity components [-]
X , Y , Z	Cartesian coordinates [m]
X_a	Molar fraction of water vapor in air
x , y , z	Dimensionless cartesian coordinates [-]

Greek symbols

α	Thermal diffusivity [$m^2.s^{-1}$]
β	Temperature expansion coefficient [K^{-1}] or extinction coefficient [m^{-1}]
Δ	Indicator for scaled temperature or cell size
δ	Change of quantity [-]
ε	Emissivity [-]
η_k	Kolmogorov scale [-]
Θ_0	Temperature ratio [-]
θ	Dimensionless temperature [-]
κ	Absorption coefficient [m^{-1}]
λ	Thermal conductivity [$W.m^{-1}.K^{-1}$]
μ	Dynamic viscosity [$kg.m^{-1}.s^{-1}$]
μ, η, ξ	Cosines directors of the propagation direction
ν	Kinematic viscosity [$m^2.s^{-1}$]
ξ	Kinetic dissipation rate [$m^2.s^{-3}$]
ρ	Mass density [$kg.m^{-3}$]

σ	Scattering coefficient [m^{-1}]
σ_B	Stefan-Boltzmann constant [$W.m^2.K^{-4}$]
τ	Optical thickness [-]
τ_{ij}	Viscous stress tensor [$N.m^{-2}$]
Φ	Scattering phase function or amplitude of perturbation [-]
φ_s'''	Dimensionless line source per unit volume [-]
φ_r'''	Dimensionless volumetric radiative power [-]
ψ	Dimensionless radiative temperature [-] or stream function [-]
Ω	Solid angle [sr] or vorticity tensor [-]
ω	Quadrature weight or vorticity [-]

Superscript

*	Normalized quantities
^{b}	Blackbody
$\overline{\cdot}$	Time averaged quantities
$'$	Fluctuating quantities

Subscript

$_{BV}$	Brunt Väisälä
$_{bot}$	Relative to the bottom wall
$_c$	Critical value or relative to the convective term
$_r$	Relative to the radiative term
$_{ref}$	Reference quantities
$_{top}$	Relative to the top wall
$_\nu$	Spectral quantities
$_w$	Quantities at the walls

$_{rms}$	Root mean square

Abbreviations

CFL	Courant-Fredrichs-Lewy
DNS	Direct Numerical simulation
DOM	Discrete Ordinates Method
LES	Large Eddy Simulation
PDF	Probability Density Function
RANS	Reynolds-Averaged Navier-Stokes equations
RTE	Radiative Transfer Equation
SLW	Spectral-Line based Weighted-sum-of-gray-gases

List of figures

List of tables

Introduction

General framework and motivation

Natural convection is a buoyancy-induced flow, arising from spatial density differences within a fluid. These density differences are mainly due to inhomogeneities in temperature and variations in species concentration. A thermal plume is one type of natural convection flow that is generated from a heat source. It can be found in many natural and artificial phenomena, such as smoke plume from fire, air circulation around human body, atmospheric circulations, and many engineering applications ranging from electronics cooling, heat storage in boilers, to nuclear reactors safety technologies, etc.

Due to its relevance to many engineering applications, researches on thermal plume flows have received great attention. However, most of these works only consider pure convective plumes. If the working fluid is a radiative participating medium, this can affect plume behavior by the emission and the absorption of radiation, making the flow more complex. The lack of results in the study of three-dimensional plumes considering convection-radiation coupling, especially in the turbulent state, reflects the difficulty of these problems. In order to characterize the thermal fields and flow dynamics of plume and to understand the influence of gas radiation, it is necessary to study natural convection coupled with the radiative heat transfer for a thermal plume. We propose in this thesis to investigate numerically the convection-radiation coupling of thermal plumes throughout its transition from steady to turbulent states.

Literature review of pure convective plumes

The case of a fully developed buoyant plume in unbounded space has been extensively investigated in the past, both for plumes originating from a point source as well as plane plumes generated by a line source. In a pioneering work, Zeldovich (1937) described the natural convective plumes arising from a point and from a horizontal line source of heat. Later on, the classical self-similar solutions for laminar flow velocities and temperature have been proposed in early theoretical studies to describe such natural convective flows (Lyakhov, 1970; Schorr & Gebhart, 1970; Fujii et al., 1973). During the same period, many experiments have been carried out and the experimental results were found to be in good agreement with the laminar theory of plume. Numerical simulations of unbounded plumes were also

performed in the past. Liñán and Kurdyumov (1998), as an example, investigated numerically laminar natural convection above a line source and used far field analytical expression to impose the boundary conditions on the limits of the computational domain. This is a limited approach because it needs the *a priori* knowledge of the flow under study. In order to avoid this difficulty, Xin et al. (2004) proposed a general formulation based on the balance between pressure and friction forces at the outer border of the computational domain, independent of the nature of the flow. This allows dealing with unsteady flow and was validated by experiments.

Free plume flows are much less stable when compared to the flows adjacent to surface which can damp disturbances (Gebhart et al., 1988). The experiment of Forstrom and Sparrow (1966), performed on a buoyant plume above a heated horizontal wire, showed that the laminar plume exhibits a slow, regular swaying motion in the plane perpendicular to the heater. Later on, Pera and Gebhart (1971) investigated numerically the stability of a laminar plume above a linear heat source and validated these stability predictions experimentally. The water experiments of Eichhorn and Vedhanayagam (1982) as well as the spindle oil experiments of Urakawa et al. (1983) showed that the buoyant plume not only sways in the plane perpendicular to the heater but also meanders along the heater direction. In addition, Urakawa et al. found that the meandering wave shape is stable when the heater length is an integral multiple of half the wave length.

As for turbulent plume in unbounded space, Schmidt (1941) studied analytically the plume behaviors by using the similarity technique and conducted experiments above an electrically heat wire. Rouse et al. (1952) studied the characteristics of the mean flow through measurements of velocity and temperature distribution above a line of small gas flames. In the works of Turner (1986), the entrainment assumption was applied to establish an integral (similarity) model for velocity and temperature fields. This assumption relates the mean inflow velocity across the edge of a turbulent flow to the local time-averaged maximum mean velocity or the mean velocity over the cross-section at the level of inflow. Gebhart et al. (1988) collected an account of instability, transition, and turbulent transport of buoyancy-induced flow.

More recently, there is a growing interest in plumes developing in a confined enclosure. Confined plumes are very complex flows due to their sensitivity to the presence of the walls and the generated thermal stratification of the fluid, and therefore can present strong intermittency (Hernández, 2015). Because of the confinement, it is quite difficult to find a general analytical approach, so numerical simulations or experiments are more commonly used to study such flows. Desrayaud and Lauriat (1993) investigated numerically plumes in air above a linear heat source in a 2D enclosure with various aspect ratios and depths of the immersion of the source. They determined the transitions of plume flows through Hopf or pitchfork bifurcations, and the critical Rayleigh number was determined by a linear

extrapolation method. They also found that in the case of a heat source near the bottom wall of a square vessel, the swaying motion of the plume begins with a periodic regime having a high fundamental frequency followed by a two-frequency locked regime. In the same configuration, Bastiaans et al. (2000) obtained a more accurate value for the critical Rayleigh number of 2D plume with a spectral element method.

Following these studies, Fiscaletti et al. (2013) investigated transitional plumes within a water-filled tank around an horizontal cylinder by means of experiment and numerical simulation. The evolution of the flow throughout the bifurcation is described in their work and the swaying motion is evidenced by 2D visualization. On their side, Hernández (2015) studied numerically the steady and periodic states of thermal plume in a slender air cavity with a linear source on the floor of the cavity. They observed that the 3D plume oscillates with the same spatial phase in all the transverse planes along the source direction, with a slight modulation of the vertical expansion of plume. They suggested that this lock-in mode can be broken for Rayleigh numbers higher than the one they considered, and/or for higher longitudinal aspect ratios.

Concerning turbulent simulations, not much information is available on thermal plumes in an entirely confined enclosure. Only in the works of Bastiaans et al. (2000), which were performed on a 3D turbulent plume in a confined environment. Results were obtained by both DNS and LES, and showed that the buoyancy force strongly affects the turbulence production and evolution process. Numerical studies of turbulent plumes in other configurations are better documented in the literature, for example, forced turbulent plume induced by an injected hot air (Zhou et al., 2001; Yan, 2007), pure thermal plume arising from a heated finite size source in an open space (Pham et al., 2007); thermal plume generated by a point heat source in a ventilated enclosure (Abdalla et al., 2009), buoyant plume above an unbounded heated horizontal cylinder (Grafsrønningen & Jensen, 2017), and so on.

Influence of radiation

The above-mentioned works only considers thermal plumes in a transparent medium. To the authors knowledge, the existing works show a lack of investigation for thermal plume in presence of gas radiation. On the other hand, influence of participating media has been widely investigated in other natural convection configurations, such as the differentially heated cavity.

- **Gas radiation in gray media**

In a pioneering work (Lauriat, 1982) investigated numerically the convection-radiation coupling in a gray fluid contained inside a 2D slender cavity. Results show that radiation

decreases the flow intensity at low Rayleigh numbers ($Ra < 10^3$) and, in contrast, leads to an enhance of the flow at higher Rayleigh numbers ($Ra > 10^4$). They also discussed influences of the optical thickness on the flow and heat transfer. Later on, Draoui et al. (1991) using the gray gas assumption studied the influence of the radiative governing paramenters (Pl, τ, ε) in a square cavity at various Rayleigh numbers. They found that the diminution of the Planck number increases the dynamical effects in the central part of the cavity, thickens the boundary layers and decreases the thermal stratification, proving that gas radiation has an important influence on the temperature field and the fluid movement.

Following their studies, Colomer et al. (2004) carried out a 3D numerical simulation of convection and radiation in a differentially heated cavity. They showed that the heat flux increases as the Rayleigh number increases. On the other hand, an increase of the optical thickness causes a decrease of the heat flux. They found that the limit of an optically very thick medium tends to the case where radiation becomes a local phenomenon and can be described with the Rosseland/diffusion approximation. In addition, their study compares the temperature fields of a 2D calculation with those extracted at mid-depth of the 3D configuration. The comparison shows a very good agreement between these two configurations, and proves that the front and rear walls have a negligible effect on the center of the cavity for aspect ratios $L_y / H \geq 1$.

The effects of the optical thickness were also studied by Lari et al. (2011) in a large range from $\tau = 0$ to 100. They observed that, at a constant Ra number ($Ra = 10^6$), radiation is the dominant mode of heat transfer for optically thin media ($\tau < 1$), but the phenomenon reverses with the increase of τ until the limit of optically thick medium where the pure convection condition is again approached for both the thermal features and the velocity field. They also found that the velocity distributions decrease with the optical thickness for $10^2 < Ra < 10^3$, but increase for $10^4 < Ra < 10^6$, as described by Lauriat (1982).

- **Gas radiation in real gas**

Recently, many works (Colomer et al., 2007; Saury et al., 2011; Soucasse et al., 2012; Ibrahim et al., 2013; Soucasse et al., 2016; Billaud et al., 2017) have been focused on the coupling of convection and radiation in a real gas mixture. Colomer et al. (2007) investigated the coupling in a square cavity filled with a gas mixture of air, CO_2 and H_2O. They studied different absorption coefficient approaches in using the Spectral Line Weighted-sum-of-gray-gases (SLW) real gas model, and compared the non-gray calculations to gray solutions through the Planck mean absorption coefficient. It is shown that the Planck mean approximation gives the worse results compared to non-gray models. The use of optimized coefficients was then recommended by the authors in order to reduce the number of calculations.

Soucasse et al. (2012) performed a coupled study in a cubic cavity of size equals to 1 m and filled with an air/CO_2/H_2O mixture at a reference temperature of 300 K. Simulations carried out at various Rayleigh numbers ($Ra = 10^5$, 10^6 and 3×10^7) showed that radiative transfer has a strong influence on the temperature and velocity fields.

In the same configuration, Cadet (2015) studied the convection-radiation coupling by using an air/ H_2O mixture at a Rayleigh number equal to 4×10^{10}. He found that gas radiation tends to homogenize the mean temperature field but to intensify the mean circulation and the global turbulence level. Later on, Soucasse et al. (2016) carrying out coupled simulations at Rayleigh numbers up to 3×10^9, observed the same effect of gas radiation on the mean and the fluctuating fields in the cavity. They also found that gas and wall radiative transfers changes drastically the spatial location of intense turbulent regions.

The work of Ibrahim et al. (2013) dealt with the influence of radiation on natural convection flows in a 2D square cavity with a gas mixture of dry air and water vapor. They found that wall radiation modifies the airflow structure, and in contrast that gas radiation has little influence on the flow structure. Results showed that gas radiation delays the transition to turbulence by the homogenization of the temperature field and the reduction of the central thermal stratification within the cavity.

Billaud et al. (2017) performed a study of convection and radiation in a cubic cavity of air/H_2O mixture at $Ra = 10^6$. Their results were compared with those of Soucasse et al. (2012), and the relative error was found to be less than 2% although the absorbing gas CO_2 is not taken into account, contrarily to the work of Soucasse et al.. Billaud et al. also discussed the effect of the cavity size, which has a strong influence on the temperature and velocity fields of the participating medium in terms of global heat transfer, boundary layer thickness and thermal stratification parameter.

These different works mentioned above show that gas radiation strongly affects the thermal and kinetic fields of air flow, even for air at ambient temperature and low water vapor content. This indicates that gas radiation effects cannot be neglected in natural convection configurations.

Objectives

This study consists in a numerical investigation of convection-radiation coupling of thermal plumes above a line heat source in a confined cavity. The objectives include:

1. To characterize the evolution of a 3D confined plume throughout its transition from steady-state to turbulent behavior.
2. To discuss the plume features in different gas media: transparent, gray gas and real gas mixture.

3. To explore gas radiation effects on flow stability, heat transfers, thermal and kinetic fields of the plume.

The structure of this manuscript is organized as follows:

- **Chapter 1**

After an overview of the physical problem under consideration, the governing equations for the convective and radiative problems are presented with their associated non-dimensional formulations. Various approaches to represent the radiative properties of gas are specified, especially the SLW model.

- **Chapter 2**

The numerical methods for solving the convection governing equations and the radiative transfer equation are introduced in this chapter. We use the CFD SUNFLUIDH software coupled to a module for radiative heat transfer calculations, using the Discrete Ordinates Method (DOM). The numerical procedure is validated with reference to existing results, first for a confined 2D plume in a pure convective case, then for coupled convection-radiation problems in a differentially heated cavity.

- **Chapter 3**

Results of a 3D plume in pure convective case are discussed for Rayleigh numbers between 10^6 and 10^9. We focus our attention on the evolution of a thermal plume throughout the transition from steady-state to turbulent behavior to characterize the thermal and kinetic properties of plumes at different flow regimes.

- **Chapter 4**

The influence of gas radiation is finally investigated by introducing different gaseous media: gray gases with various optical thickness and a real gas considering a (dry air - water vapor) mixture. Simulations are performed in the same range of Rayleigh numbers as for the pure convective case. The governing parameters (the Rayleigh number, the optical thickness, the reference temperature and the water vapor concentration) are varied to emphasize radiation effects on flow regimes, heat transfers, thermal and kinetic fields of the flow.

Chapter 1
Physical problem and governing equations

1.1 Problem description

The considered geometry is presented in Figure 1.1. It corresponds to an air-filled cubic cavity of size H. A thermal plume is induced by an immersed heat source along the line $(X,\ Y, Z) = (0.5H,\ Y, 0.25H)$, indicated in red in Figure 1.1. This is the configuration considered by Desrayaud and Lauriat (1993) and Bastiaans et al. (2000). The heat source is considered to be intangible and generates a volumetric power Q_s' by unit length. The top wall $(Z = H)$ and the bottom wall $(Z = 0)$ are maintained at the reference temperature T_{ref}, while the four vertical walls are considered to be adiabatic.

For the pure convective case, a transparent medium is considered and there is no surface radiative effect. When radiation is accounted for, the horizontal top and bottom walls are supposed to be black surfaces ($\varepsilon = 1$, with ε the wall emissivity), while the vertical walls are purely reflecting ($\varepsilon = 0$). When dealing with radiative participating media, we first consider a fictitious gray gaseous medium whose optical thickness (τ) is varied, then a mixture of real gases (dry air - water vapor) with a molar fraction (X_a) of H_2O fixed over the whole cavity.

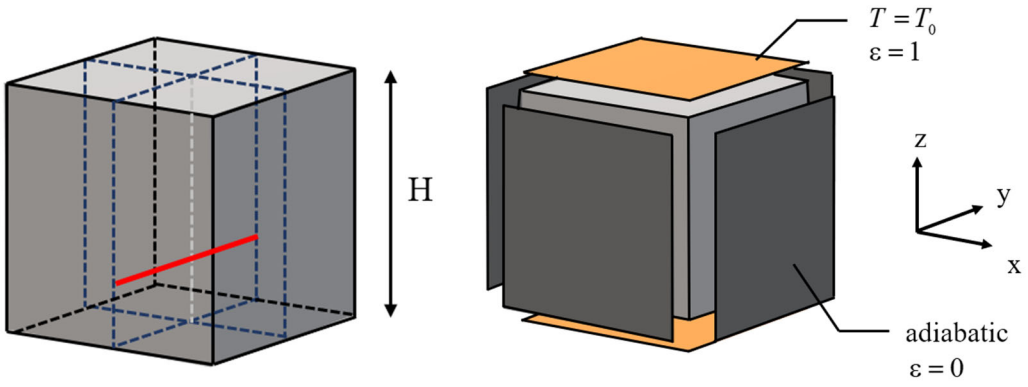

Figure 1.1. Considered geometry. The red line corresponds to the linear heat source.

1.2 Natural convection

1.2.1 Conservation equations

The governing equations of fluid flow represent mathematical statements of the conservation law of physics:

- The mass of a fluid is conserved.
- The rate of change of momentum equals the sum of the forces on a fluid particle. (Newton's second law)
- The rate of change of total energy is equal to the sum of the rate of heat addition and the rate of work done on the fluid volume. (first law of thermodynamics)

Mass conservation

In the absence of mass sources or sinks, the equation of mass conservation is written as

$$\frac{\partial \rho}{\partial t} + \frac{\partial (\rho U_i)}{\partial X_i} = 0 \tag{1.1}$$

For an incompressible fluid, the density ρ is invariant in space and time. The equation (1.1) becomes

$$\frac{\partial U_i}{\partial X_i} = 0 \tag{1.2}$$

Momentum conservation

Newton's second law states that the rate of change of momentum equals the sum of the forces on the particle which can be distinguished into two types of forces.

- Surface forces (pressure forces and viscous forces)
- Body forces (here only the gravity force is considered)

The momentum conservation equation is then given by

$$\frac{\partial \rho U_i}{\partial t} + \frac{\partial \rho U_i U_j}{\partial X_j} = -\frac{\partial p}{\partial X_i} + \frac{\partial \tau_{ij}}{\partial X_j} - \rho g \delta_{iz} \tag{1.3}$$

where U_i is the velocity components in the direction X_i, τ_{ij} the viscous stress tensor and g the acceleration of gravity carried by the *Z*-axis.

Additionally, the internal friction of the fluid is supposed to be Newtonian, meaning that the shear stress is assumed to be proportional to the strain, and eq. (1.3) becomes

$$\frac{\partial \rho U_i}{\partial t} + \frac{\partial \rho U_i U_j}{\partial X_j} = -\frac{\partial p}{\partial X_i} + \frac{\partial}{\partial X_j} \mu \left(\frac{\partial U_i}{\partial X_j} + \frac{\partial U_j}{\partial X_i} \right) - \rho g \delta_{iz} \tag{1.4}$$

where μ is the dynamic viscosity.

Energy conservation

Neglecting the pressure and viscous forces working on the fluid volume, the energy equation derived from the first law of thermodynamics is given by

$$\frac{\partial(\rho c_p T)}{\partial t}+\frac{\partial(\rho c_p T U_i)}{\partial X_i}=\frac{\partial}{\partial X_i}(\lambda\frac{\partial T}{\partial X_i})+Q''' \tag{1.5}$$

where c_p is the specific heat at constant pressure, λ the thermal conductivity, and Q''' the internal heat source per unit volume.

We note that in the present work, a linear heat source is considered in the fluid domain. Thus, the energy equation becomes

$$\frac{\partial(\rho c_p T)}{\partial t}+\frac{\partial(\rho c_p T U_i)}{\partial X_i}=\frac{\partial}{\partial X_i}(\lambda\frac{\partial T}{\partial X_i})+Q_s'''+Q_{ext}''' \tag{1.6}$$

where Q_s''' is the volumetric power generated by the linear heat source, and Q_{ext}''' stands for other heat sources, such as sources thermal radiation, chemical reaction, etc.

In our configuration, the source term Q_s''' is positioned along the line $(X_s,\ Y, Z_s)$. It is supposed to be immaterial and emitted in a very small area around the line position:

$$Q_s'''=\begin{cases}\dfrac{Q_s'}{\delta X_s \delta Z_s} & \text{if } (X,\ Z)\in[X_s\pm\dfrac{\delta X_s}{2}]\times[Z_s\pm\dfrac{\delta Z_s}{2}]\\ 0, & \text{otherwise}\end{cases} \tag{1.7}$$

where δX_s and δZ_s are the spatial extension of the heat source in Cartesian coordinates.

1.2.2 The Boussinesq approximation

Considering a plume flow, the body force contains a term accounting for buoyancy effects. We suppose the Boussinesq approximation to be valid, which implies that the density variations are neglected in all the terms except the one accounting for buoyancy effects. A further simplification is the linearization of the temperature dependency of the density, which yields

$$\rho=\rho_{ref}[1-\beta_T(T-T_{ref})] \tag{1.8}$$

where $(T_{ref},\ \rho_{ref})$ is the reference state of the fluid, and β_T is the coefficient of thermal expansion, $\beta_T=-[1/\rho(\partial\rho/\partial T)]_{T_{ref}}$, equals to $1/T_{ref}$ for a perfect gaz. Adding the first term of this expression with the static pressure p, and defining the driving pressure

$$p_h=p-\rho_{ref} g\delta_{iz} \tag{1.9}$$

Then the momentum conservation equation is given by

$$\frac{\partial U_i}{\partial t}+\frac{\partial (U_i U_j)}{\partial X_j}=-\frac{\partial p_h}{\partial X_i}+\nu\frac{\partial^2 U_i}{\partial X_j^2}+\rho_{ref}\beta_T(T-T_{ref})g\delta_{iz} \tag{1.10}$$

1.2.3 Non-dimensional formulations

With the aid of characteristic scales of the problem, it is possible to transform the governing equations into a non-dimensional form. The cavity size H is taken as the reference length, and the reference velocity is the diffusive velocity $V_{ref}=\alpha/H$ where α is the thermal diffusivity $(\alpha=\lambda/\rho c_p)$. The dimensionless temperature is defined by

$$\theta=\frac{T-T_{ref}}{\Delta T} \text{ with } \Delta T=Q_s'/\lambda \tag{1.11}$$

By introducing these reference quantities, the set of dimensionless equations for an incompressible fluid under Boussinesq hypothesis then reads

$$\frac{\partial u_i}{\partial x_i}=0 \tag{1.12}$$

$$\frac{\partial u_i}{\partial t}+\frac{\partial (u_i u_j)}{\partial x_j}=-\frac{\partial p^*}{\partial x_i}+\mathrm{Pr}\frac{\partial^2 u_i}{\partial x_j^2}+\mathrm{RaPr}\theta\delta_{iz} \tag{1.13}$$

$$\frac{\partial \theta}{\partial t}+\frac{\partial (\theta u_j)}{\partial x_j}=\frac{\partial^2 \theta}{\partial x_j^2}+\varphi_s'''+\frac{H^2}{\lambda\Delta T}Q_{ext} \tag{1.14}$$

where φ_s''' is the volumetric linear source normalized by Q_s'/H^2, defined as

$$\varphi_s'''=\begin{cases}\dfrac{1}{\delta x_s \delta z_s} \text{ if } (x,\ z)\in[x_s\pm\dfrac{\delta x_s}{2}]\times[z_s\pm\dfrac{\delta z_s}{2}]\\ 0,\ \text{otherwise}\end{cases} \tag{1.15}$$

The dimensionless quantities and the characteristic parameters of the problem are summarized in Table 1.1.

Dimensionless coordinates	$x_i = X_i / H$
Dimensionless velocity component	$u_i = U_i / V_{ref}$ with $V_{ref} = \alpha / H$
Dimensionless temperature	$\theta = (T - T_{ref}) / \Delta T$ with $\Delta T = Q_s' / \lambda$
Dimensionless time	$t = t_{\dim} / t_{ref}$ with $t_{ref} = H / V_{ref} = H^2 / \alpha$
Dimensionless pressure	$p^* = p_h H^2 / (\rho \alpha^2)$
Rayleigh number	$\mathrm{Ra} = g\beta_T Q_s' H^3 / (\lambda \nu \alpha)$
Prandtl number	$\mathrm{Pr} = \nu / \alpha$

Table 1.1. Dimensionless quantities and characteristic parameters for the convective problem.

1.2.4 Transition to turbulence and Hopf bifurcation

Fluid flow can be characterized by its flow regime: laminar, turbulent or transitional. With the increase of the control parameter, here the Rayleigh number, flow experiences first a transition from steady to time-dependent motion, and then becomes more and more complex until a turbulent state is reached. Landau (1944) introduced the concept of transition to turbulence, and proposed a mechanism consisting of a sequence of bifurcations in which at each time a discrete frequency is added. In general, the ratio between separate frequencies is not an integer and a quasi-periodic motion occurs. At the end of an infinite number of discrete frequencies, the flow system reaches a turbulent state and has a broadband frequency spectrum.

If the Rayleigh number is below a critical value Ra_c, the motion is steady, which can be represented by a single point in the phase space. Since the fluid is stable, this point attracts all other points, initially deviating from the stable situation. Therefore, this point is called an attractor. Above the critical Rayleigh number, the flow becomes unstable, and the attractor becomes a limit cycle, which is called a Hopf bifurcation (McCracken & Marsden, 1976). We emphasize that in a Hopf bifurcation, the limit cycle is a purely periodic solution which can be pictured as a closed curve in phase space.

A Hopf bifurcation can be either supercritical or subcritical. In a supercritical Hopf bifurcation, the limit cycle grows out of the equilibrium point. In other words, right at the parameter of the Hopf bifurcation ($\mathrm{Ra} = \mathrm{Ra}_c$), the limit cycle has zero amplitude. If the bifurcation parameter is greater than the critical value ($\mathrm{Ra} > \mathrm{Ra}_c$), this amplitude grows as the parameters move further into the stable limit-cycle regime. In the subcritical case, the limit cycle is shown to be unstable when the real bifurcation parameter is less than the critical value (McCracken & Marsden, 1976).

For a supercritical Hopf bifurcation, the amplitude of the perturbation in the vicinity of the transition satisfies the relation

$$\Phi_{\max} - \Phi_{\min} \propto \sqrt{\mathrm{Ra} - \mathrm{Ra}_c} \tag{1.16}$$

This signature of a supercritical bifurcation can be used to determine the critical Rayleigh number by linear extrapolation of the square of the amplitude of the oscillations to zero. A second distinctive feature of a Hopf bifurcation is the relationship between the oscillation frequency and the Rayleigh number in the vicinity of the bifurcation point. Since the plume has a thermally stratified field, the Brunt Väisälä frequency can be associated to the oscillation frequency of plume flow

$$f \propto f_{BV} \tag{1.17}$$

and the Brunt Väisälä frequency is defined as

$$f_{BV}^2 = [(f_{BV})_{\dim} \frac{H^2}{\alpha}]^2 = -\frac{g}{\rho}\frac{\partial \rho}{\partial z}\frac{H^4}{\alpha^2} = g\beta\frac{\partial T}{\partial z}\frac{H^4}{\alpha^2} \tag{1.18}$$

By applying an approximation of the stratification value, the Brunt Väisälä frequency at any horizontal planes above the heat source can be expressed as (Desrayaud & Lauriat, 1993)

$$f^2 \propto f_{BV}^2 \approx \mathrm{Ra}\,\mathrm{Pr} \text{ with } \frac{\partial T}{\partial z} \approx \frac{Q_s'}{\lambda_c H} \tag{1.19}$$

1.2.5 Turbulence and turbulence modelling

For a turbulent flow, the parameters (velocity, temperature and so on) vary in a chaotic way. The flow properties can be characterized in terms of time integrated mean values ($\overline{U}$, $\overline{V}$, $\overline{W}$, $\overline{T}$) and higher orders statistical moments (U', V', W', T', $U'T'$, etc.). In fact, the fluid motion becomes intrinsically unsteady, and the turbulent fluctuations always have a three-dimensional spatial character. Furthermore, visualizations of turbulent flows reveal rotational flow structures, so-called turbulent eddies, with a wide range of length scales.

Figure 1.2 presents a schematic of the turbulent kinetic energy spectrum $E(k)$ in function of the wave number (k), which can be divided into three subranges: the source subrange, the inertial subrange and the viscous subrange. The source subrange is responsible for the production of energy. It is associated to the macroscopic scale of the same order of the length scale of the mean flow, which characterizes the length of the larger eddies. These large eddies are dominated by inertia effects and viscous effects are negligible. The inertial subrange corresponds to the intermediate range of scale which is strongly stretched by the larger eddies without being affected by the viscous effects. In this way the kinetic energy is handed down from large eddies to progressively smaller and smaller eddies, which leads to the Kolmogorov energy cascade

$$E(k) = K_0 \xi^{2/3} k^{-5/3} \tag{1.20}$$

where K_0 is the Kolmogorov constant, and ξ is the viscous dissipation rate.

The viscous subrange is associated to the last smallest scale, named the Kolmogorov scale η_k, which is dominated by viscous effects (Lesieur, 1990; Versteeg & Malalasekera, 2007).

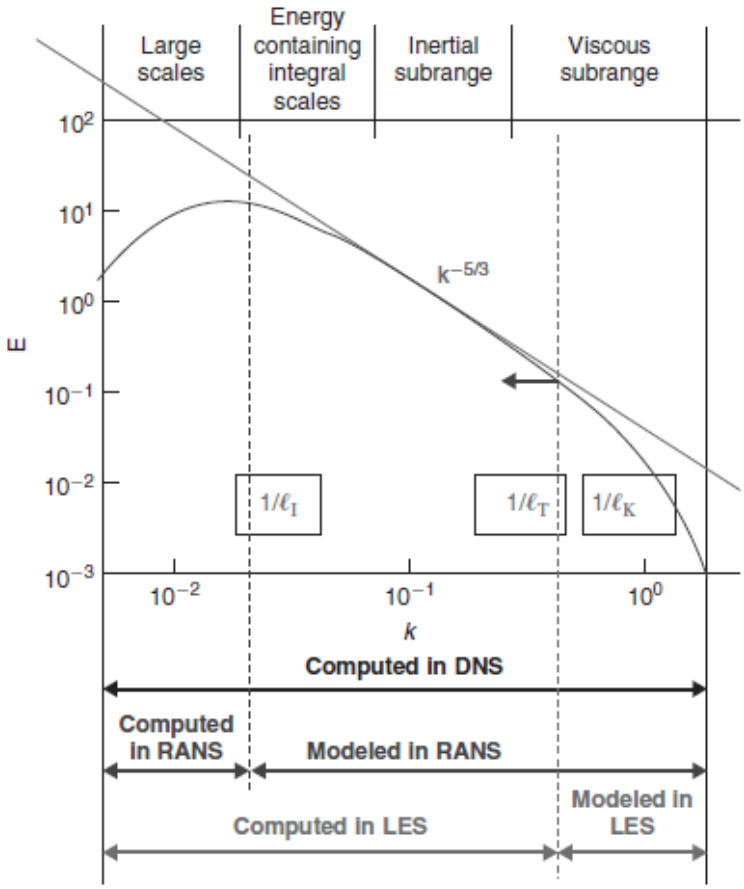

Figure 1.2. Energy spectrum of turbulence in function of the wave number k, with indication of the range of application of DNS, LES and RANS models. The length scales l_T and l_l are respectively associated with the LES and RANS approaches. (From Hirsch (1998)).

To compute the large-scale turbulent eddies, or even the small-scale eddies, there are mainly three families of methods in numerical simulations of turbulence, as indicated in Figure 1.2:

- Direct numerical simulation (DNS)
- Large Eddy Simulation (LES)
- Reynolds Averaged Navier–Stokes (RANS)

In DNS, the governing equations are numerically solved without any model, meaning that all the spatial and temporal scales of the flow must be captured on the computational grid and by the time discretization scheme. This is a formidable challenge in terms of computational effort, which grows with increasing Reynolds numbers, since the size of the smallest

turbulent eddies, the Kolmogorov scale, is inversely proportional to $\mathrm{Re}^{3/4}$ (Hirsch, 1998). If we wish a resolution of n points per unit length of the smallest eddy, the total number of required mesh points will scale as $n^3 \mathrm{Re}^{3/4}$.

In LES approach, the turbulent fluctuations are computed directly only above a certain length scale (l_T). Below that scale, called the subgrid scale, the turbulence effects are modelled by semi-empirical laws. In this way, the spatial resolution is decreased compared to DNS, and also the temporal resolution requirements. This leads to a substantial decrease in both computer storage and work. The equations describing LES models are obtained by applying a spatial filter on the governing equations. By performing this filtering operation extra terms appear, accounting for the subgrid contributions. The subgrid contributions are unknown in principle, and therefore they have to be modelled in order to close the set of LES equations.

Finally, the Reynolds Averaged Navier–Stokes (RANS) model is restricted to the computation of the averaged turbulent flow. This approach ignores the turbulent fluctuations and aims at computing only the turbulent averaged flow. The idea behind the equations is the Reynolds decomposition, whereby any quantity can be decomposed into a time-averaged term and a time fluctuation term.

Application of DNS

Although DNS requires considerable computer resources, it remains a valuable tool in turbulence studies. DNS can provide a database of information for improving lower level approximations (LES or RANS). DNS has already led to very informative results on the fundamental physics of turbulence in various frameworks. A review of the state of art of direct numerical simulation of turbulent flows can be found in Jiménez (2003) and Geurts (2003). To better understand the fundamental mechanisms of turbulent plume flow and to evaluate other turbulence models, DNS has been applied as a basic tool in the works of Bastiaans et al. (2000) and Pham et al. (2007).

In the present work, DNS is used to resolve the governing equations, which then leads to severe requirements for the grid resolution. To ensure sufficient resolution, Grötzbach (1983) derived a formulate for direct numerical simulation to estimate the ratio between the mean cell size of the spatial discretization and the smallest scales of the velocity and temperature fields, i.e. the Kolmogorov scale η_k and the thermal dissipative scale η_T. The Grötzbach (1983) requirement has been used in many studies of Rayleigh-Bénard convection, e.g. Kaczorowski and Wagner (2009); Vincent et al. (2012), and will be adopted here to verify the grid resolution. If the grid spacing between points is $\delta r = (\delta x \delta y \delta z)^{1/3}$, it must satisfy the following relationships (Grötzbach, 1983)

$$\delta r \le \pi\eta_k = \pi(\nu^3/\xi)^{1/4} \quad \text{for} \quad \Pr < 1 \tag{1.21}$$

$$\delta r \le \pi\eta_T = \pi(\kappa^3/\xi)^{1/4} \quad \text{for} \quad \Pr > 1 \tag{1.22}$$

where ξ is the dissipation of turbulence kinetic energy defined by

$$\xi = \nu \cdot \overline{S_{ij}S_{ij}} \quad \text{with} \quad S_{ij} = \frac{1}{2}\left(\frac{\partial U_i'}{\partial X_j} + \frac{\partial U_j'}{\partial X_i}\right) \tag{1.23}$$

in which $\overline{\cdot}$ denotes time-averaged quantities and $'$ the fluctuating parts.

1.3 Radiative transfer

In this section, the radiative transfer equation (RTE) is described in detail and different models for predicting the properties of the participating gas are discussed. Finally, a complete description of the Spectral Line Weighted (SLW) model is given.

1.3.1 Radiative transfer equation

For radiative phenomena, the spectral radiative intensity is the fundamental quantity. It is defined as the radiative energy flux per unit solid angle, per unit frequency and per surface area normal to the rays. The total radiative intensity is the intensity integrated over the entire spectrum.

As illustrated in Figure 1.3, the spectral intensity $I_\nu(\mathbf{x}, \boldsymbol{s})$ at a vector position $\mathbf{x}$ emitted across an apparent area dS' limited by a solid angle $d\Omega$ along a unit direction vector $\boldsymbol{s}$, is expressed by

$$I_\nu(\mathbf{x}, \boldsymbol{s}) = \frac{dQ_\nu}{d\Omega dS'} = \frac{dQ_\nu}{d\Omega dS\cos\theta} \tag{1.24}$$

where Q_ν is the radiative energy flux, and $\cos\theta$ the cosine angle between dS and dS'.

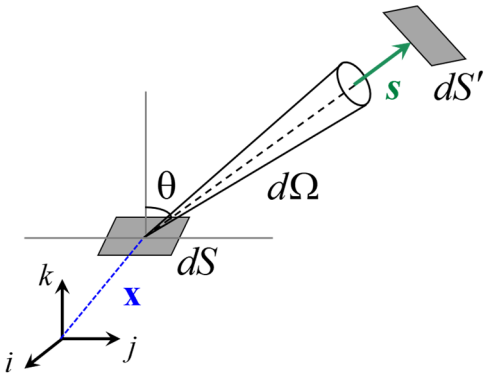

Figure 1.3. Illustration of the definition of the spectral radiative intensity $I_\nu(\mathbf{x}, \boldsymbol{s})$ along the direction $\boldsymbol{s}$ in a solid angle $d\Omega$.

The radiative intensity traveling through a participating medium in the direction $\boldsymbol{s}$ can be attenuated by absorption and by scattering away from the traveling direction. But at the same time, it also gains energy by emission as well as scattering from other directions into the original traveling direction $\boldsymbol{s}$. By analyzing energy balance for an elementary control volume in the direction $\boldsymbol{s}$, the radiative transfer equation (RTE) can be written as

$$\begin{aligned}&\frac{1}{c}\frac{\partial I_\nu(\mathbf{x},\boldsymbol{s},t)}{\partial t}+\boldsymbol{s}\cdot\nabla I_\nu(\mathbf{x},\boldsymbol{s},t)=\kappa_\nu I_\nu^b(T(\mathbf{x}))-\beta_\nu I_\nu(\mathbf{x},\boldsymbol{s},t)\\&+\frac{\sigma_\nu}{4\pi}\int_{4\pi} I_\nu(\mathbf{x},\boldsymbol{s}',,t)\Phi_\nu(\boldsymbol{s}',\boldsymbol{s})d\Omega'\end{aligned} \tag{1.25}$$

where c is the speed of light, κ_ν and σ_ν are the spectral absorption and scattering coefficients respectively, and β_ν is the extinction coefficient $\beta_\nu=\kappa_\nu+\sigma_\nu$. $I_\nu^b(T(\mathbf{x}))$ is the monochromatic radiative intensity of the black body at the frequency ν and the local temperature $T(\mathbf{x})$. Φ_ν is the scattering phase function which is linked to the probability that a beam from direction $\boldsymbol{s}'$ is scattered to direction $\boldsymbol{s}$.

For the majority of engineering applications, the first term of eq. (1.25) can be neglected, as the speed of light is many orders of magnitudes superior to any other velocity scale in the problem. Moreover, the participating medium in this work is considered to be non-scattering $(\sigma_\nu=0)$. Therefore, the quasi-steady form of RTE in Cartesian coordinates reduces to

$$\mu\frac{\partial I_\nu(\mathbf{x},\ \boldsymbol{s})}{\partial X}+\eta\frac{\partial I_\nu(\mathbf{x},\ \boldsymbol{s})}{\partial Y}+\xi\frac{\partial I_\nu(\mathbf{x},\ \boldsymbol{s})}{\partial Z}=\kappa_\nu[I_\nu^b(T(\mathbf{x}))-I_\nu(\mathbf{x},\ \boldsymbol{s})] \tag{1.26}$$

where $(\mu,\ \eta,\ \xi)$ are the cosines directors of the direction of the radiative propagation $\boldsymbol{s}$ with respect to the $(x,\ y,\ z)$ axis.

- **Boundary conditions for RTE**

Generally, the radiative intensity leaving a wall surface which surrounds a participating medium can be specified and employed as boundary condition for the RTE. For an opaque surface that emits and reflects diffusively, the exiting intensity is independent of direction. Therefore, at a point $\mathbf{x}_w$ on the gray surface, the exiting intensity can be expressed as the sum of the emitted intensity and the reflected intensity

$$I_\nu(\mathbf{x}_w,\ \boldsymbol{s})=\varepsilon_w I_\nu^b(T(\mathbf{x}_w))+\frac{\rho_w}{\pi}H_\nu(\mathbf{x}_w) \tag{1.27}$$

for the directions $\boldsymbol{s}\cdot\boldsymbol{n}_w>0$, and $\boldsymbol{n}_w$ is the inward-pointing normal vector at the wall, ε_w the wall emissivity, ρ_w the reflectance with $\rho_w=1-\varepsilon_w$, and H_ν the hemispherical irradiation (i.e., incoming radiative heat flux) defined as

$$H_\nu(\mathbf{x}_w) = \int_{\boldsymbol{s}'\cdot\boldsymbol{n}_w<0} I_\nu(\mathbf{x}_w,\ \boldsymbol{s}')\left|\boldsymbol{s}'\cdot\boldsymbol{n}_w\right| d\Omega' \tag{1.28}$$

where, as indicated in Figure 1.4, $\boldsymbol{n}_w$ is the inward surface normal unit vector and $\boldsymbol{s}'$ is the direction unit vector of the incoming intensity $I_\nu(\mathbf{x}_w,\ \boldsymbol{s}')$.

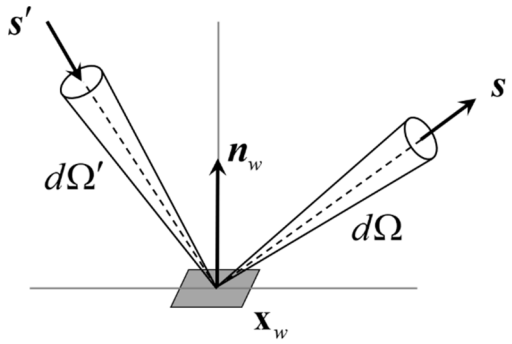

Figure 1.4. Radiative intensity reflected from a surface.

- **Radiative flux terms**

In order to correlate the radiation field with the flow field, the terms of incident radiative flux, radiative power per volume as well as the net radiative flux at the walls need to be determined. They are defined as follows:

Incident radiative flux

$$G_\nu(\mathbf{x}) = \int_{4\pi} I_\nu(\mathbf{x},\ \boldsymbol{s}) d\Omega \tag{1.29}$$

$$G(\mathbf{x}) = \int_0^{+\infty} G_\nu(\mathbf{x}) d\nu \tag{1.30}$$

Radiative flux vector

$$\boldsymbol{Q}_r(\mathbf{x}) = \int_0^{+\infty}\int_0^{4\pi} \boldsymbol{s}\cdot I_\nu(\mathbf{x},\boldsymbol{s}) d\Omega d\nu \tag{1.31}$$

Volumetric radiative power

$$Q'''_{ext}(\mathbf{x}) = -\nabla\cdot\boldsymbol{Q}_r(\mathbf{x}) \tag{1.32}$$

$$Q'''_{ext}(\mathbf{x}) = \int_0^{+\infty} \kappa_\nu[G_\nu(\mathbf{x}) - 4\pi I_\nu^b(T(\mathbf{x}))] d\nu \tag{1.33}$$

Net radiative flux at gray walls

$$\mathrm{Q}_r^{net}(\mathbf{x}_w) = \pi\int_0^{+\infty} \varepsilon_w I_\nu^b(T(\mathbf{x}_w)) d\nu - \int_0^{+\infty} \varepsilon_w H_\nu(\mathbf{x}_w,\ \boldsymbol{n}_w) d\nu \tag{1.34}$$

1.3.2 Non-dimensional formulations

In order to be consistent with the non-dimensional formulations of the convective problem, we consider the cavity length H as the reference length scale. However, the radiative problem requests absolute temperature levels, so the physical problem loses its symmetry

property around the reference temperature T_{ref} obtained for the convective problem, and it is necessary to define another dimensionless temperature noted ψ.

The characteristic dimensionless quantities are thus given in Table 1.2.

Positions	$\mathbf{x}^+ = \mathbf{x} / H$
Gradient	$\nabla^+ = H \cdot \nabla$
Intensity	$I_\nu^+(\mathbf{x}^+,\ \boldsymbol{s}) = I_\nu(\mathbf{x},\ \boldsymbol{s}) / I_\nu^b(T_{ref})$
Temperature ratio	$\Theta_0 = T_{ref} / \Delta T = \lambda T_{ref} / Q_s'$
Dimensionless radiative temperature	$\psi(\mathbf{x}) = T(\mathbf{x}) / T_{ref} = 1 + \theta(\mathbf{x}) / \Theta_0$
Optical thickness	$\tau = \kappa H$

Table 1.2. Dimensionless quantities of the radiative problem.

With these dimensionless quantities, the radiative transfer equation for a non-scattering medium can be written in its non-dimensional form

$$\boldsymbol{s} \cdot \nabla^+ I_\nu^+(\mathbf{x}^+,\ \boldsymbol{s}) = \tau_\nu [I_\nu^{b,+}(\psi(\mathbf{x}^+)) - I_\nu^+(\mathbf{x}^+,\ \boldsymbol{s})] \tag{1.35}$$

and by introducing the cosines directors of the propagation direction in Cartesian coordinates

$$\mu \frac{\partial I_\nu^+(\mathbf{x}^+,\ \boldsymbol{s})}{\partial x} + \eta \frac{\partial I_\nu^+(\mathbf{x}^+,\ \boldsymbol{s})}{\partial y} + \xi \frac{\partial I_\nu^+(\mathbf{x}^+,\ \boldsymbol{s})}{\partial z} = \tau_\nu [I_\nu^{b,+}(\psi(\mathbf{x}^+)) - I_\nu^+(\mathbf{x}^+,\ \boldsymbol{s})] \tag{1.36}$$

The other dimensionless radiative terms are defined below:

Radiative intensity at the walls

$$I_\nu^+(\mathbf{x}_w^+,\ \boldsymbol{s}) = \varepsilon_w I_\nu^{b,+}(\psi(\mathbf{x}_w^+)) + \frac{\rho_w}{\pi} H_\nu^+(\mathbf{x}_w^+,\ \boldsymbol{n}_w) \quad \text{for} \quad \boldsymbol{s} \cdot \boldsymbol{n}_w > 0 \tag{1.37}$$

Hemispherical irradiation

$$H_\nu^+(\mathbf{x}_w^+,\ \boldsymbol{n}_w) = \int_{\boldsymbol{s}' \cdot \boldsymbol{n}_w < 0} I_\nu^+(\mathbf{x}_w^+,\ \boldsymbol{s}') \left| \boldsymbol{s}' \cdot \boldsymbol{n}_w \right| d\Omega' \tag{1.38}$$

Incident radiative flux

$$G_\nu^+(\mathbf{x}^+) = \int_{4\pi} I_\nu^+(\mathbf{x}^+,\ \boldsymbol{s}) d\Omega \tag{1.39}$$

$$G^+(\mathbf{x}) = \int_0^{+\infty} G_\nu^+(\mathbf{x}^+) d\nu \tag{1.40}$$

Volumetric radiative power

$$\varphi_r'''(\mathbf{x}^+) = \frac{H}{\sigma_B T_0^4} Q_{ext}'''(\mathbf{x}) \tag{1.41}$$

$$\varphi_r'''(\mathbf{x}^+) = \int_0^{+\infty} \tau_\nu [G_\nu^+(\mathbf{x}^+) - 4\pi I_\nu^{b,+}(\psi(\mathbf{x}^+))] d\nu \tag{1.42}$$

Net radiative flux at the walls

$$q_r^{net}(\mathbf{x}_w^+) = \frac{1}{\sigma_B T_0^4} \mathrm{Q}_r^{net}(\mathbf{x}_w) \tag{1.43}$$

$$q_r^{net}(\mathbf{x}_w^+) = \pi \int_0^{+\infty} \varepsilon_w I_\nu^{b,+}(\psi(\mathbf{x}_w^+)) d\nu - \int_0^{+\infty} \varepsilon_w H_\nu^+(\mathbf{x}_w^+,\ \boldsymbol{n}_w) d\nu \tag{1.44}$$

1.3.3 Radiative properties of participative gases

The participative gases can emit and absorb in an infinite set of distinct wavenumbers or frequencies, which makes the prediction of radiative properties of gaseous media a difficult task in the description of radiative phenomena. For sake of simplification, the gray gas approximation is a common practice in engineering and has been widely used in the literature for convection-radiation coupled flows in enclosures (Lauriat, 1982; Yücel et al., 1989; Draoui et al., 1991; Lari et al., 2011), as an example.

1. Gray gas approximation

The gray gas approximation consists in considering that the absorption coefficient κ_ν has no dependence on frequency, e.g. $\kappa_\nu = \kappa_0$. Integrating the RTE over the whole frequency range, the equation can be directly expressed in total quantities and the problem is faster to solve. After applying the gray gas approximation, we obtain

$$\mu \frac{\partial I(\mathbf{x},\ \boldsymbol{s})}{\partial X} + \eta \frac{\partial I(\mathbf{x},\ \boldsymbol{s})}{\partial Y} + \xi \frac{\partial I(\mathbf{x},\ \boldsymbol{s})}{\partial Z} = \kappa_0 [\frac{\sigma_B T^4(\mathbf{x})}{\pi} - I(\mathbf{x},\ \boldsymbol{s})] \tag{1.45}$$

The total radiative intensity of blackbody is defined by

$$\int_0^{+\infty} I_\nu^b(T) d\nu = \frac{\sigma_B T^4}{\pi} \tag{1.46}$$

where σ_B is the Stefan-Boltzmann constant.

The dimensionless RTE for a gray gas is then written in the form

$$\mu \frac{\partial I^+(\mathbf{x}^+,\ \boldsymbol{s})}{\partial x} + \eta \frac{\partial I^+(\mathbf{x}^+,\ \boldsymbol{s})}{\partial y} + \xi \frac{\partial I^+(\mathbf{x}^+,\ \boldsymbol{s})}{\partial z} = \tau_0 [\frac{\psi^4(\mathbf{x}^+)}{\pi} - I^+(\mathbf{x}^+,\ \boldsymbol{s})] \tag{1.47}$$

and the dimensionless radiative terms are obtained below

$$\varphi_r'''(\mathbf{x}^+) = \tau_0 [G^+(\mathbf{x}^+) - 4\psi^4(\mathbf{x}^+)] \tag{1.48}$$

$$q_r^{net}(\mathbf{x}_w^+) = \varepsilon_w \psi^4(\mathbf{x}_w{}^+) - \varepsilon_w \int_{\boldsymbol{s}' \cdot \boldsymbol{n}_w < 0} I^+(\mathbf{x}_w^+,\ \boldsymbol{s}') \left| \boldsymbol{s}' \cdot \boldsymbol{n}_w \right| d\Omega' \tag{1.49}$$

By applying this approach, the numerical solution of the radiative problems is greatly accelerated. But the disadvantage of this approximation is to represent the spectral behavior of a gas with a unique optical thickness. For the cases of gases with a large absorption spectrum, such as humid air that we consider in this study, the gray gas approximation is not appropriate. Thus, more complex models must be considered.

2. Real gas model

The approaches for the representation of radiative properties may by mainly distinguished into four groups: (1) line-by-line calculations, (2) narrow-band models, (3) wide-band models and (4) global models.

(1) Line-by-line calculations

Line-by-line calculations (Hartmann et al., 1984) represents each discrete absorption-emission line of the entire spectrum by its intensity and half-width of the line. Such calculations depend on very detailed information of each single spectral line. Because of strongly varying values of the absorption coefficient, the spectral radiative transfer problem must be solved for a huge number of frequencies. Although this approach may be the most accurate, it is not feasible in practical configurations due to the requirement of vast amounts of computer resources.

(2) Narrow-band models

In these models, the absorption spectrum is discretized in intervals called narrow bands where the Planck function is assumed to be constant. Hence, it consists in replacing the spectral absorption coefficient distribution by smoothened discrete values appropriately averaged over narrow spectral bands. In order to calculate the averaged band values, some information on the spacing of individual lines within the narrow band and on their relative strengths is needed. Various narrow band models (Hartmann et al., 1984; Soufiani & Taine, 1987; Kim et al., 1991; Soufiani & Taine, 1997; Liu et al., 1998; Coelho, 2002) have been proposed for this purpose.

An alternative to the "traditional" narrow band models is the so-called “correlated *k*-distribution” (CK model) (Goody et al., 1989). In this method, it is observed that over a narrow spectral range, the absorption coefficient attains the same value many times and can be reordered in the correlated *k*-distribution method. This results in a smooth monotonically increasing function of absorption coefficient vs artificial wavenumber, and makes spectral integration very straightforward.

(3) Wide-band models

Wide band models (Edwards & Menard, 1964; Edwards, 1976) determine the radiative emission or absorption over an interval of wavenumber much more important than for the narrow-band model. Due to the fact that the necessary calculations are relatively simple, this

wide band model was very popular in the past. However, nowadays, it is not commonly used anymore because of its low accuracy.

(4) Global models

Global models consider a global approach of the absorption spectrum. Among various global models, the models based on the discretization of the absorption coefficient by a sum of virtual gray gases are widely used. These models are commonly called the Weighted-Sum-of-Gray-Gases (WSGG) models and was initially proposed by Hottel and Sarofim (1967). The main interest of WSGG method is its low computational cost, but this method appears to be a crude and approximate tool when estimating complex behavior of participating media. More accurate global models can be found in Denison and Webb (1993, 1995) and Rivière et al. (1996), where the Spectral-Line-Based Weighted-Sum-of-Gray-Gases (SLW) model and the Absorption Distribution Function (ADF) model are proposed.

In the WSGG method, the nongray gas is replaced by a number of independent gray gases with different absorption coefficients. The total intensity (or radiative heat flux) is then obtained by adding the results of the gray gases contributions with different weight factors. The absorption coefficients are supposed to be spatially constant and to no longer depend on the local temperature, while the weight factors may depend on the local temperature. These WSGG parameters (absorption coefficients and weight factors) can be obtained with respect to a reference model.

The SLW model is an extension of the WSGG method which provides accurate results when compared to line-by-line method. It considers that the weight factors are determined from a distribution function of the absorption coefficient, weighted by the Planck function. Goutiere et al. (2000) conducted a very complete study of the comparison between different gas models (CK, SNW, EWB, WSGG, SLW) in a rectangular cavity filled with CO_2 and H_2O and showed that the SLW model offers an excellent compromise between precision and computation time. So, many works of coupled flows in a square or cubic cavity (Colomer et al., 2007; Ibrahim et al., 2013; Laouar-Meftah et al., 2014; Cadet, 2015; Billaud et al., 2017) have been conducted with the SLW model to represent the radiative properties of participating medium. Therefore, the SLW model is adopted in this work, and a detailed description of SLW will be presented in the next section.

The ADF model consists in replacing the wavenumber integration of the radiative heat fluxes by an integration over the value of the absorption coefficient. Note that the ADF model has been applied by (Soucasse et al., 2012; Soucasse et al., 2013, 2016) for coupled flows in a cavity, and the discretization was also found to be very accurate when compared to line-by-line calculations. It is similar, in nature, to the SLW method as well as the FSK method developed by Modest (2003).

1.3.4 Implementation of the SLW model

In this work, we will consider a perfect gas mixture of air/H_2O. It is assumed that the molar fraction ($X_{ref} = X_a$) of the absorbing specie (H_2O) and the pressure (P_{ref}) is homogeneous in the gaseous medium. The absorption coefficient κ_ν is defined as

$$\kappa_\nu(T) = N \times C_\nu(X_a,\ T) \tag{1.50}$$

where C_ν is the absorption cross-section which will be explained in the following paragraph, and $N = X_a P_{ref} / (RT)$ is the molar density of the absorbing gas. As we consider in this work only very moderate temperature differences according to the Boussinesq hypothesis, and homogeneous concentration in water vapour, the absorption cross-section is considered as a constant in the whole the cavity, i.e. $C_\nu(X_a,\ T) = C_\nu(X_{ref},\ T_{ref})$.

The SLW method is based on the application of the absorption-line blackbody distribution function $F(C,\ T_g,\ T_b)$, which is the fraction of the blackbody emissive power $E_b(\nu,\ T_b)$ emitted at temperature T_b for which the absorption cross-section $C_k(T_g)$ is below the prescribed value C

$$F(C,\ T_g,\ T_b) = \int_{\{k:\ C_k<C\}} E_b(k,\ T_b) / E_b(T_b) dk \tag{1.51}$$

where $E_b(T_b) = \sigma_B T_b^4$ is the integrated blackbody emissive power over the whole spectrum.

As illustrated in Figure 1.5, the construction procedure of SLW spectral model is in the following way:

First, a set of discrete values ($\tilde{C}_0$, $\tilde{C}_1$, …, $\tilde{C}_{N_g}$) is chosen between the minimum $\tilde{C}_{\min}$ and the maximum $\tilde{C}_{\max}$ values of the absorption cross-section: $\tilde{C}_j = \tilde{C}_{j-1} + \Delta C_j$, $j = 1, 2, ..., N_g$ where N_g is the total number of gray gases considered in the model. Considering a gray gas absorption cross-section C_j specified as $\tilde{C}_{j-1} < C_j < \tilde{C}_j$, the corresponding absorption coefficient is defined by $\kappa_j = N \cdot C_j$, $j = 1, 2, ..., N_g$. Thus, the continuous absorption section $C_k(T_g)$ is replaced by a histogram model spectrum with a finite number of discrete absorption cross-section values.

The RTE equation with its boundary conditions for gray gases is then written as follows

$$\mu \frac{\partial \tilde{I}_j(\mathbf{x},\ \boldsymbol{s})}{\partial X} + \eta \frac{\partial \tilde{I}_j(\mathbf{x},\ \boldsymbol{s})}{\partial Y} + \xi \frac{\partial \tilde{I}_j(\mathbf{x},\ \boldsymbol{s})}{\partial Z} = \kappa_j [a_j \frac{\sigma_B T^4(\mathbf{x})}{\pi} - \tilde{I}_j(\mathbf{x},\ \boldsymbol{s})] \tag{1.52}$$

$$\tilde{I}_j(\mathbf{x}_w, \boldsymbol{s}) = \varepsilon_w a_j \frac{\sigma_B T^4(\mathbf{x}_w)}{\pi} + \frac{1-\varepsilon_w}{\pi} \int_{\boldsymbol{s}' \cdot \boldsymbol{n}_w < 0} \tilde{I}_j(\mathbf{x}_w,\ \boldsymbol{s}') \left| \boldsymbol{s}' \cdot \boldsymbol{n}_w \right| d\Omega' \tag{1.53}$$

where $\tilde{I}_j$ are the radiative intensity of each gray gases. Their corresponding weighting factors are calculated from the absorption-line blackbody distribution function

$$\begin{aligned} a_j &= F(\tilde{C}_j,\ T_g,\ T_b) - F(\tilde{C}_{j-1},\ T_g,\ T_b), \\ a_0 &= F(\tilde{C}_{\min},\ T_g,\ T_b) \end{aligned} \tag{1.54}$$

and the absorption coefficients can be obtained by

$$\begin{aligned} \kappa_j &= N \cdot C_j = N\sqrt{\tilde{C}_j \tilde{C}_{j-1}}, \\ \kappa_0 &= 0 \end{aligned} \tag{1.55}$$

Once the radiative intensities of gray gases are determined, the total intensity is calculated as the sum of all the gray gas intensities

$$I(\mathbf{x},\ \boldsymbol{s}) = \sum_{j=0}^{N_g} \tilde{I}_j(\mathbf{x},\ \boldsymbol{s}) \tag{1.56}$$

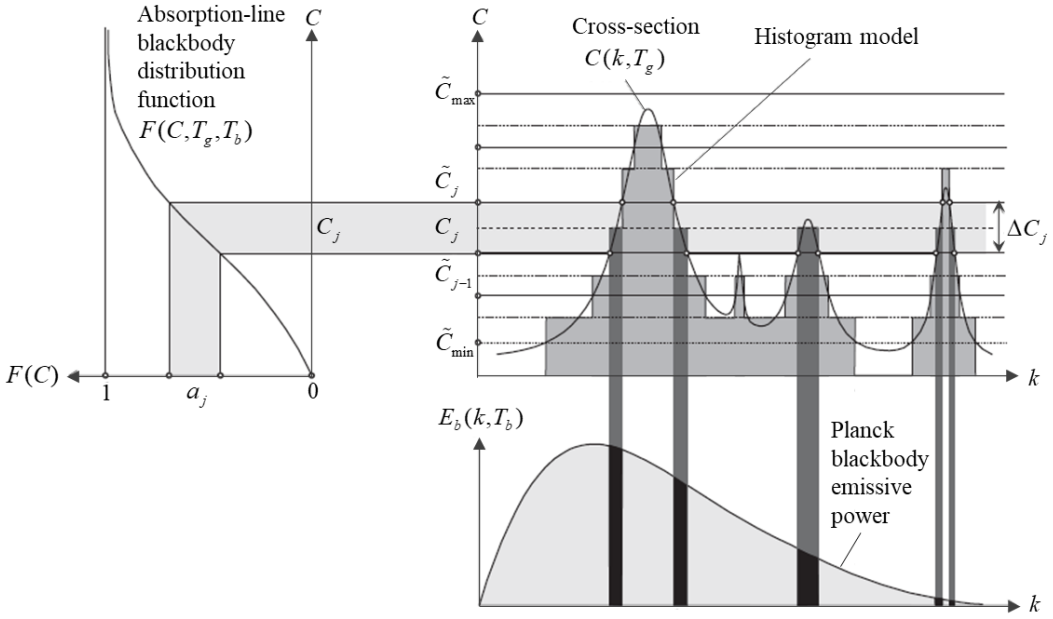

Figure 1.5. The SLW spectral model. (From Solovjov et al. (2014)).

To conclude, when introducing SLW model, it is necessary to choose the number of gray gases N_g and define the optical thickness range $[\tau_{\min},\ \tau_{\max}]$. With this range of optical thickness, the extremum values of $\tilde{C}$ can be obtained by

$$\tilde{C}_{\max/\min} = \tau_{\max/\min} / (N \cdot H) \tag{1.57}$$

Thereby, the modified radiative problem depends not only on the dimensionless parameters previously proposed but also on some additional quantities: the reference pressure P_{ref}, the reference temperature T_{ref}, the molar fraction X_a and the reference length H.

1.4 Convection-radiation coupling

By introducing the radiative source term in the energy equation, the global conservation set of equations of the convection-radiation coupling in dimensionless form is obtained:

$$\frac{\partial u_i}{\partial x_i} = 0 \tag{1.58}$$

$$\frac{\partial u_i}{\partial t} + \frac{\partial (u_i u_j)}{\partial x_j} = \frac{-\partial p_h}{\partial x_i} + \mathrm{Pr}\frac{\partial^2 u_i}{\partial x_j^2} + \mathrm{RaPr}\theta\delta_{iz} \tag{1.59}$$

$$\frac{\partial \theta}{\partial t} + \frac{\partial (\theta u_j)}{\partial x_j} = \frac{\partial^2 \theta}{\partial x_j^2} + \varphi_s''' + \frac{1}{\mathrm{Pl}}\varphi_r''' \tag{1.60}$$

The Planck number (Pl), which characterizes the relation between the thermal conduction and radiation is defined as follows

$$\mathrm{Pl} = \frac{\lambda \Delta T}{\sigma_B T_{ref}^4 H} = \frac{Q_s'}{\sigma_B T_{ref}^4 H} \tag{1.61}$$

- **Boundary conditions**

Kinetic boundary conditions

$u = v = w = 0$ on all the walls.

Thermal boundary conditions

Horizontal walls ($z = 0$, 1) are maintained at T_{ref} : $\theta = 0$;

Left and right walls ($x = 0$, 1) are purely reflecting and adiabatic: $\partial\theta / \partial x = 0$;

Front and rear walls ($y = 0$, 1) are purely reflecting and adiabatic: $\partial\theta / \partial y = 0$.

Radiative intensity

Vertical walls are purely reflecting ($\varepsilon = 0$ and $\rho = 1$):

$I_\nu^+(\mathbf{x}_w^+, \boldsymbol{s}) = \frac{1}{\pi} H_\nu^+(\mathbf{x}_w^+, \boldsymbol{n}_w)$ for $\boldsymbol{s}\cdot\boldsymbol{n}_w > 0$;

Horizontal walls are black surfaces ($\varepsilon = 1$ and $\rho = 0$):

$I_\nu^+(\mathbf{x}_w^+, \boldsymbol{s}) = I_\nu^{b,+}(\psi(\mathbf{x}_w^+))$ for $\boldsymbol{s}\cdot\boldsymbol{n}_w > 0$.

- **Characteristic parameters**

For the case of pure convection (that is without any radiative effect), two typical dimensionless parameters define the problem: the Prandtl number $\mathrm{Pr} = \nu / \alpha$ and the Rayleigh number $\mathrm{Ra} = g\beta_T Q_s' H^3 / (\lambda \nu \alpha)$. When radiation is taken into account, other

dimensionless parameters are involved: the Planck number $\mathrm{Pl} = Q_s' / \sigma_B T_0^4 H$, the temperature ratio $\Theta_0 = \lambda T_{ref} / Q_s'$ and the optical thickness $\tau = \kappa H$. In the case of real gas (here a gas mixture of air/H_2O), some additional quantities must be specified:

- the molar fraction of water vapor X_a;
- the reference quantities for temperature T_{ref}, length H and pressure P_{ref};
- the optical thickness range $[\tau_{\min}, \tau_{\max}]$ and the number of gray gases N_g for the SLW model.

In this work, two different values of reference temperature are considered for the real gaseous cases: $T_{ref} = 300$ K and $T_{ref} = 500$ K, with different water vapor molar fractions. In order to focus on the influence of radiative effects only, the variations of the air properties with the water vapor content will be neglected and we consider only the corresponding thermophysical properties of dry air at the two reference temperatures:

Case	$T_{ref} = 300$ K	$T_{ref} = 500$ K
Pr [-]	0.71	0.68
λ [W.m^{-1}.K^{-1}]	0.0261	0.0404
α [m^2.s^{-1}]	2.12×10^{-5}	5.55×10^{-5}
ρ [kg.m^{-3}]	1.225	0.706

Table 1.3. Thermophysical properties considered in the real gaseous cases.

- **Nusselt numbers**

In order to characterize the heat transfer at the walls of the cavity, the convective and radiative Nusselt numbers are defined as follows. A positive value means that the heat flux is in the same direction of the outgoing normal to the wall, that is gained by the fluid.

- 2D convective and radiative Nusselt numbers averaged over the horizontal walls

$$\mathrm{Nu}_{c,top}^{2D} = -\int_0^1\int_0^1 \left(\frac{\partial\theta}{\partial z}\right)_{z=1} dxdy \tag{1.62}$$

$$\mathrm{Nu}_{c,bottom}^{2D} = \int_0^1\int_0^1 \left(\frac{\partial\theta}{\partial z}\right)_{z=0} dxdy \tag{1.63}$$

$$\mathrm{Nu}_{r,top/bottom}^{2D} = -\frac{1}{\mathrm{Pl}}\int_0^1\int_0^1 (q_r^{net})_{z=0/1} dxdy \tag{1.64}$$

- 1D convective and radiative Nusselt numbers averaged along the horizontal line of the horizontal walls at mid-depth of the cavity

$$\mathrm{Nu}_{c,top}^{1D} = -\int_0^1 \frac{\partial \theta}{\partial z}(x,\ A_y/2,\ 1)\ dx \tag{1.65}$$

$$\mathrm{Nu}_{c,bottom}^{1D} = \int_0^1 \frac{\partial \theta}{\partial z}(x,\ A_y/2,\ 0)\ dx \tag{1.66}$$

$$\mathrm{Nu}_{r,\,top/bottom}^{1D} = -\frac{1}{\mathrm{Pl}}\int_0^1 q_r^{net}(x,\ A_y/2,\ 1)\ dx \tag{1.67}$$

Because the vertical walls in the cavity are considered purely reflecting and adiabatic, the following relationship exists between the 2D averaged Nusselt numbers on the horizontal walls ($\overline{\cdot}$ indicates time-averaged values for unsteady regimes):

$$\overline{\mathrm{Nu}}_{total}^{2D} = \overline{\mathrm{Nu}}_{c,top}^{2D} + \overline{\mathrm{Nu}}_{c,bottom}^{2D} + \overline{\mathrm{Nu}}_{r,\,top}^{2D} + \overline{\mathrm{Nu}}_{r,\,bottom}^{2D} = 1 \tag{1.68}$$

Chapter 2
Numerical modelling

2.1 Computational software

To solve the governing equations, we use the finite volume CFD software SUNFLUIDH coupled to a module for radiative heat transfer calculations from ROCOCO code (Cadet, 2015; Cadet et al., 2016), previously developed during a common project between LaSIE, LIMSI and PPRIME laboratories. SUNFLUIDH has been developed by Dr. Yann Fraigneau at LIMSI since 2011 for the numerical simulation of 2D and 3D unsteady incompressible and non-isothermal flows or flows under Low Mach number hypothesis. This code covers a large range of flows (natural or forced flows, reactive flows, two-phase flows, etc.), and offers the possibility to define complex geometries by means of immersed bodies which modelize the solid parts. A brief description of the numerical modelling is presented below (cf. Fraigneau (2013) for more details).

2.1.1 Staggered grid

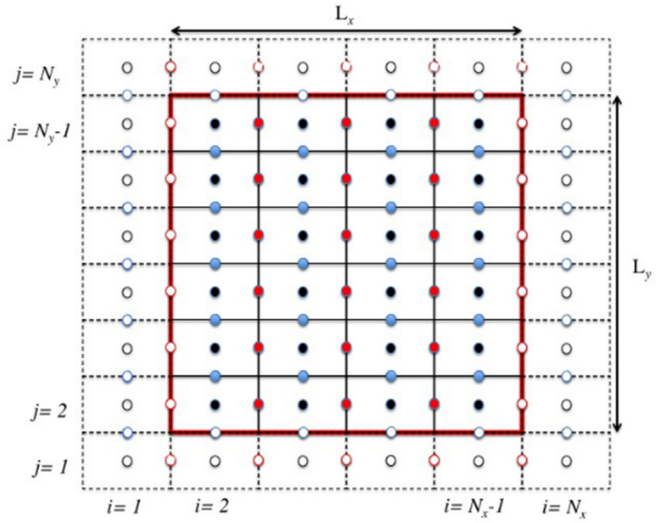

Figure 2.1. 2D representation of staggered grids associated with the spatial discretization of scalar quantities (in black) and the two velocity components (in red and in blue). Empty circles refer to the outside nodes.

The discretization of different quantities is performed on staggered Cartesian grid of MAC type, which ensures the numerical stability of the prediction-correction method for the velocity/pressure coupling. A reference mesh associated with the velocity components and the scalar quantities is defined in Figure 2.1. The discretization nodes are different for each velocity component as well as for scalar quantities. We note that the staggered grid leads to defined ghost nodes outside the domain for the management of the boundary conditions at the edges of the domain.

2.1.2 Numerical methods

- **Spatial discretization**

Let us consider the momentum equation in the following form:

$$\frac{\partial \boldsymbol{V}}{\partial t} + NL(\boldsymbol{V}) = -GP + L(\boldsymbol{V}) \tag{2.1}$$

where $\boldsymbol{V} = (u,\ v,\ w)$ is the velocity field, GP the term of the pressure gradient, L the operator associated with the viscous flux and NL the convective flux operator.

The spatial discretization is performed by a second-order centered scheme according to the finite volume approach with the staggered mesh described above. For the convective flux, a conservative formulation is applied in this work.

- **Time discretization**

The time derivative discretization adopts a second-order Backward Differentiation Formula (BDF2)

$$\left(\frac{\partial u_i}{\partial t}\right)^{n+1} = \frac{3u_i^{n+1} - 4u_i^n + u_i^{n-1}}{2\Delta t} + O(\Delta t^2) \tag{2.2}$$

For stability reasons, a semi-implicit formulation is applied in the time discretization of the other terms. The viscous term is treated implicitly and defined at the instants t^{n+1}, while the convection flux is estimated by an explicit linear extrapolation scheme

$$NL^{n+1} = 2NL^n - NL^{n-1} \tag{2.3}$$

With the consistency of the conservation equation (1.59), the complete second order semi-implicit formulation of the momentum equation reads

$$\frac{3u_i^{n+1} - 4u_i^n + u_i^{n-1}}{2\Delta t} + NL^{n+1} = -GP^{n+1} + \mathrm{Pr}\frac{\partial^2 u_i^{n+1}}{\partial x_j^2} \tag{2.4}$$

- **Pressure-velocity coupling**

In order to enforce the mass conservation $\nabla \cdot \boldsymbol{V}^{n+1} = 0$, the projection method is adopted. It derives from the Helmholtz-Hodge decomposition which states that a vector field $\boldsymbol{V}^*$ can

be decomposed in a solenoidal field $\boldsymbol{V}$ (i.e. $\nabla \cdot \boldsymbol{V} = 0$) and an irrotational field derived from the gradient of a scalar potential field Ψ, expressed as follows

$$\boldsymbol{V}^* = \boldsymbol{V} + \nabla \Psi \tag{2.5}$$

The resolution of the momentum equation is then performed in two steps: prediction and correction. First, we consider the predicted velocity field $\boldsymbol{V}^* = (u^*, v^*, w^*)$, which is obtained from eq. (2.4) with an explicit expression of the pressure gradient term:

$$\frac{3u_i^* - 4u_i^n + u_i^{n-1}}{2\Delta t} + NL^{n+1} = -GP^n + \mathrm{Pr}\frac{\partial^2 u_i^*}{\partial x_j^2} \tag{2.6}$$

This velocity field is not a divergence free, but from the Helmholtz-Hodge decomposition, it is possible to define the solenoidal velocity field $\boldsymbol{V}^{n+1}$ as

$$\boldsymbol{V}^{n+1} = \boldsymbol{V}^* - \nabla \Phi \tag{2.7}$$

Then subtracting eq. (2.4) to (2.6), applying the divergence operator on the result and considering that $\nabla \cdot \boldsymbol{V}^{n+1} = 0$, we obtain the following Poisson equation for the potential field Φ

$$\Delta \Phi = \frac{3\nabla \cdot \boldsymbol{V}^*}{2\Delta t} \text{ with } \Phi = p^{n+1} - p^n + \mathrm{Pr}\nabla \cdot \boldsymbol{V}^* \tag{2.8}$$

Subsequently, solving the problem (2.8) enables to obtain the field $\boldsymbol{V}^{n+1}$ as

$$\boldsymbol{V}^{n+1} = \boldsymbol{V}^* - \frac{2\Delta t}{3}\nabla \Phi \tag{2.9}$$

and to update the pressure as

$$p^{n+1} = p^n + \Phi - \mathrm{Pr}\nabla \cdot \boldsymbol{V}^* \tag{2.10}$$

The Poisson problem is solved by a direct approach using the partial diagonalization of the Laplacian operator. This method is faster than iterative methods but can only be used for convex geometries.

- **Parallelization**

In order to increase the solver performances, the code SUNFLUIDH is parallelized through an MPI domain decomposition, which is used in the context of large-scale simulations requiring large memory resources.

The domain decomposition is carried out according to a Cartesian topology, as presented in Figure 2.2. Each element of subdomains is assigned to a processor through the MPI process. The boundary of a subdomain forms a part of the entire domain boundary, or an interface that communicates with an adjacent subdomain. In order to obtain a good charge balance,

each subdomain contains the same number of nodes, which leads to different sub-domain sizes in the case of an irregular grid distribution.

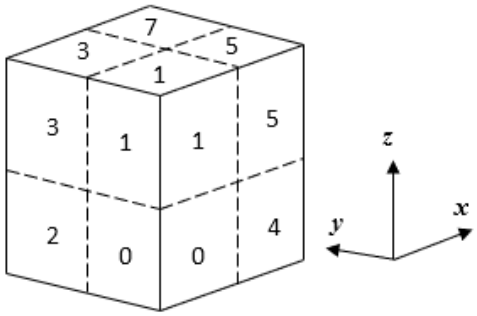

Figure 2.2. Example of domain decomposition in a 3D cubic cavity with a Cartesian topology $2\times2\times2$ for 8 processors.

The mesh distribution of each subdomain is defined in the same way as for the complete domain, that is internal cells and fictive cells that serve as overlaps between two adjacent subdomains to ensure the continuity at the interface. For the evaluation of the explicit terms in the equations, the fictive cells of the subdomains are updated at each time step. To decouple the problem, the Schur complement method is used to calculate the variables at the interfaces.

2.1.3 Numerical approaches for solving the RTE

For a radiative participating medium, the general problem of radiative heat transfer entails determining the radiative intensity from RTE. A brief description of several approaches to resolve RTE are introduced below.

- **The Spherical Harmonics Method (PN-approximation)**

First proposed by Jeans (1917), this method approximates the radiative intensity through a series of arbitrary high-order spherical harmonic functions. The RTE equations are then transformed into a set of simultaneous partial differential equations. The most commonly used is the P_1-approximation for optically thick media. The advantage of this method is the conversion of the governing equations to relatively simple partial differential equations. But the low-order approximations are usually only accurate in media with near-isotropic radiative intensity. For higher-order approximations, the accuracy is only weakly improved while the mathematical complexity increases extremely rapidly (Modest, 2003).

- **The Monte Carlo Method**

The Monte Carlo method is based on the statistical characteristics of physical processes. It considers that a large number of photon bundles carrying a fixed amount of radiative energy are emitted in the system. The history of these photon bundles is traced until the energy

carried is absorbed at a certain point in the participative media or at the wall, or until it exits the system. The departure point, propagation direction, spectral frequency of the ray and the point where the energy is absorbed are independently and randomly chosen according to given distribution functions. A detailed explanation of the Monte-Carlo method is given in references (Howell, 1969; Modest, 2003).

The Monte Carlo method is well-known for its high accuracy resolution and it can be easily employed in complicated systems (such as scattering media, absorption spectrum of gas at high resolution…). However, its drawback is the need of a large number of rays to obtain statistically meaningful results. Soucasse et al. (2013) performed a Monte Carlo simulation of real gas radiation in a cavity with a prescribed 3D temperature field. This temperature field was obtained from their previous works (Soucasse et al., 2012), as the steady solution of coupled radiation-convection problem at $\mathrm{Ra} = 3\times10^{7}$. The Monte Carlo simulation was performed with the emission of 6×10^{9} bundles and a mesh of 40^3 cells, and needs approximately 10 minutes (elapsed time) for complete convergence when using 256 processors of a 4.7 GHz IBM power6.

- **The Ray Tracing Method**

The Ray Tracing method consists in discretizing the angular space Ω by generating N_Ω rays from each point r of volume cells, and the RTE equation is solved for each ray. This has been applied in many studies, for example, Goutiere et al. (2000), effecting an assessment of gas models in a 2D enclosure, and Soucasse et al. (2012), simulating a coupled flow in a differentially heated cavity with a real gas (ADF model) at $\mathrm{Ra} = 10^{6}$. Soucasse et al. (2012) used an angular discretization of 3600 directions and an 81^3 points mesh, which results in an elapsed time of 170 h with 94 processors with a 4.7 GHz IBM power6. It indicates that the computations using ray-tracing method is very expensive and this method is not suitable for turbulent flow.

- **The Discrete Ordinate Method (S_N-approximation)**

First proposed by Chandrasekhar (1960), the discrete ordinate method (DOM) is based on a discrete representation of the directional variation of the radiative intensity. The RTE is solved by a set of discrete directions spanning the total solid angle range of 4π. Therefore, the integrals terms over solid angle, such as radiative flux, are approximated by numerical quadratures.

The DOM has been widely used in recent years to solve different thermal radiation problems. For example: (Coelho, 2002), used it for investigating non-gray gas radiation models; (Collin et al., 2005), for the study of radiative transfer in water spray; (Yücel et al., 1989; Colomer et al., 2007; Lari et al., 2011; Ibrahim et al., 2013; Laouar-Meftah et al., 2014),

for radiation-convection coupling in a differentially heated cavity. This method offers a very good compromise between precision and cost in computing time, and will be adopted in this work.

2.1.4 Implementation of DOM (S_N-Approximation)

In the discrete ordinate method, the RTE equation (1.26) with its boundary condition (1.27) are then solved for a set of different directions and the integrals over solid angle are replaced by numerical quadratures according to the relationship below

$$\int_{4\pi} f(\boldsymbol{s}) d\Omega = \sum_{m=1}^{M} \omega_m f(\boldsymbol{s}_m) \tag{2.11}$$

where ω_m are the variable quadrature weights associated with the direction $\boldsymbol{s}_m$, obtained with the Balsara (2001) approach. Thus, the RTE equation and its boundary condition become a system of M linear differential equations ($M = N(N+2)$ for S_N-approximation)

$$\begin{cases} \mu_m \dfrac{\partial I_m(\mathbf{x})}{\partial X} + \eta_m \dfrac{\partial I_m(\mathbf{x})}{\partial Y} + \xi_m \dfrac{\partial I_m(\mathbf{x})}{\partial Z} + \kappa I_m(\mathbf{x}) = \kappa I^b(T(\mathbf{x})) \quad \forall m \in [1,\ M] \\ I(\mathbf{x}_w) = \varepsilon_w I^b(T(\mathbf{x}_w)) + \dfrac{\rho_w}{\pi} \displaystyle\sum_{\boldsymbol{s}_m \cdot \boldsymbol{n}_w < 0} \omega_m \left| \boldsymbol{s}_m \cdot \boldsymbol{n}_w \right| I_m(\mathbf{x}_w) \quad \text{for} \quad \boldsymbol{s}_m \cdot \boldsymbol{n}_w > 0 \end{cases} \tag{2.12}$$

Moreover, the incident radiative flux G, the radiative source term φ_r''' and the net radiative flux at the walls are defined by

$$G = \sum_{m=1}^{M} \omega_m I_m \tag{2.13}$$

$$\varphi_r''' = \kappa [G - 4\pi I^b(T)] \tag{2.14}$$

$$q_r^{net} = \pi \varepsilon_w I^b(T) - \varepsilon_w \sum_{\boldsymbol{s}_m \cdot \boldsymbol{n}_w < 0} \omega_m \left| \boldsymbol{s}_m \cdot \boldsymbol{n}_w \right| I_m \tag{2.15}$$

In order to solve the set of equations (2.12), the finite volume technique is applied to any control volume of each direction $\boldsymbol{s}_m$ (cf. Figure 2.3).

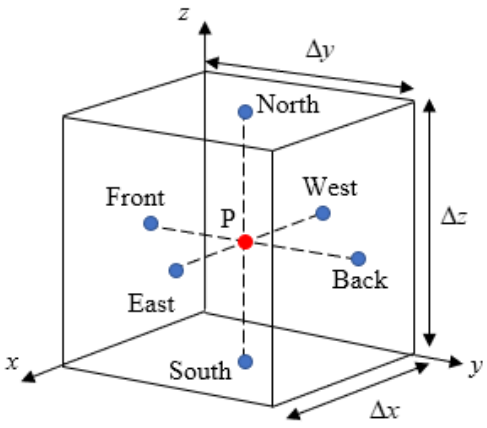

Figure 2.3. Control volume in cartesian coordinates. The RTE is solved only on the node P (red dot). The intensities at the faces (blue dots) are obtained by an intermediate step.

Considering constant radiative properties in the elementary volume ΔV, integration of equations (2.12) results in

$$\begin{cases} \mu_m \int_{\Delta V} \frac{\partial I_m}{\partial X} dV + \eta_m \int_{\Delta V} \frac{\partial I_m}{\partial Y} dV + \xi_m \int_{\Delta V} \frac{\partial I_m}{\partial Z} dV + \kappa \int_{\Delta V} I_m dV = \kappa I^b \int_{\Delta V} dV \\ \int_{\Delta S} I_w d\Gamma = \varepsilon_w I^b \int_{\Delta S} d\Gamma + \frac{\rho_w}{\pi} \sum_{\boldsymbol{s}_m \cdot \boldsymbol{n}_w < 0} \omega_m \left| \boldsymbol{s}_m \cdot \boldsymbol{n}_w \right| \int_{\Delta S} I_m d\Gamma \end{cases} \tag{2.16}$$

and to the form (2.17) when applying the finite volume approach.

$$\begin{cases} \mu_m (I_E^m - I_W^m) A_x + \eta_m (I_B^m - I_F^m) A_y + \xi_m (I_N^m - I_S^m) A_z + \kappa I_P^m \Delta V = \kappa I_P^b \Delta V \\ I_w = \varepsilon_w I_w^b + \frac{\rho_w}{\pi} \sum_{\boldsymbol{s}_m \cdot \boldsymbol{n}_w < 0} \omega_m \left| \boldsymbol{s}_m \cdot \boldsymbol{n}_w \right| I_m \end{cases} \tag{2.17}$$

(A_x, A_y, A_z) are the surfaces areas of the control volume along the directions (x, y, z), I_P is the intensity at the central node of the control volume. (I_E, I_W, I_B, I_F, I_N, I_S) are the intensities at the faces of the control volume and I_w the incident intensity at the wall.

In order to obtain the relationships between the intensity at the node and at the faces read, we use the following interpolation schemes

$$\begin{aligned} I_p &= I_W + a(I_E - I_W) \\ &= I_S + b(I_N - I_S) \\ &= I_F + c(I_B - I_F) \end{aligned} \tag{2.18}$$

The choice of the factors (a, b, c) determine different spatial differencing schemes:

Step scheme ($a = b = c = 1$). This is the simplest first order spatial differencing scheme, stable but numerically diffusive.

Diamond scheme ($a = b = c = 0.5$). This is a second order interpolation scheme, but which can induce spatial oscillations, leading to physically impossible negative intensities at the control volume faces.

Lathrop scheme. The Lathrop scheme (Lathrop, 1969) is a variable weighted difference scheme with a limiter, which can locally switch to the step scheme in order to avoid the appearance of negative intensities. For 3D case, the factors in Lathrop scheme are given by

$$a = \max(0.5,\ 1 - \frac{|\mu_m| A_x}{\beta \Delta V + 2|\eta_m| A_y + 2|\xi_m| A_z}) \tag{2.19}$$

$$b = \max(0.5,\ 1 - \frac{|\eta_m| A_y}{\beta \Delta V + 2|\mu_m| A_y + 2|\xi_m| A_z}) \tag{2.20}$$

$$c = \max(0.5,\ 1 - \frac{|\xi_m| A_z}{\beta \Delta V + 2|\mu_m| A_y + 2|\eta_m| A_z}) \tag{2.21}$$

Finally, combining (2.17) and (2.18), the intensity at node P is obtained by

$$I_P^m = \frac{\lambda_x I_W^m + \lambda_y I_F^m + \lambda_z I_S^m + \Delta V \kappa I_P^b}{\lambda_x + \lambda_y + \lambda_z + \kappa \Delta V} \tag{2.22}$$

where $\lambda_x = |\mu_m| A_x / a$, $\lambda_y = |\eta_m| A_y / b$ and $\lambda_z = |\xi_m| A_z / c$.

Once I_P^m is obtained at the current cell (i, j, k), the intensities at the faces of the control volume are transmitted to the neighboring cells through

$$\begin{cases} I_W(i+1, j, k) = I_E(i, j, k) \\ I_S(i, j+1, k) = I_N(i, j, k) \\ I_F(i, j, k+1) = I_B(i, j, k) \end{cases} \tag{2.23}$$

To solve the RTE in the global domain, a sweeping method is used as illustrated in Figure 2.4 for a 2D case. It supposes that the 2D computation domain is swept for j varying from 1 to N_j . For each value of j , i varying from 1 to N_i when $\mu_m > 0$ and $\eta_m > 0$. For negative cosine directors, the orientation of the faces as well as the dependence of the indices for the sweeping are changed according to the direction of $\boldsymbol{s}_m$, as shown in Figure 2.5. The dependence of the indices in a 3D case for different directions $\boldsymbol{s}_m$ is given in Table 2.1.

From a computational point of view, radiation and convection are solved on the same grids, but the radiative problem is solved every 5 convective time steps. The RTE is solved by an iterative process repeated until the absolute residual between two steps of the sum of the wall radiative fluxes and the volumetric radiative source over the global domain is less than 5×10^{-5} .

	i_{min}	i_{max}	i_{step}		j_{min}	j_{max}	j_{step}		k_{min}	k_{max}	k_{step}
$\mu_m > 0$	1	N_i	1	$\eta_m > 0$	1	N_j	1	$\xi_m > 0$	1	N_k	1
$\mu_m < 0$	N_i	1	-1	$\eta_m < 0$	N_j	1	-1	$\xi_m < 0$	N_k	1	-1

Table 2.1. Dependence of indices in a 3D case for different directions $\boldsymbol{s}_m$.

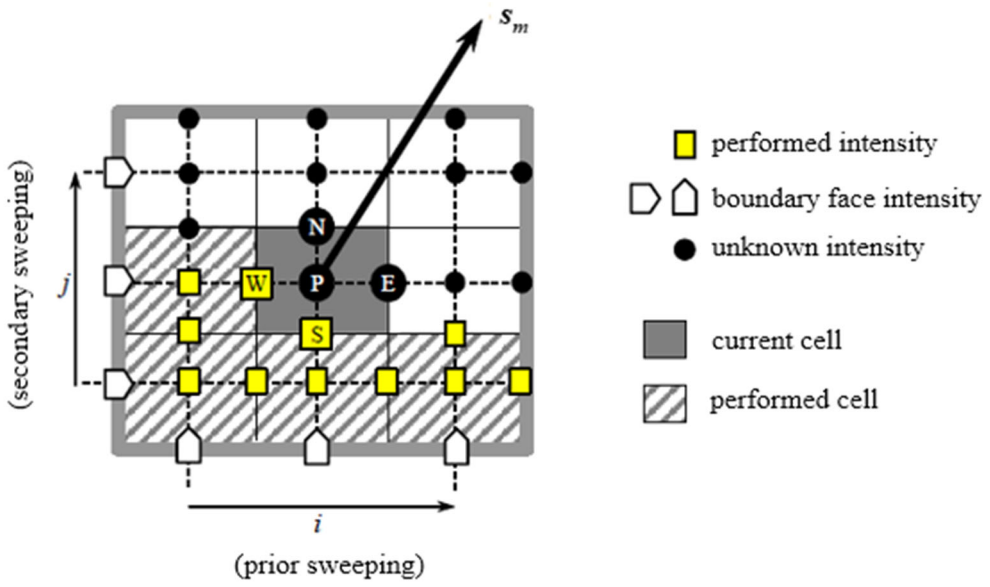

Figure 2.4. Resolution of the RTE by sweeping the computation domain. (From Denis Lemonnier course on radiation phenomena-ISAE-ENSMA).

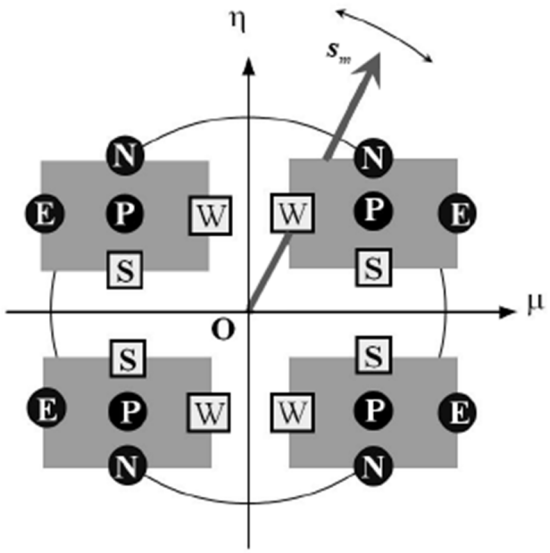

Figure 2.5. Orientation of the control volume according to the direction $\boldsymbol{s}_m$. (From Denis Lemonnier course on radiation phenomena-ISAE-ENSMA).

2.2 Code Validation

2.2.1 2D plume

We first consider a 2D plume, previously investigated in the works of Desrayaud and Lauriat (1993) and Bastiaans et al. (2000). They considered a plume generated by a point source at the non-dimensional position $(x_s,\ z_s) = (0.5,\ 0.25)$ in a square enclosure. The top and bottom boundaries are maintained at a given temperature T_0, while the lateral boundaries are adiabatic. The development of the flow from rest could be used to confirm the grid convergence by analyzing the time evolution of the dipole height, proposed by Bastiaans et al.

$$h = z_s + \frac{\int_0^1 \int_0^1 \omega^2 (z - z_s) dx dz}{\int_0^1 \int_0^1 \omega^2 dx dz} \tag{2.24}$$

where ω is the vorticity.

Figure 2.6 plots the results obtained at Rayleigh numbers equal to 10^6 and 2.7×10^7 for three different uniform grids 65^2, 129^2 and 261^2. The time evolutions of the dipole height match well for the three resolutions at $\mathrm{Ra} = 10^6$. Although a slight time shift is present at $\mathrm{Ra} = 2.7\times10^7$ in the early stages for the lower resolution 65^2, the three grids produce the same long-term evolution with a relative difference less than 1%.

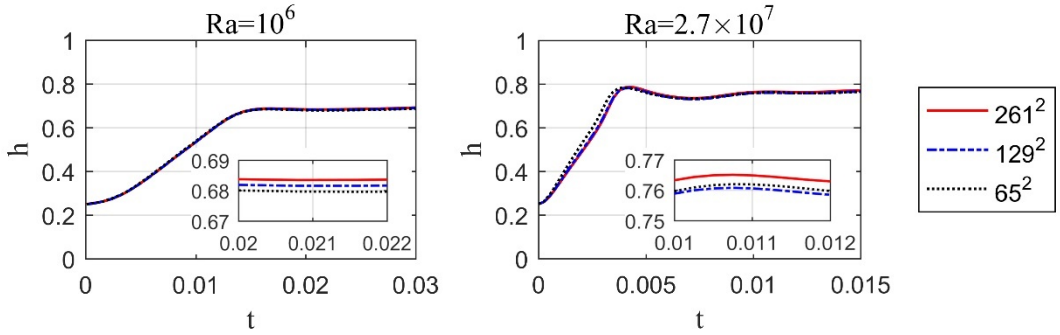

Figure 2.6. Time evolution of the dipole height for grid resolutions [65^2; 129^2; 261^2] at $\mathrm{Ra} = 10^6$ and 2.7×10^7.

Furthermore, Desrayaud and Lauriat (1993) highlighted a transition of the 2D plume from stationary to mono periodic motion through a Hopf bifurcation. They determined the value of the critical Rayleigh number (Ra_c) close to 3.0×10^7 by linear extrapolation of the square of the amplitudes for velocity and heat flux fluctuations to a zero value. Later on, Bastiaans et al. (2000) obtained the critical value of 2.8×10^7 by using a more accurate spectral element method than the finite volume method used by Desrayaud and Lauriat.

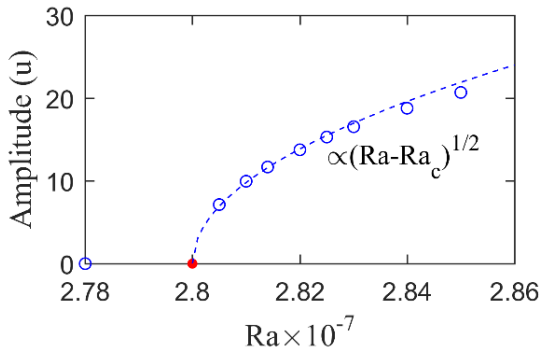

Figure 2.7. Bifurcation diagram for the 129^2 grid resolution.

In the present study, a linear extrapolation method is applied to the square of the *u*-velocity oscillations for the uniform 65^2, 129^2, and 261^2 points grids leads to respective Ra_c values of 2.782×10^7, 2.799×10^7 and 2.815×10^7, very close to the one obtained by Bastiaans et al. (2000). Figure 2.7 presents the bifurcation diagram for the 129^2 grid resolution obtained for the horizontal velocity fluctuations at the point (0.25, 0.5). It confirms that the amplitude of the velocity fluctuations behaves like $(Ra - Ra_c)^{1/2}$, and the supercritical nature of the Hopf bifurcation as stated by Desrayaud and Lauriat.

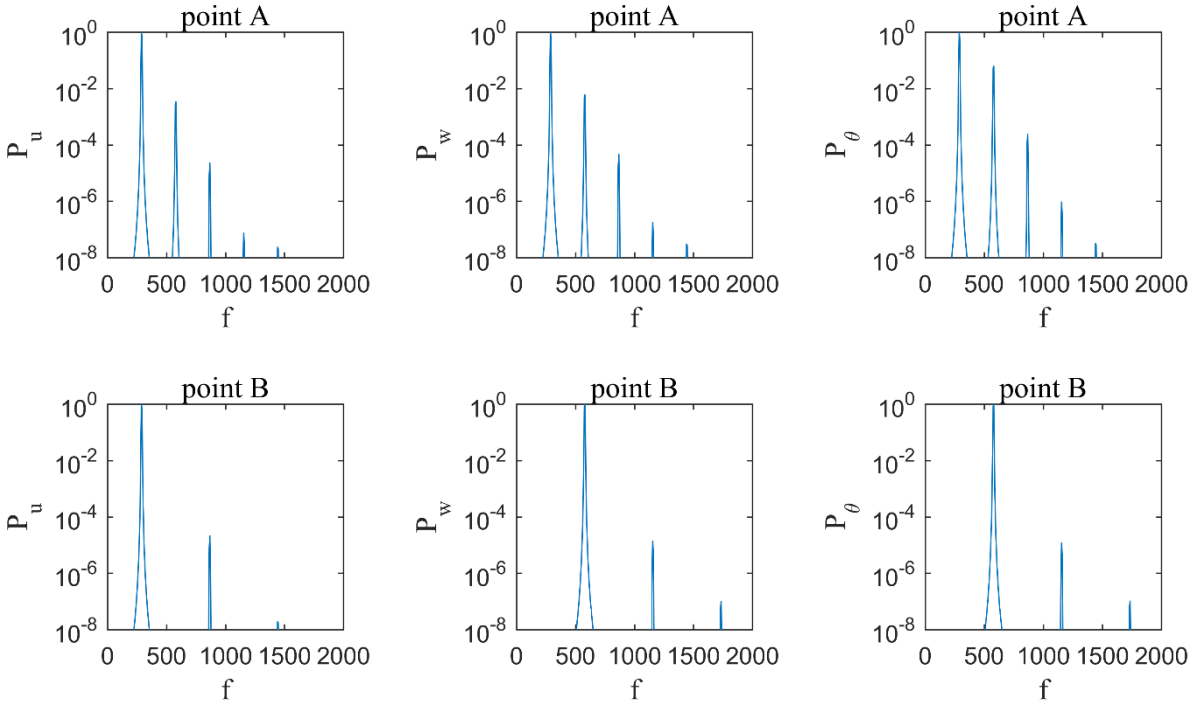

Figure 2.8. Periodic flow at $Ra = 2.81\times10^7$. Density power spectra of u, v and θ at the monitoring points A and B.

Above the critical Rayleigh value, the dynamic behavior of the oscillating flow can be examined by analysing the power spectra of fluctuating parameters. The spectra are estimated through a fast Fourier transform (FFT) algorithm with an oversampled time series data to

yield a sufficient effective sampling period Δt_e. The length of FFT has been chosen at $N = 4096$ points to obtain a good spectral resolution. Desrayaud and Lauriat (1993) obtained the fundamental frequency and its harmonics by applying power spectra to the periodic flow. In the present work, the normalized power spectra are calculated for the velocity components u, v and temperature θ at two monitoring points A and B (cf. Figure 2.9) for $\mathrm{Ra} = 2.81\times10^7$ with the 129^2 grid resolution, as shown in Figure 2.8.

At the point A, the frequency peaks are at the same positions for velocity components and temperature spectra, indicating a pure periodic flow whose fundamental frequency is $f_0 = 287.6$. For the point B, located along the vertical centerline, only f_0 and its even harmonics are present for u, while they are absent for w and θ. The absence of the even or odd harmonics in spectra is also found in Desrayaud and Lauriat (1993). The reason is the symmetry of the periodical fluid motion with respect to the centerline $x = 0.5$.

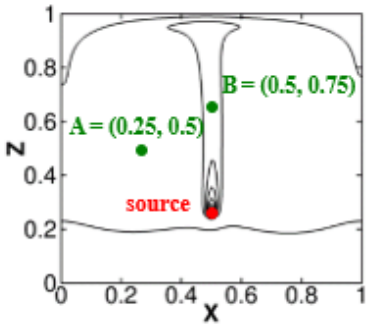

Figure 2.9. Monitoring points A and B and iso-contours of instantaneous temperature field at $\mathrm{Ra} = 2.81\times10^7$.

2.2.2 Validation of the DOM method

Validation of the implementation of the radiative module in SUNFLUIDH, is done by considering the pure radiation case considered by Soucasse et al. (2012). It consists in a cubic cavity of size $H = 1$ m, with perfectly diffuse gray walls of emissivity $\varepsilon = 0.5$. The cavity contains a gray gas with absorption coefficient $\kappa = 1\ \mathrm{m}^{-1}$. All the walls are maintained at $T_0 = 300$ K, while the temperature field in the cavity is imposed according to:

$T(x, y, z) = T_0 + \Delta T \cdot exp(-(x-x_0)^2 - (y-y_0)^2 - (z-z_0)^2)$, with $\Delta T = 10$ K and $(x_0, y_0, z_0) = (0.25, 0.25, 0.25)$.

Soucasse et al. (2012) performed the simulation with a Monte Carlo method, which can be considered as a reference method due to its accuracy, on a uniform grid of 42^3 cells. In the present work, the simulation is based on DOM method with a uniform grid of 80^3 cells. Figure 2.10 and Figure 2.11 compare the iso-contours of the radiative flux in the planes $x = 0$ m and $x = 1$ m, as well as the radiative volumetric power in the planes $x = 0.25$ m and

$x = 0.75$ m. Our results using S_8-approximation show a very good qualitative agreement with those obtained by Soucasse et al. This is also confirmed by radiative wall flux and radiative volumetric power profiles plotted in Figure 2.12, which presents a very good agreement with those obtained by the Monte-Carlo method.

A comparison between S_8- and S_{12}-approximation (involving respectively 80 and 168 discrete directions) is made in terms of radiative flux and radiative volumetric power along different x-lines. As shown in Figure 2.13, it is found that the S_8-approximation is sufficient to resolve the radiative transfer problem.

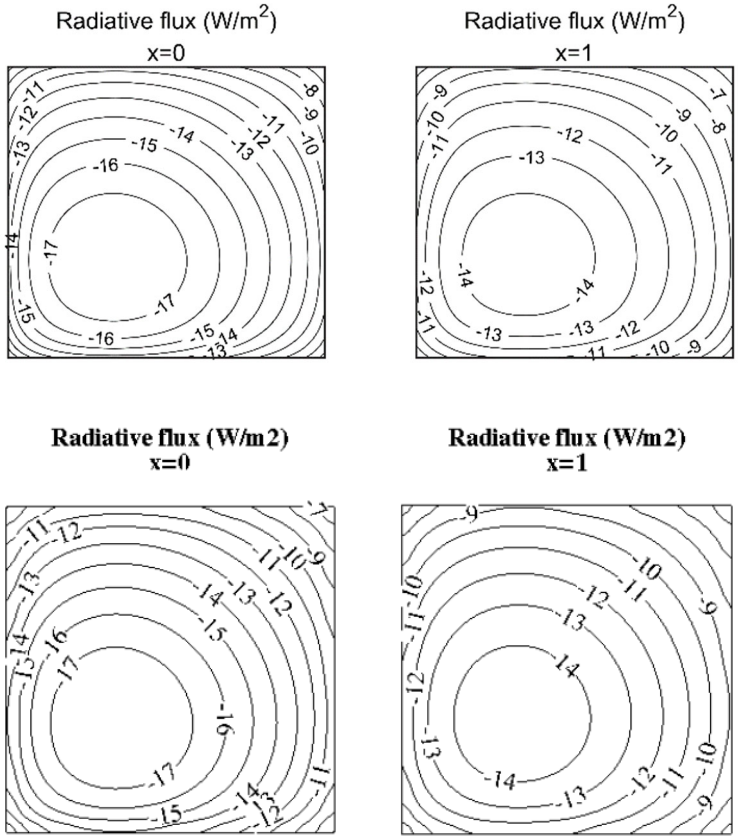

Figure 2.10. Iso-contours of the radiative flux at the planes $x = 0$ m and $x = 1$ m. (Top) present study, (bottom) reference case.

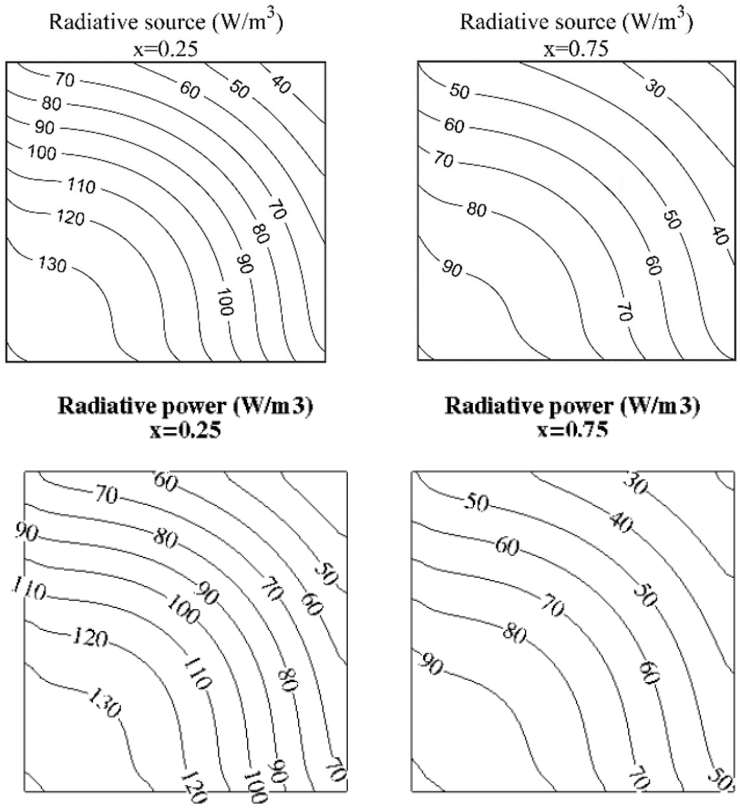

Figure 2.11. Iso-contours of the radiative volumetric power at the planes $x = 0.25$ m and $x = 0.75$ m. (Top) present study, (bottom) reference case.

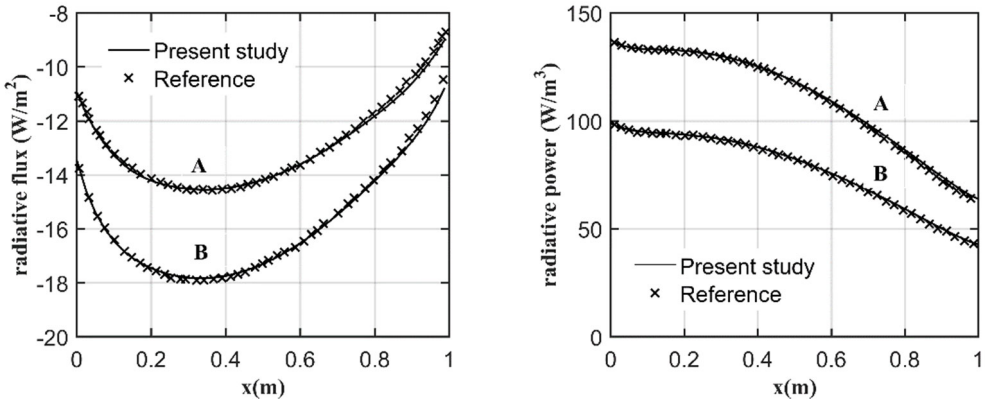

(a) radiative wall flux at (A) $y = 0.25$ m, $z = 1$ m and (B) $y = 0.25$ m, $z = 0$ m.

(b) volumetric radiative source at (A) $y = 0.25$ m, $z = 0.25$ m and (B) $y = 0.25$ m, $z = 0.75$ m.

Figure 2.12. Profiles of radiative net flux at the walls and volumetric radiative power, compared with the results of Soucasse et al. (2012).

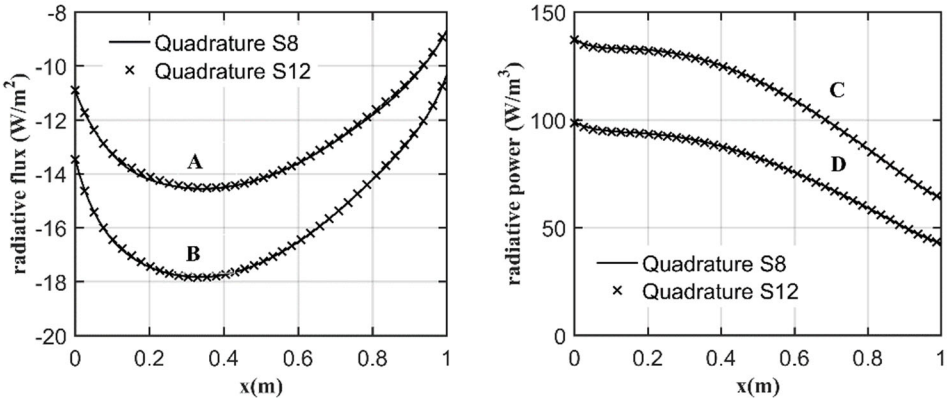

Figure 2.13. Comparison of S_8- and S_{12}-approximation, (a) profiles of radiative wall flux along the lines A(x, 0.25 m, 1 m) and B(x, 0.25 m, 0 m), (b) profiles of radiative volumetric power along the lines C(x, 0.25 m, 0.25 m) and D(x, 0.25 m, 0.75 m).

2.2.3 Validation of the real gas model

The real gas model is validated in this section by performing a case of convection-radiation coupling in a differentially heated cavity, also based on Soucasse et al. (2012). The configuration considers a cubic cavity ($H = 1$ m) filled with a real gas mixture air/H_2O/CO_2 at atmospheric pressure and a mean temperature $T_0 = 300$ K.

The simulation is carried out at $\mathrm{Ra} = 10^6$ with the Planck number equals to $\mathrm{Pl} = 6.23 \times 10^{-7}$ and the temperature ratio $\Theta_0 = 27522$. Among the works presented by Soucasse et al. (2012), we applied the configuration (B) that considers a participating medium with emissivity $\varepsilon = 1$ on the vertical isothermal walls and $\varepsilon = 0$ on all the adiabatic walls. In the present case, we only consider an air + H_2O gaseous mixture with ($X_{H_2O} = 2\%$), and not CO_2 as Soucasse et al. did. Note that the air + H_2O mixture is also applied in the works of Billaud et al. (2017), for validation of the SLW model in the same configuration. Neglecting CO_2 in this low T_0 configuration does not affect the results.

Considering the numerical aspects, Soucasse et al. (2012) used a ray tracing method to solve the RTE equation, along with the real gas model ADF. Their calculations were performed on a mesh of 81^3 points within the flow and 40^3 points for the radiation field. In our simulations, the spatial domain is discretized with a wall-refined 100^3 cells repartition both for the flow and the radiative problem. The angular domain decomposition is performed through S_8 quadrature set and the spectral modelling of the real gas considers 8 gray gases. Table 2.2 gives a comparison of different local or global quantities. It shows a good agreement between the present work and the reference. The y-averaged temperature profiles along the lines $z = 1$ and $x = 0.5$, as well as the volumetric radiative power ($-\varphi_r'''$) profiles reported in Figure 2.14 and Figure 2.15 agree very well with those obtained by the ray tracing method and prove the ability of our method in dealing with real gas radiative problems.

Case	present	reference
$\mathrm{Nu}_{c,\,hot}$	7.51	7.55
$\mathrm{Nu}_{r,\,hot}$	121.28	120.58
$u_{\max}$	0.232	0.231
$v_{\max}$	0.059	0.060
$w_{\max}$	0.296	0.296
Elapsed time	5h	170h
Processors	8	94

Table 2.2. Convective and radiative Nusselt numbers, velocity maximums, and elapsed computing time, compared with Soucasse et al. (2012).

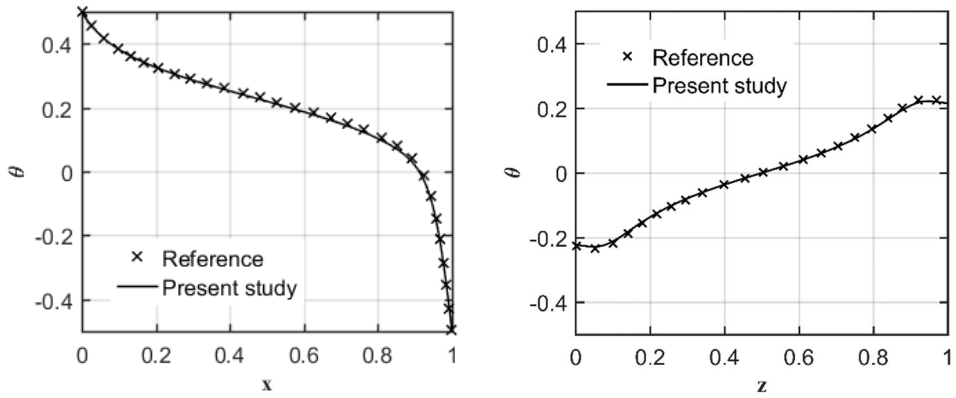

Figure 2.14. Left: temperature profile at the line (x, $\overline{y}$, 1). Right: vertical temperature profile at the line (0.5, $\overline{y}$, z). Results are compared with Soucasse et al. (2012).

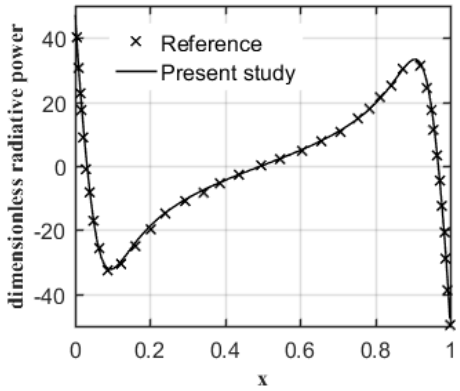

Figure 2.15. Profile of dimensionless radiative volumetric power along the line (x, 0.5, 0.5), compared with Soucasse et al. (2012).

2.3 Conclusion

The numerical methods for solving the convection governing equations and the radiative heat transfers have been introduced in this chapter. The simulations are performed with the CFD software SUNFLUIDH coupled to a DOM module for the radiative problem with either grey gas approximation or SLW model for real gases. The code has been validated first in the case of a confined 2D plume in the pure convective case, through the study of the onset of unsteadiness of the flow compared with existing data. Then the DOM method and the real gas model SLW have been validated in the case of differentially heated cavity by comparison to reference results of the literature. In the next chapter, we will focus on a pure convective 3D plume in a cubic cavity to study the plume behavior at different flow regimes.

Chapter 3
Results for the pure convective situation

3.1 Simulations characteristics

In the following studies, we consider a pure convective plume generated by a line heat source in a confined cubic cavity, as described in section 1.1. This chapter is divided into three parts according to the different flow regimes: steady, transitional and turbulent. The numerical simulations have been carried out at Rayleigh numbers varying from 10^6 to 10^9. Table 3.1 lists a summary of simulations characteristics with corresponding flow regimes.

Regime	**Rayleigh**	**Mesh**	**Grid distribution (x, y, z)**	**Time step**
Steady	10^6	$129\times129\times129$	Uniform	2.0×10^{-5}
Transitional	1.2×10^6	$129\times129\times129$	Uniform	2.0×10^{-5}
	2×10^6			1.6×10^{-5}
	5×10^6			1.0×10^{-5}
	1.2×10^7			7.5×10^{-6}
Turbulent	10^9	$192\times192\times512$	(Tanh, Tanh, Uniform)	3.0×10^{-7}

Table 3.1. Summary of simulations characteristics in pure convective case and corresponding flow regimes.

All the simulations were performed with a fixed time step which corresponds to a maximum CFL number of 0.45. Concerning the grid distribution, we apply first a uniform 129^3 grid for simulations of steady and transitional flows. This mesh distribution is referring to the previous 2D configuration in which the line source occupies one cell in the xz-plane. For the turbulent simulation, we apply a non-uniform grid distribution in order to refine the computational regions close to the line heat source and to the walls by using a hyperbolic tangent law. This grid distribution is checked *a posteriori* with the Grötzbach (1983) requirement (cf. section 1.2.5) and is defined as follows

$$x(0)=0;\;\; x(i)=L\frac{F(i)}{\alpha+(1-\alpha)F(i)} \;\text{ for }\; 2\le i \le N;\;\; x(N+1)=L$$
$$F(i)=\frac{1}{2}[1+\frac{\tanh(\beta(\frac{i-1}{N}-0.5))}{\tanh(\beta/2)}] \qquad (3.1)$$

The parameters used in the non-uniform mesh, and the corresponding minimum and maximum cell sizes are reported in Table 3.2. The *x*-distribution of the grid is divided into 3 sections to refine the regions close to the heat source and lateral walls by providing cell sizes equal to 1.95×10^{-3} and 4×10^{-3}, respectively. We also note that the line source region occupies 4×4 cells in the *xz*-plane which allows a similar *xz*-surface area as the line source defined in the uniform 129^3 grid. In the following, the time series data are monitored at four points (A_1, B_1, A_2, B_2) in planes $y=0.25$ and 0.5. The existence of unsteady solutions (periodic or chaotic) can be assessed by analyzing the power spectra at these monitoring points. Figure 3.1 illustrates their locations on a snapshot of the temperature field at $\mathrm{Ra}=1.2\times10^6$.

Direction	x			y	z
L	0.4961	7.8×10^{-3}	0.4961	1	1
N	94	4	94	192	512
α	0.69	Regular	1.43	1	Regular
β	1.89	Regular	1.89	1.30	Regular
$(\Delta)_{\min}$	1.95×10^{-3}	1.95×10^{-3}	1.95×10^{-3}	4×10^{-3}	1.95×10^{-3}
$(\Delta)_{\max}$	7.25×10^{-3}	1.95×10^{-3}	7.25×10^{-3}	6×10^{-3}	1.95×10^{-3}

Table 3.2. Characterization of mesh distribution at $\mathrm{Ra}=10^9$.

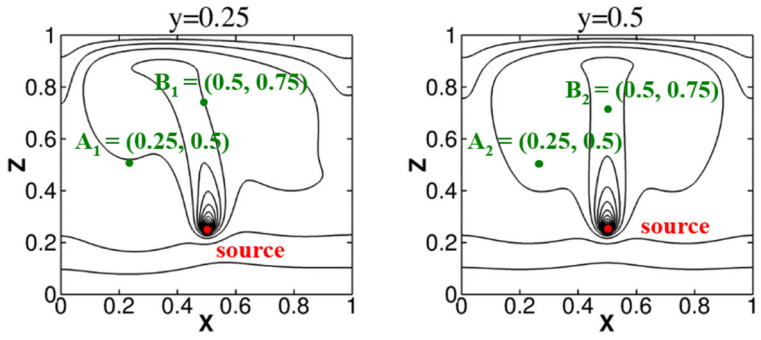

Figure 3.1. Monitoring points $A_{1/2}$ and $B_{1/2}$, the subscripts 1 and 2 represent planes $y=0.25$ and $y=0.5$, respectively. Iso-contours of instantaneous temperature at $\mathrm{Ra}=1.2\times10^6$.

3.2 Steady regime

A 3D steady plume flow at $\mathrm{Ra} = 10^6$ is simulated first and compared to the corresponding 2D one. Figure 3.2 and Figure 3.3 display the distributions of isotherms and streamlines for both cases. The thermal and kinetic fields of the plume (in the vertical mid-plane $y = 0.5$ for the 3D case) are very close: two symmetrical large vortices are formed in which the hot fluid moves upward from the heat source, and then descends along the lateral walls to finally feed the plume entrainment region close to the source.

Besides, the temperature field inside the bottom region strongly depends on the thermal boundary conditions at the bottom wall, and presents a stagnant fluid layer below the source as denoted by the quasi-horizontal thermoclines. The isotherms reported in Figure 3.2 (c) at the horizontal mid-plane ($z = 0.5$) indicate that the flow structure is mainly 2D in a large central part of the cavity ($0.2 < y < 0.8$), while 3D effects remains limited to the vicinity of the front and rear walls.

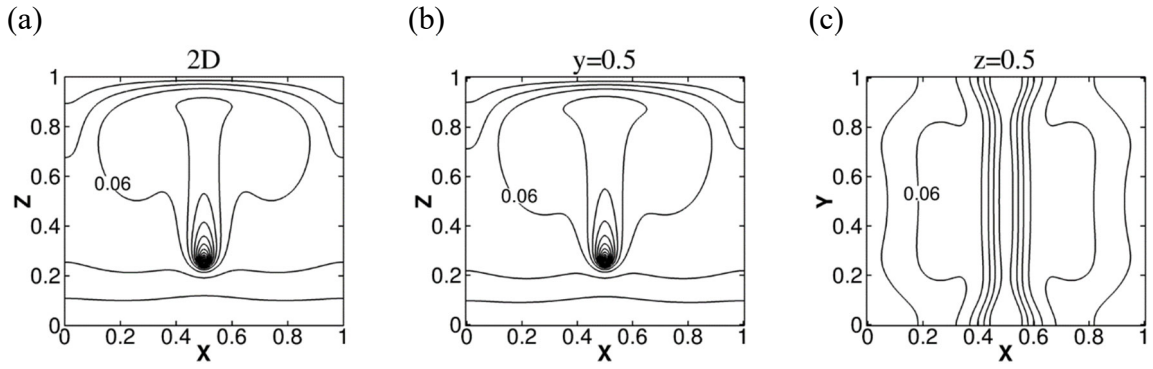

Figure 3.2. $\mathrm{Ra} = 10^6$. Isotherms for (a) 2D case, and (b) 3D case in the vertical mid-plane ($y = 0.5$), (c) 3D case in the horizontal mid-plane ($z = 0.5$). Contour levels (a), (b) (0.02:0.02:0.4), and (c) (0.05:0.01:0.1).

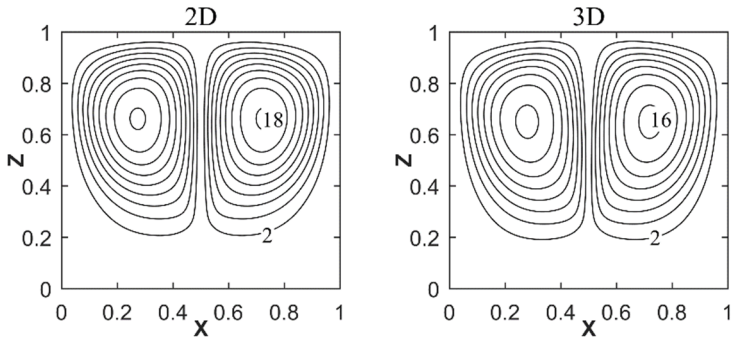

Figure 3.3. $\mathrm{Ra} = 10^6$. Stream function contours for 2D and 3D case in the mid-plane $y = 0.5$.

3.3 Transitional regime

3.3.1 Critical Rayleigh number

Increasing the Rayleigh number to 1.2×10^6, we observed an unsteady flow, which remains present for higher Rayleigh values. This indicates the existence of a transition to unsteadiness in the range of $\mathrm{Ra}=10^6$ to 1.2×10^6. Figure 3.4 shows the bifurcation diagram obtained from the amplitude of the fluctuations of horizontal velocity u at the point A_2 (cf. Figure 3.1). As observed in the 2D case, the amplitude of the fluctuations behaves like $(\mathrm{Ra}-\mathrm{Ra}_c)^{1/2}$, which is a typical feature of Hopf bifurcation. By using the linear extrapolation method on the square of the horizontal velocity fluctuations, the critical value is obtained at $\mathrm{Ra}_c\approx1.01\times10^6$, that is a decade smaller than in the 2D case. This proves that the 3D flow is less stable than the 2D case.

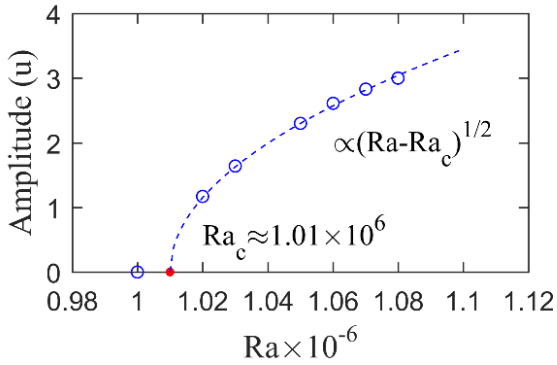

Figure 3.4. Bifurcation diagram of the amplitude of the horizontal velocity fluctuation at the point A_2.

$\mathrm{Ra}\times10^{-6}$	f	$(\mathrm{Ra}\cdot\mathrm{Pr})^{1/2}/f$
1.02	73.88	11.51
1.03	74.51	11.47
1.05	75.11	11.49
1.06	74.16	11.69
1.07	74.77	11.65
1.08	74.76	11.71

Table 3.3. Frequencies at the monitoring point A_2 compared to the Brunt Vaïsälä frequency.

The Hopf bifurcation can also be evaluated by the relationship between the Brunt Vaïsälä frequency and the oscillating frequency. According to eq. (1.19), the ratio f_{BV}/f is nearly constant around the threshold, and the Brunt Vaïsälä frequency f_{BV} can be expressed as $(\mathrm{Ra}\cdot\mathrm{Pr})^{1/2}$ by applying an approximation of the stratification value. Table 3.3 reports the

dimensionless frequencies of the horizontal velocity oscillation at the point A_2 in the vicinity of Ra_c. It shows that the present frequencies well support the Brunt Väisälä relationship.

3.3.2 Periodic regime description

Figure 3.5 presents the time evolution, starting from rest, of the total 2D Nusselt number Nu_{total}^{2D} at $Ra = 1.2\times10^6$. It can be seen that in a first stage, the total heat flux at the walls increases until $Nu_{total}^{2D} = 1$. Then, after a long apparent steady state, an oscillating motion appears with a period $T(Nu_{total}^{2D}) \approx 0.013$. The normalized spectrum of Nu_{total}^{2D} reported in Figure 3.5 shows a fundamental frequency $f(Nu_{total}^{2D})$ equals to 76.9, and its harmonics.

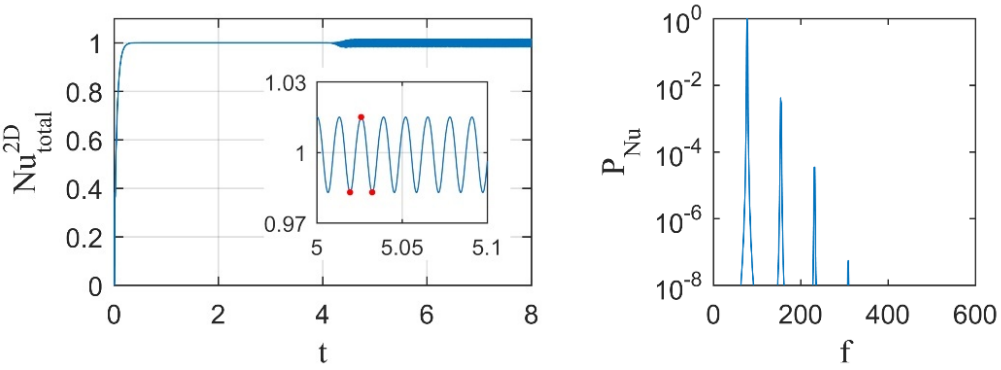

Figure 3.5. Periodic flow at $Ra = 1.2\times10^6$. Time evolution (left) and power spectrum (right) of the total Nusselt number Nu_{total}^{2D}. The red points are marked to identify three specific instants displayed in Figure 3.6.

Figure 3.6 displays the snapshots of the thermal fields in three vertical planes $y = 0.25$, 0.5 and 0.75 at three different instants within one period, as marked in Figure 3.5 (red dots). A swaying motion is clearly visible in the planes $y = 0.25$ and 0.75 with opposite spatial phases and antisymmetric thermal distributions with respect to the vertical centerline $x = y = 0.5$. For symmetry reasons this swaying motion is not observed in the mid-plane $y = 0.5$, but a pulsating growth of the plume.

To explain this antisymmetric swaying motion along the *y*-direction, the iso-surfaces $\theta = 0.09$ are illustrated in Figure 3.7 at the same three instants. We observe that a stationary plane wave propagates along the direction of the line heat source with a half-wavelength close to the cavity depth. It confirms that the 3D plume not only sways in the plane perpendicular to the source direction but also meanders in the cavity, as observed in the experimental works of Eichhorn and Vedhanayagam (1982) and Urakawa et al. (1983). Moreover, the plume shape is found antisymmetric along the *y*-direction. Its upward extension is almost constant in the central part of the cavity ($0.2 < y < 0.8$), while the 3D

effects near the front ($y = 0$) and rear wall ($y = 1$) correspond to the suction of the plume through the wall.

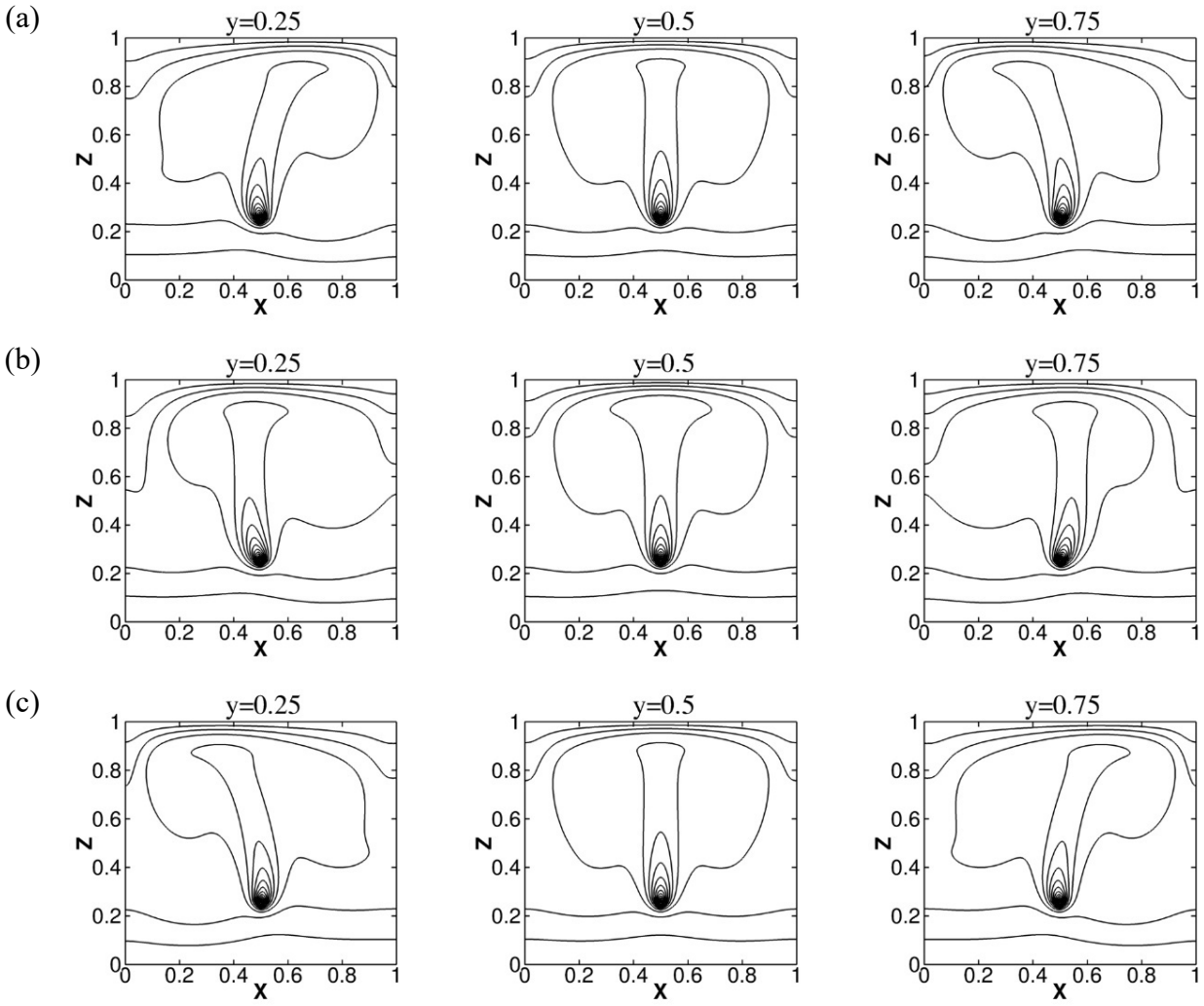

Figure 3.6. $\mathrm{Ra} = 1.2 \times 10^6$. Snapshots of the temperature fields at three depths $y = [0.25;\ 0.5;\ 0.75]$ for three different instants marked in Figure 3.5 by red points. Contour levels (0.02:0.02:0.4).

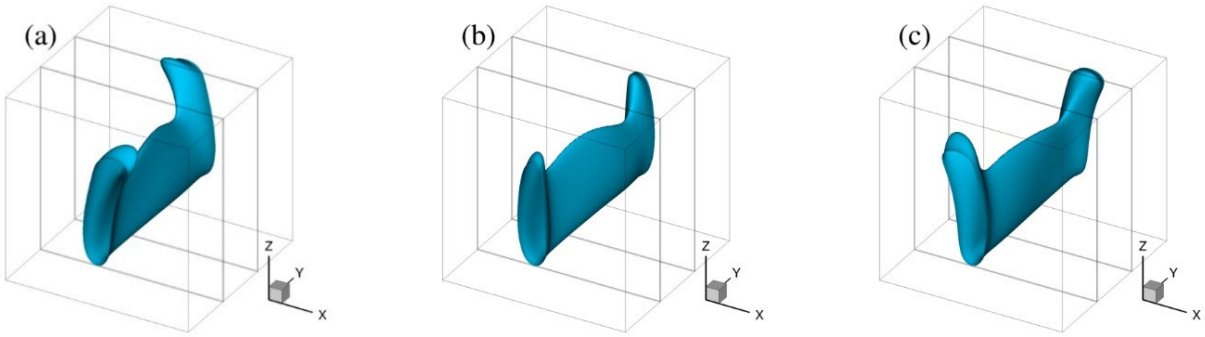

Figure 3.7. $\mathrm{Ra} = 1.2 \times 10^6$. Iso-surfaces of $\theta = 0.09$ at three different instants. (marked by red points in Figure 3.5).

The periodic nature of the swaying motion is then analysed by means of the normalized power spectra in Figure 3.8. The spectra are given for the velocity components u, w and the temperature θ at two monitoring points A_1 and B_1 in a vertical plane ($y = 0.25$) away from the vertical mid-plane. A_1 is placed outside the plume zone while B_1 is inside the plume zone, but far above the heat source (see Figure 3.1 for their exact locations). At the point A_1, the same fundamental frequency and its harmonics are observed in three spectra. The fundamental frequency is located at $f_1 = 38.45$ which characterizes the swaying motion of plume. At the point B_1, only the fundamental and the odd harmonics are present for u while only the even harmonics appear for w and θ. This is due to the symmetry of the periodic motion with respect to the centerline $x = 0.5$.

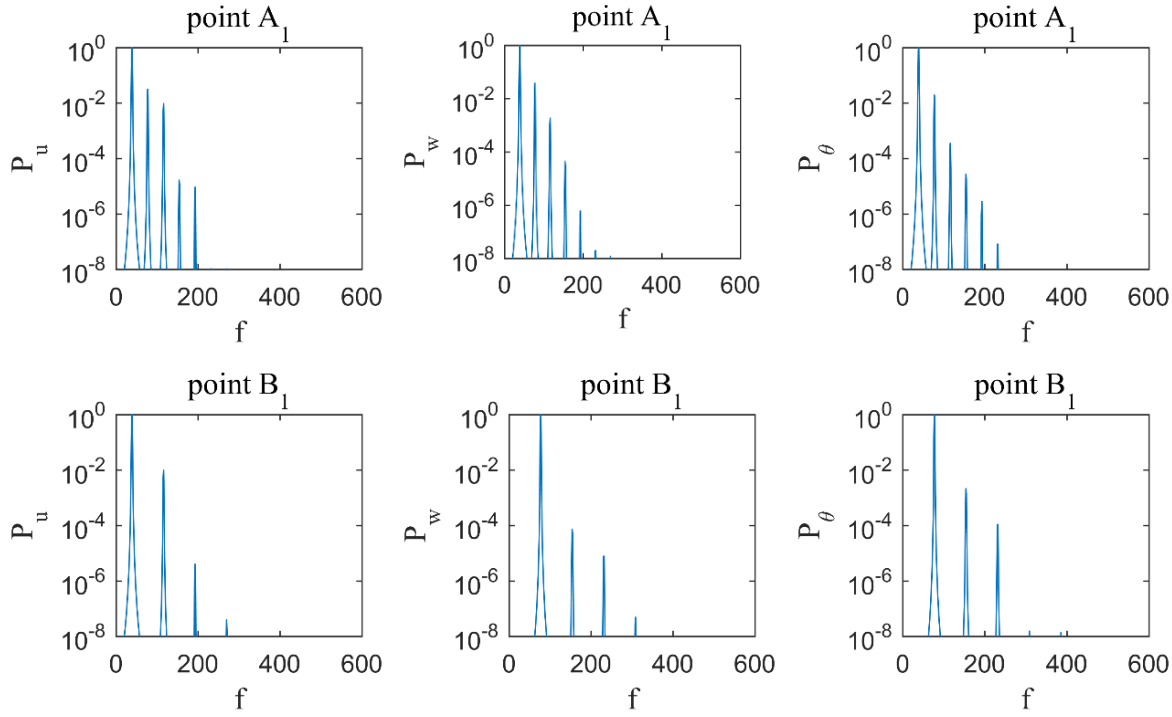

Figure 3.8. $\mathrm{Ra} = 1.2\times10^6$. Normalized density power spectra for u, w and θ at the monitoring points in the plane $y = 0.25$.

Point	Component	f_1	$2f_1$	$3f_1$	$4f_1$	$5f_1$
A_1	u	38.45	76.90	115.35	153.80	192.87
	w	38.45	76.90	115.35	153.80	192.87
	θ	38.45	76.90	115.35	153.80	192.87
B_1	u	38.45		115.35		192.87
	w		76.90		153.80	
	θ		76.90		153.80	

Table 3.4. $\mathrm{Ra} = 1.2\times10^6$. Frequency peaks at the monitoring points in the plane $y = 0.25$.

As shown in Figure 3.6, the swaying plume moves alternatively between the right and left sides of the cavity. Consequently, the horizontal oscillation at point B_1 respects a half-wave symmetry, i.e. $u(t) = -u(t + T_1/2)$ with the period $T_1 = 1/f_1$. This half-wave symmetry is responsible for the disappearance of the even harmonics in u-spectrum at point B_1. As the oscillations for w and θ are repeated twice over one cycle of the swaying motion, their main frequency is twice the fundamental f_1. Figure 3.9 plots the time evolutions of u, w and θ at the monitoring points. It can be seen that the time evolutions of u, w and θ at point B_1 follow the relationships $u(t) = -u(t + T_1/2)$; $w(t) = w(t + T_1/2)$; $\theta(t) = \theta(t + T_1/2)$.

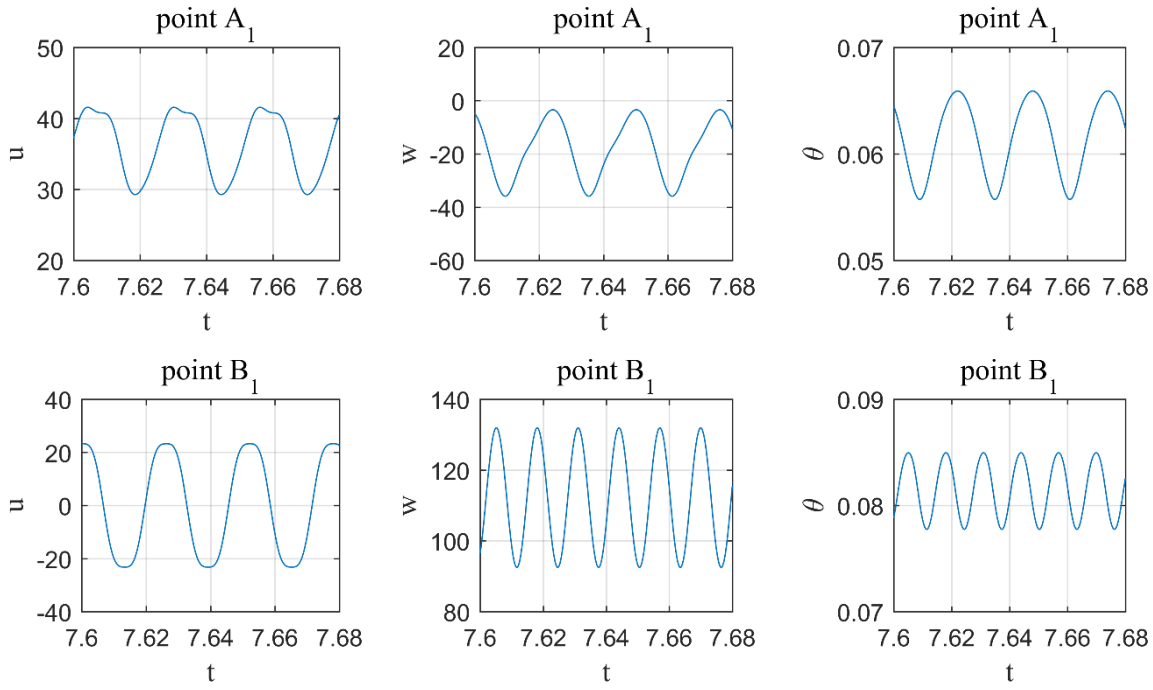

Figure 3.9. $\mathrm{Ra} = 1.2 \times 10^6$. Time evolution for u, w and θ at the monitoring points in the plane $y = 0.25$.

Figure 3.10 and Figure 3.11 present the power spectra of u, w and θ at the monitoring points A_2 and B_2 in the mid-plane $y = 0.5$ which exhibits a pulsating movement. The u-spectrum at point B_2 is not present here because the horizontal oscillation at this location can be neglected (see Figure 3.12). Table 3.5 gives the locations of the frequency peaks in the spectra. We observe that only the even harmonics are present for u, w and θ in the mid-plane, with respect to the antisymmetric mode through the y-direction.

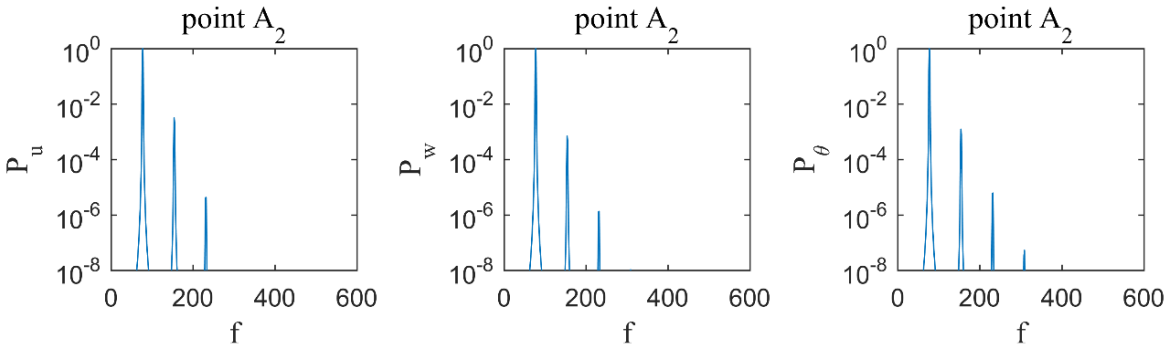

Figure 3.10. $\mathrm{Ra} = 1.2 \times 10^6$. Density power spectra for u, w and θ at the point A_2 in the plane $y = 0.5$.

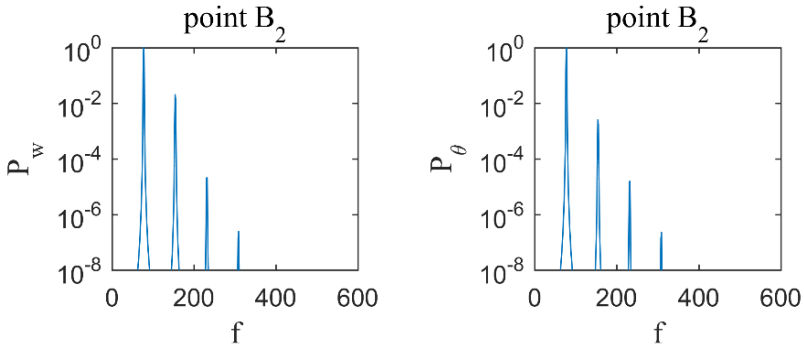

Figure 3.11. $\mathrm{Ra} = 1.2 \times 10^6$. Density power spectra for u, w and θ at the point B_2 in the plane $y = 0.5$.

Point	Variable	$2f_1$	$4f_1$
A_2	u	76.90	153.80
	w	76.90	153.80
	θ	76.90	153.80
B_2	w	76.90	153.80
	θ	76.90	153.80

Table 3.5. $\mathrm{Ra} = 1.2 \times 10^6$. Frequency peaks at the monitoring points in the plane $y = 0.5$.

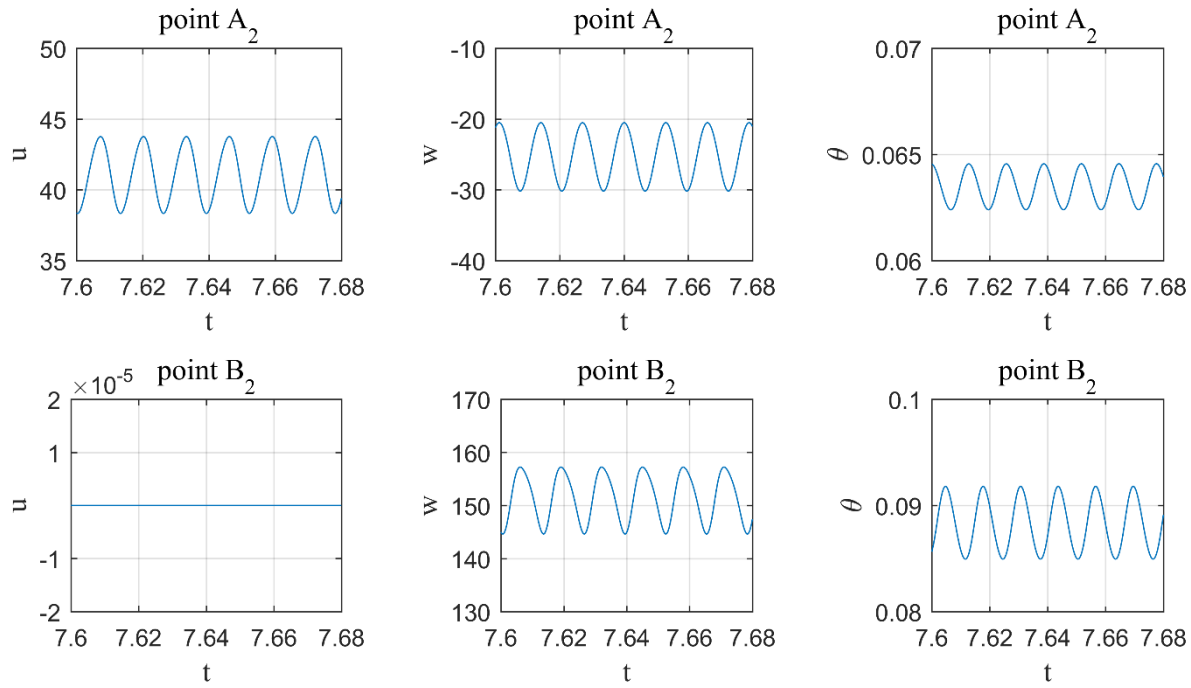

Figure 3.12. $\mathrm{Ra} = 1.2\times10^{6}$. Time evolution for u, w and θ at the monitoring points in the plane $y = 0.5$.

3.3.3 Transition to chaos

In order to observe the transition of plume to chaos, further simulations have been carried out at three Rayleigh numbers $\mathrm{Ra} = 2\times10^{6}$, 5×10^{6} and 1.2×10^{7}. The corresponding power spectra of u, w and θ at the monitoring points A_1 and B_1 in the plane $y = 0.25$ are presented in Figure 3.13 to Figure 3.15, respectively. If dominant frequencies can be well identified in the spectra at $\mathrm{Ra} = 2\times10^{6}$, they progressively disappear with the increase of Ra and the gradual transition to chaos.

At $\mathrm{Ra} = 1.2\times10^{7}$, a dominant frequency peak $f_1 = 84.36$ can still be identified in all spectra at the point A_1 and in the u-spectrum at the point B_1, indicating that the swaying motion of the plume still exists. In addition, the well-known -5/3 Kolmogorov power law seems to be present in a small range of frequency in the velocity spectra at far-field point A_1. It may indicate that the flow inside the cavity is weakly turbulent at $\mathrm{Ra} = 1.2\times10^{7}$. Besides, a decay following a -3 power law appears in the temperature fluctuations spectrum at the monitoring point B_1 located in the plume plane. This slope is a typical feature of turbulent buoyancy induced flows, (Kotsovinos, 1991; Pham et al., 2007) as an example, and is interpreted as a characteristic effect of the buoyancy forces in the conversion of potential energy into kinetic energy (Kotsovinos, 1991). We can notice that the temperature spectrum at the monitoring point in the far-field of the plume (A_1) is affected by both phenomenon: the turbulent behavior of the far field and the buoyancy induced dissipation.

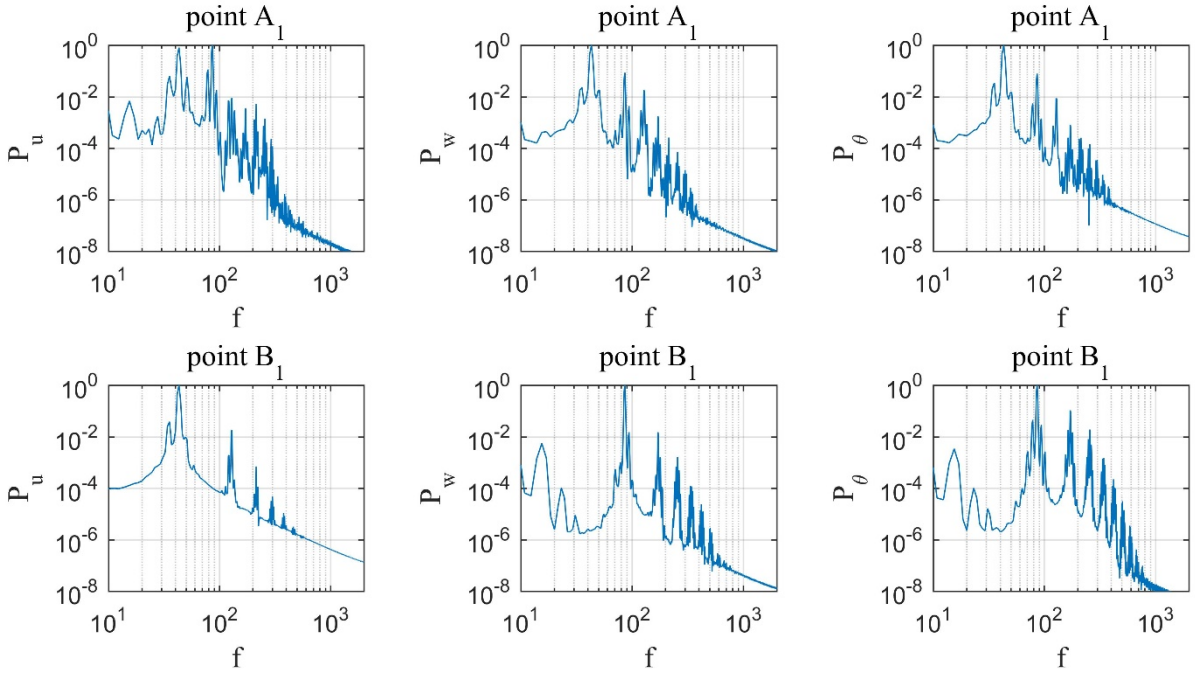

Figure 3.13. $\mathrm{Ra} = 2\times10^{6}$. Density power spectra of velocity components u, w and temperature θ at the monitoring points.

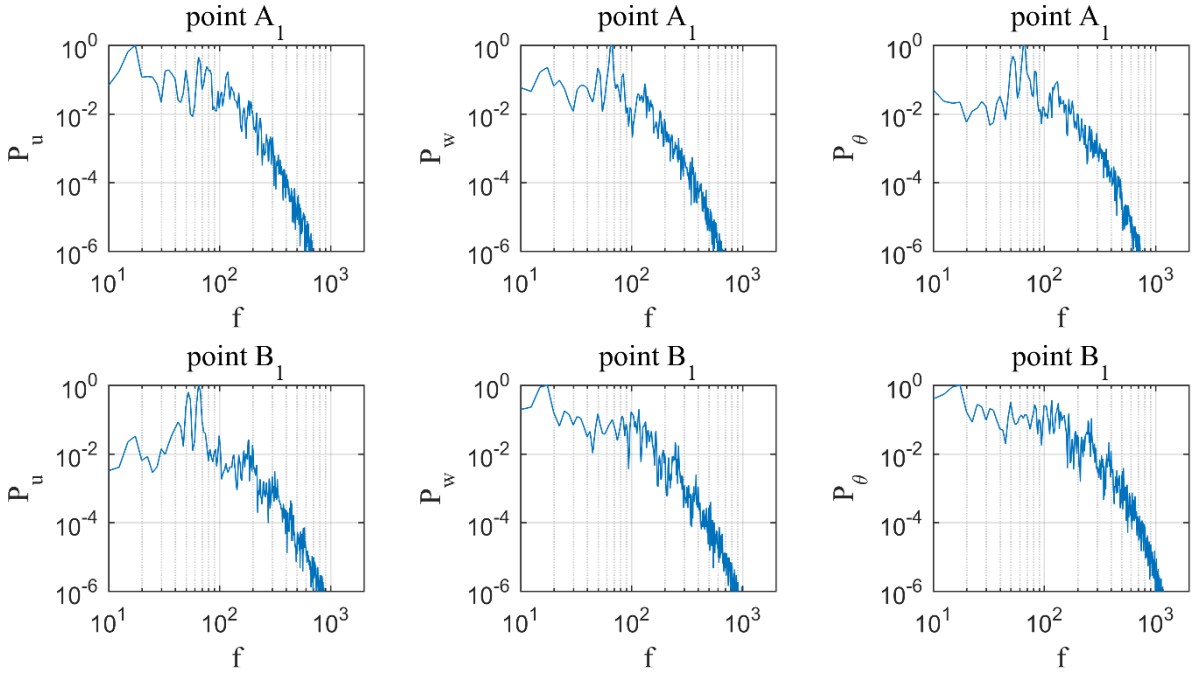

Figure 3.14. $\mathrm{Ra} = 5\times10^{6}$. Density power spectra of velocity components u, w and temperature θ at the monitoring points.

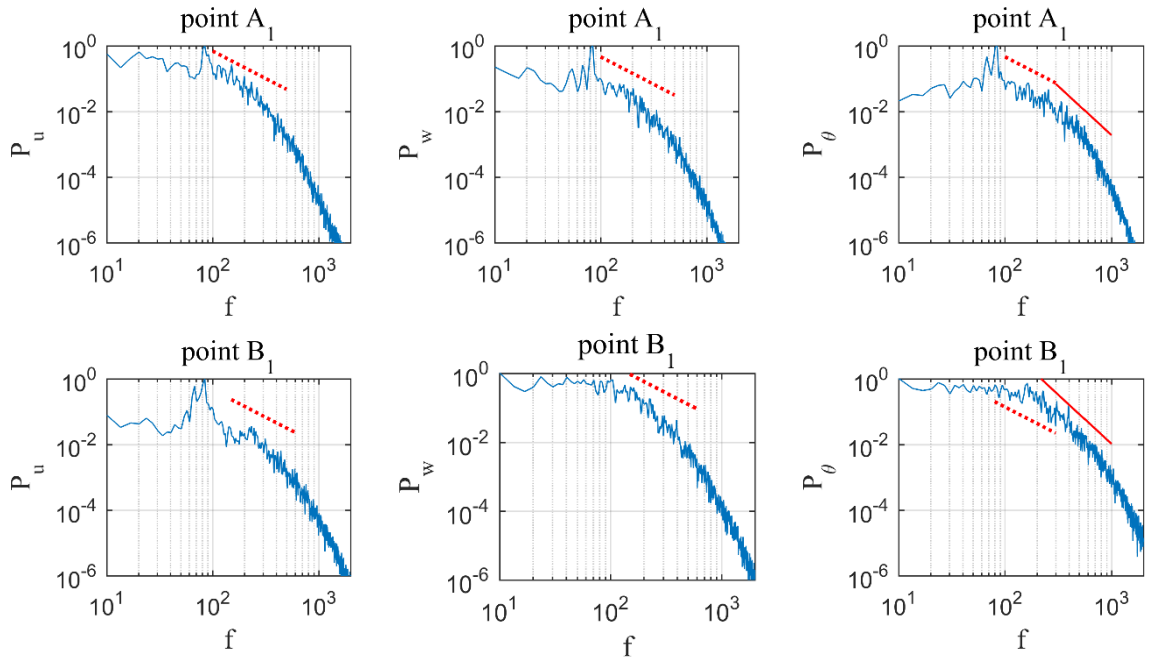

Figure 3.15. $\mathrm{Ra} = 1.2\times10^{7}$. Density power spectra of velocity components u, w and temperature θ at the monitoring points. Dotted trendline: -5/3 power law, solid trendline: -3 power law.

Snapshots of the instantaneous thermal fields at $\mathrm{Ra} = 1.2\times10^{7}$ in the planes $y = 0.25$, 0.5 and 0.75 are displayed in Figure 3.16. They show that, even if the primary laminar structure remains above the source, the temperature field is disturbed in the rest of the cavity as the result of the developing instabilities. Moreover, the antisymmetric mode along the *y*-direction is destroyed at this Ra number.

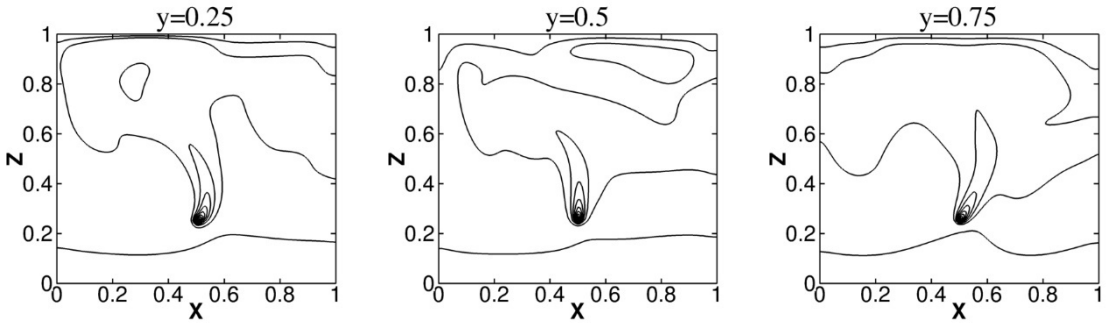

Figure 3.16. $\mathrm{Ra} = 1.2\times10^{7}$. Snapshots of the instantaneous temperature fields at three depths $y = [0.25;\ 0.5;\ 0.75]$. Contour levels (0.02:0.02:0.4).

3.4 Turbulent regime

3.4.1 Time and grid space convergence

To investigate the turbulent behavior of plumes, simulations were carried out at $\mathrm{Ra} = 10^9$ by increasing progressively the Rayleigh number from previous results. Figure 3.17 shows the time evolution of the total Nusselt number Nu_{total}^{2D}. After a transient period up to $t \approx 0.07$ the flow is statically established, and statistics are performed up to $t \approx 0.16$ (approximately 2 hours in real time for the statistics accumulation).

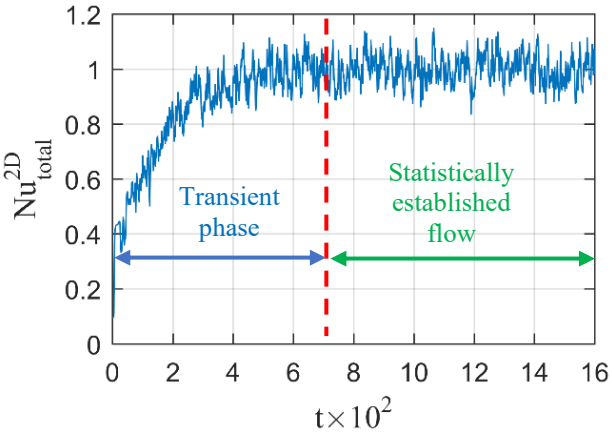

Figure 3.17. $\mathrm{Ra} = 10^9$. Time evolution of the total Nusselt number.

The simulation was launched on the Ada supercomputer of Idris Center using 64 processors of a 2.67 GHz IBM x3750M4. The total CPU consumption was about 8 000 h for a total dimentionless time $t \approx 0.16$.

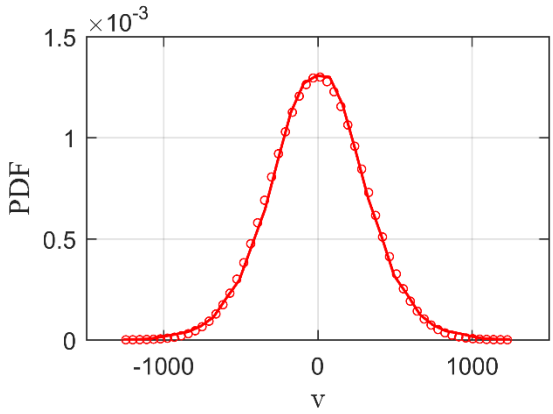

Figure 3.18. $\mathrm{Ra} = 10^9$. Normalized distribution of the density probability function of the axial velocity v at point B_2. Solid line: present results. Circular marker: Gaussian distribution with the same mean and standard deviation values.

Figure 3.18 presents the probability distribution functions (PDF) of the axial velocity v at the monitoring point B_2 (cf. Figure 3.1) over the statistical time interval $t \in [0.06,\ 0.14]$. It is observed that the mean value of PDF distribution is located around $v = 0$, from which it can be deduced that the symmetry of fluid motion along the source direction is well established in the mid-plane $y = 0.5$. In addition, the PDF profile follows a Gaussian distribution, which is also observed in the works of Bastiaans et al. (2000).

To ensure sufficient grid resolution, a comparison between the grid size $\delta r = (\delta x \delta y \delta z)^{1/3}$ and the Kolmogorov scale η_k is done over the global domain. It is found that the maximum of the ratio $\delta r / \pi\eta_k$ in the global domain equals 0.641, which well satisfies the Grötzbach requirement (cf. section 1.2.5). Figure 3.19 displays the distribution of this ratio in the mid-plane $y = 0.5$. The Grötzbach requirement is always well respected, and the need for the finer grid resolution is encountered close to the top wall, that is in the impinging regions of the plume.

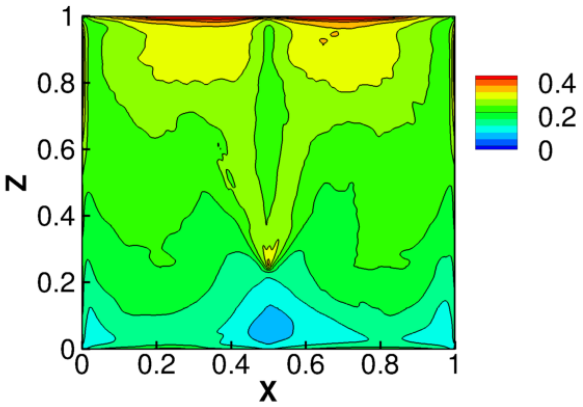

Figure 3.19. $\mathrm{Ra} = 10^9$. Ratio of the grid size compared to the Kolmogorov scale in the mid-plane $y = 0.5$.

3.4.2 Instantaneous fields

Snapshots of the temperature in the planes $y = 0.5$ and $x = 0.5$ are displayed in Figure 3.20. It is shown that in the mid-plane $y = 0.5$, the laminar structure is still present above the source while small structures are created at larger heights where the plume becomes turbulent. Below the source, the thermocline is maintained but is affected by the returning eddies from the upper part. Along the *y*-direction, it can be seen that the turbulence structures also mainly exist in the high part of the cavity.

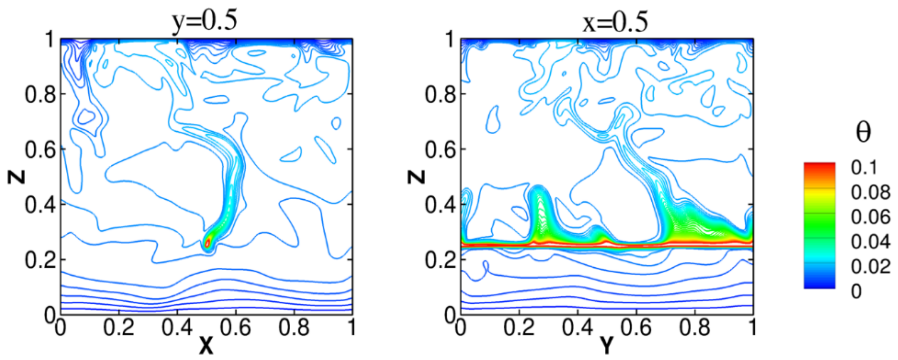

Figure 3.20. $\mathrm{Ra} = 10^9$. Instantaneous fields of temperature θ in the planes $y = 0.5$ and $x = 0.5$.

For turbulent flows, the identification of the vortex structures allows to better understand the flow dynamics. The most widely used local methods for vortex identification are based on the analysis of the velocity-gradient tensor $\nabla \boldsymbol{u} = \boldsymbol{\Omega} + \mathbf{S}$, its symmetric and antisymmetric parts are strain-rate tensor $\boldsymbol{S}$ and vorticity tensor $\boldsymbol{\Omega}$, respectively, and can be written as follows

$$\frac{\partial u_i}{\partial x_j} = S_{ij} + \Omega_{ij} = \frac{1}{2}\left(\frac{\partial u_i}{\partial x_j} + \frac{\partial u_j}{\partial x_i}\right) + \frac{1}{2}\left(\frac{\partial u_i}{\partial x_j} - \frac{\partial u_j}{\partial x_i}\right) \tag{3.2}$$

We use here the Q criterion (Hunt et al., 1988) defined by

$$\mathrm{Q} = -\frac{1}{2}\frac{\partial u_i}{\partial x_j}\frac{\partial u_j}{\partial x_i} = \frac{1}{2}\left(\|\boldsymbol{\Omega}\|^2 - \|\mathbf{S}\|^2\right) \tag{3.3}$$

where $\| \ \|$ is the tensor norm, which expresses for any tensor $\mathbf{G}$, as $\|\mathbf{G}\| = [\mathrm{tr}(\mathbf{G}\mathbf{G}^T)]^{1/2}$.

This criterion, introduced by Hunt et al. (1988), is based on the second invariant of $\nabla \boldsymbol{u}$ for incompressible flows, and represents the local balance between shear strain rate and vorticity magnitude. Numerous analyses done on various flows (isotropic turbulence, free-shear layers, separated flows, wall flows, etc.) show that the coherent vortices are well characterized by the positive iso-surfaces of Q.

Figure 3.21 presents the distribution of Q criterion at the same instant as the snapshots of Figure 3.20. It can be seen that the vortices are created along the linear heat source, and develop and enlarge in an ascendant motion up to $z = 0.6$. This development of unsteady large structures mainly characterizes the laminar region close to the heat source, as observed in Figure 3.20. Further downstream, the vortices rapidly roll-up, stretch and break down to turbulence. In the downstream after the collision on the top wall, some vortices are also produced within the descending motion of plume.

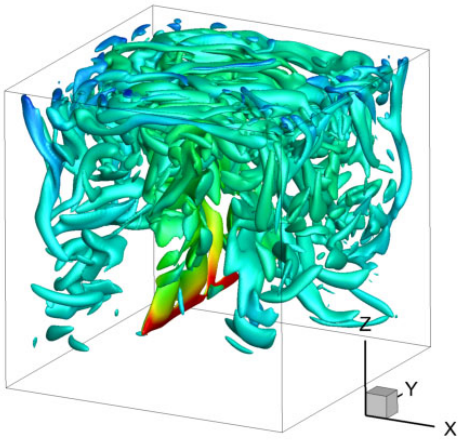

Figure 3.21. $\mathrm{Ra} = 10^9$. Iso-surface of instantaneous Q criterion colored by temperature ($\mathrm{Q} = 10^8$).

3.4.3 Time-averaged fields

The distributions of time-averaged temperature $\overline{\theta}$, 2D kinetic energy $\overline{E}_k$ and streamlines are displayed in Figure 3.22. The mean flow moves upward from the heat source, then descends along the lateral walls, and finally feed the plume entertainment region close to the source, which forms two recirculating regions in the cavity. Below the source, there exists always a region of quasi-horizontal thermoclines.

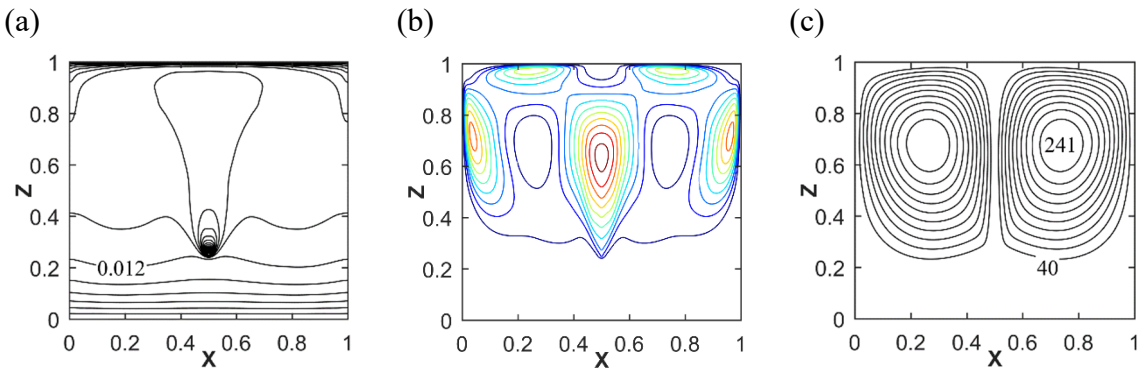

Figure 3.22. $\mathrm{Ra} = 10^9$. Time averaged distributions of (a) temperature $\overline{\theta}$, (b) 2D kinetic energy $\overline{E}_k$, and (c) stream function $\overline{\psi}$ in the mid-plane $y = 0.5$. Contour levels $\overline{\theta} = [0.002 : 0.002 : 0.1]$, $\overline{E}_k = [5\times10^4 : 5\times10^4 : 5\times10^5]$ and $\overline{\psi} = [40 : 20 : 220]$.

To visualize the spatial distribution of plume, the mean fields of kinetic energy in different planes are shown in Figure 3.23. It is observed that the mean flow structure is nearly uniform along the linear heat source direction in the central part of the cavity, and that 3D effects are only present near the front and rear walls. The distributions of the mean kinetic energy in the three *y*-planes also indicates that the flow structures are approximately maintained along *y*-direction.

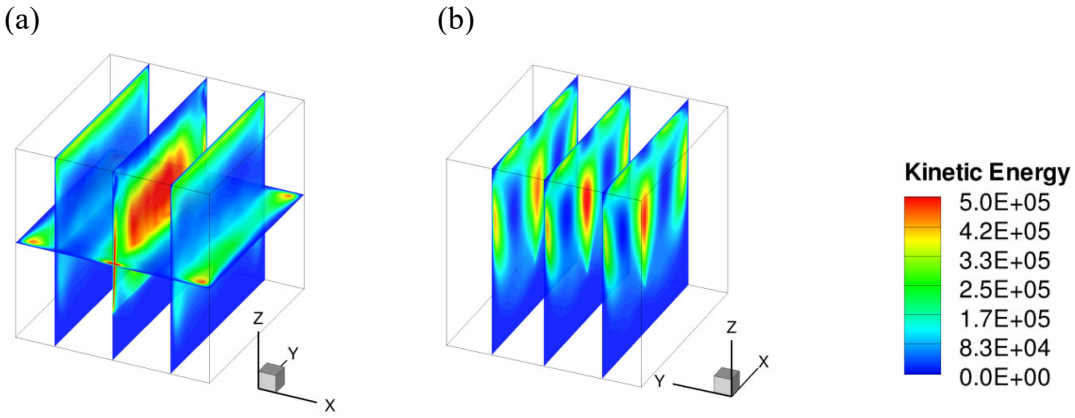

Figure 3.23. $\mathrm{Ra} = 10^9$. Spatial distribution of time-averaged kinetic energy in the planes (a) $x = [0.2;\ 0.5;\ 0.8]$ and $z = 0.5$, and (b) $y = [0.2;\ 0.5;\ 0.8]$.

3.4.4 Second order moments and time spectra

The distribution of temperature fluctuations at mid-depth $y = 0.5$ is shown in Figure 3.24. We observe that the temperature fluctuations are more concentrated around the line source due to its high temperature level generated. Figure 3.25 displays the distribution of velocity fluctuations $(u_i)_{rms}$ and the turbulent kinetic energy $k = (u_{rms}^2 + v_{rms}^2 + w_{rms}^2)/2$ in the mid-plane $y = 0.5$. As described for the instantaneous fields, the velocity fluctuations and the turbulent kinetic energy are found more important in the upper part of cavity. The profiles of $(u_i)_{rms}$ and θ_{rms} along the centerline $x = y = 0.5$ are plotted in Figure 3.26. It is observed that the velocity fluctuations reach the maximum levels near the top wall, especially for u_{rms} and v_{rms} which presents a sharp increase in the top layer. The fluctuations u_{rms} also presents a local maximum at the heat source position due to the entrainment in the near-source region of plume. As for θ_{rms}, the absolute maximum is located at the source position, and a local maximum is present very near the top with the impingement of the plume.

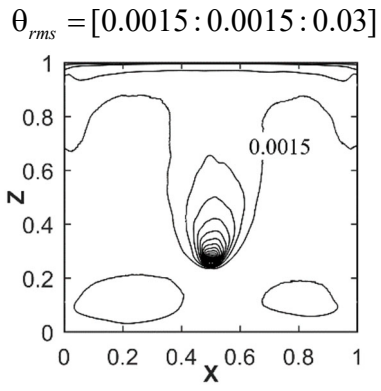

Figure 3.24. $\mathrm{Ra} = 10^9$. Isocontours of the temperature fluctation θ_{rms} in the mid-plane $y = 0.5$.

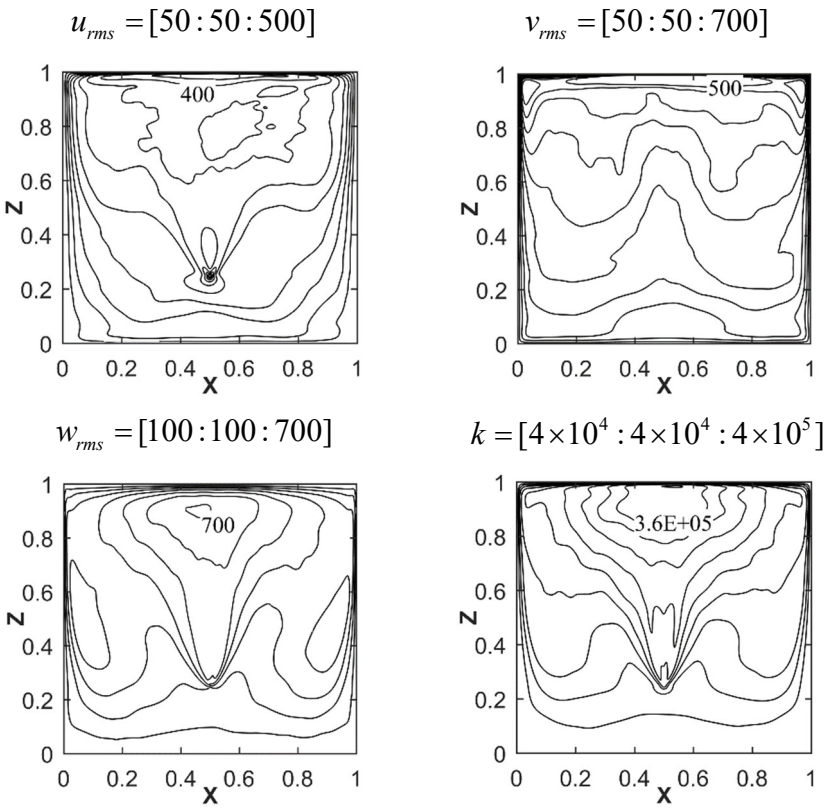

Figure 3.25. $\mathrm{Ra}=10^9$. Isocontours of the velocity fluctations $(u_i)_{rms}$, turbulence kinetic energy k in the mid-plane $y=0.5$.

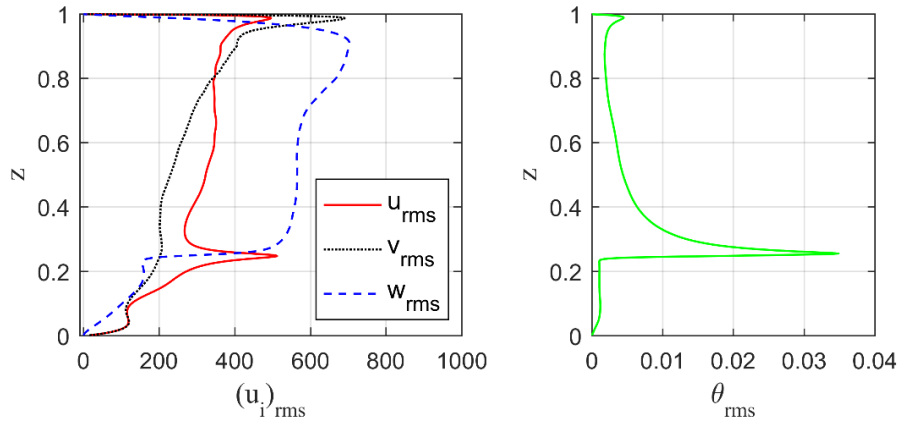

Figure 3.26. $\mathrm{Ra}=10^9$. Vertical profiles of the velocities and temperature fluctuations along the centerline $x=y=0.5$.

The u, w and θ power spectra at the monitoring points A_2 and B_2 in the mid-plane $y=0.5$ are plotted in Figure 3.27. A_2 is placed outside the plume zone while B_2 is inside the plume plane, but far above the heat source (cf. Figure 3.1). The -5/3 Kolmogorov power law is suspected in all the spectra, indicateing that a fully developed turbulent flow is achieved in the plume plane as well as in the far-field of the plume. For the temperature spectra at the two monitoring points, a quite rapidly decay following -3 power law is observed at the highest

frequencies. This is a typical feature of turbulent buoyancy induced flows (Kotsovinos, 1991), and was previously observed at $\mathrm{Ra} = 1.2 \times 10^7$ (section 3.3.3). Besides, we notice that at point B_2, the frequency domains of the spectra are slightly broader than at point A_2, revealing a higher turbulence level in the plume plane. These spectra also confirm that the resolution is fine enough to capture the smallest scales.

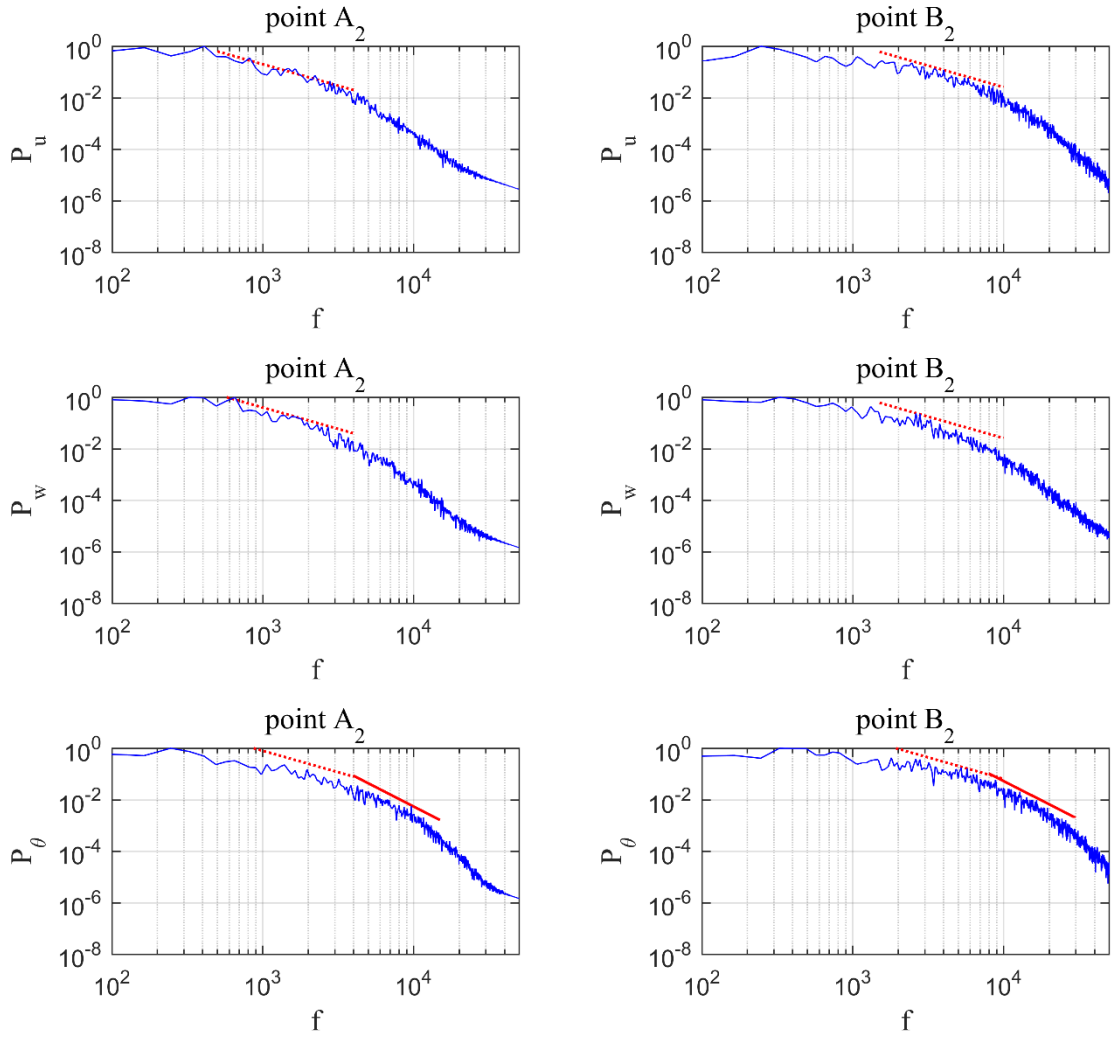

Figure 3.27. $\mathrm{Ra} = 10^9$. Density power spectra of u, w, and θ at the points A_2 and point B_2 in the mid-plane $y = 0.5$. Dotted trendline: -5/3 power law, solid trendline: -3 power.

3.5 Conclusion

The evolution of a 3D plume in pure convective case (i.e. neither gas nor wall radiation) has been investigated throughout the transition from steady-state to turbulent behavior. The thermal and kinetic properties of plumes were studied at different flow regimes. We found that the transition to unsteadiness occurs through a supercritical Hopf bifurcation. In the succeeding time periodic regimes, the flow structure combines an antisymmetric oscillating mode along the heat source direction and a swaying motion of the plume in each transverse

plane with respect to the vertical centerline. The turbulent flow was finally analysed, which destroys the antisymmetric mode and presents turbulence structures mainly in the upper part of the cavity. To emphasize the influence of gas radiation on the flow behavior and thermal transfers, different gaseous media will be introduced in the following chapter.

Chapter 4
Convection-radiation coupling

Convection-radiation coupling is finally studied by introducing gray gas at various optical thicknesses (τ) or real gaseous mixture of dry air and water vapor with a fixed molar fraction (X_a) of H_2O over the whole domain. Simulations are performed at various Rayleigh numbers from 10^6 to 10^9 to examine the influence of gas radiation at different flow regimes.

4.1 Simulations characteristics

In this chapter, the effects of governing parameters (Ra , τ , X_a , T_{ref}) are discussed. The results of coupled transfers are compared with those obtained in the pure convective configuration, where the fluid is assumed to be transparent and the walls purely reflective. Table 4.1 specifies the different Rayleigh numbers considered and the flow regimes observed. Note that the mesh distribution and the time step used in the coupled simulations are based on the pure convective simulations at the same Rayleigh number.

Regime	Rayleigh	Gas media	
Steady	10^6	Gray gas	$\tau = [0.1;\ 0.2;\ 0.5;\ 1;\ 2;\ 5]$
	2×10^6	Gray gas	$\tau = [0.1;\ 0.2;\ 0.5]$
		Real gas	$X_a = 2\%$ at $T_{ref} = 300$ K
		Real gas	$X_a = [2\%;\ 10\%;\ 20\%]$ at $T_{ref} = 500$ K
	5×10^6	Gray gas	$\tau = [0.1;\ 0.2;\ 0.5]$
	1.2×10^7	Gray gas	$\tau = 0.5$
Transitional	1.2×10^7	Gray gas	$\tau = [0.1;\ 0.2]$
		Real gas	$X_a = 2\%$ at $T_{ref} = 300$ K
Turbulent	10^9	Gray gas	$\tau = 0.1$
		Real gas	$X_a = 2\%$ at $T_{ref} = 300$ K

Table 4.1. Considered configurations in the case of convection-radiation coupling at different Rayleigh numbers and corresponding flow regimes.

4.2 Steady regime

4.2.1 Gray gas: effects of the optical thickness

To study the influence of gas radiation, we applied the assumption of gray gas in this section. The simulations were performed at $\mathrm{Ra} = 10^6$ with various optical thicknesses τ. Two additional parameters are fixed: the Planck number at $\mathrm{Pl} = 5.61 \times 10^{-7}$ and the temperature ratio at $\Theta_0 = 30473.1$. Note that the simulation using gray gas approximation has no dependency on the reference temperature T_{ref}.

Table 4.2 specifies the different considered configurations. Case (A) corresponds to a pure convection configuration, i.e. $\varphi_r''' = 0$ in the medium and $q_r^{net} = 0$ at the walls. This case has been documented in the previous section 3.2 and will serve as a reference to assess the radiation effects.

Configuration	(A)	(B)	(C)	(D)
Gas medium	Transparent	Gray gas	Gray gas	Gray gas
Optical thickness	$\tau = 0$	$\tau = 0.1$	$\tau = 0.2$	$\tau = 0.5$
Isotherm walls	$\varepsilon = 0$	$\varepsilon = 1$	$\varepsilon = 1$	$\varepsilon = 1$
Adiabatic walls	$\varepsilon = 0$	$\varepsilon = 0$	$\varepsilon = 0$	$\varepsilon = 0$

Table 4.2. $\mathrm{Ra} = 10^6$. Different considered configurations.

The results obtained for each configuration at $\mathrm{Ra} = 10^6$ reveal a steady-state regime. Figure 4.1 displays the steady distributions of temperature θ, stream function and 2D kinetic energy E_k at mid-depth $y = 0.5$ for the different cases. When gas radiation is considered, a decrease of the spatial spreading of the thermal field is observed. As τ increases, the temperature field is gradually homogenized in the regions next to and above the source, as radiation becomes the dominant heat transfer mode in the cavity. Moreover, the temperature distribution in the far-field of the plume is also changed: the fluid out of the plume is quasi-isothermal for the gray gases in contrast of the case (A), where a stratification is established in the cavity. It should be noticed that at $\tau = 0.5$, all the isotherms tend to be concentrated around the heat source.

Regarding the kinetic fields, when τ increases, the maximum of the stream function and the density of streamlines gradually decrease, but the global flow circulation still fills the domain above the source. Meanwhile, a reduction of the kinetic energy is clearly visible in Figure 4.1. Therefore, gas radiation tends to decrease the flow intensity and to weaken the global circulation.

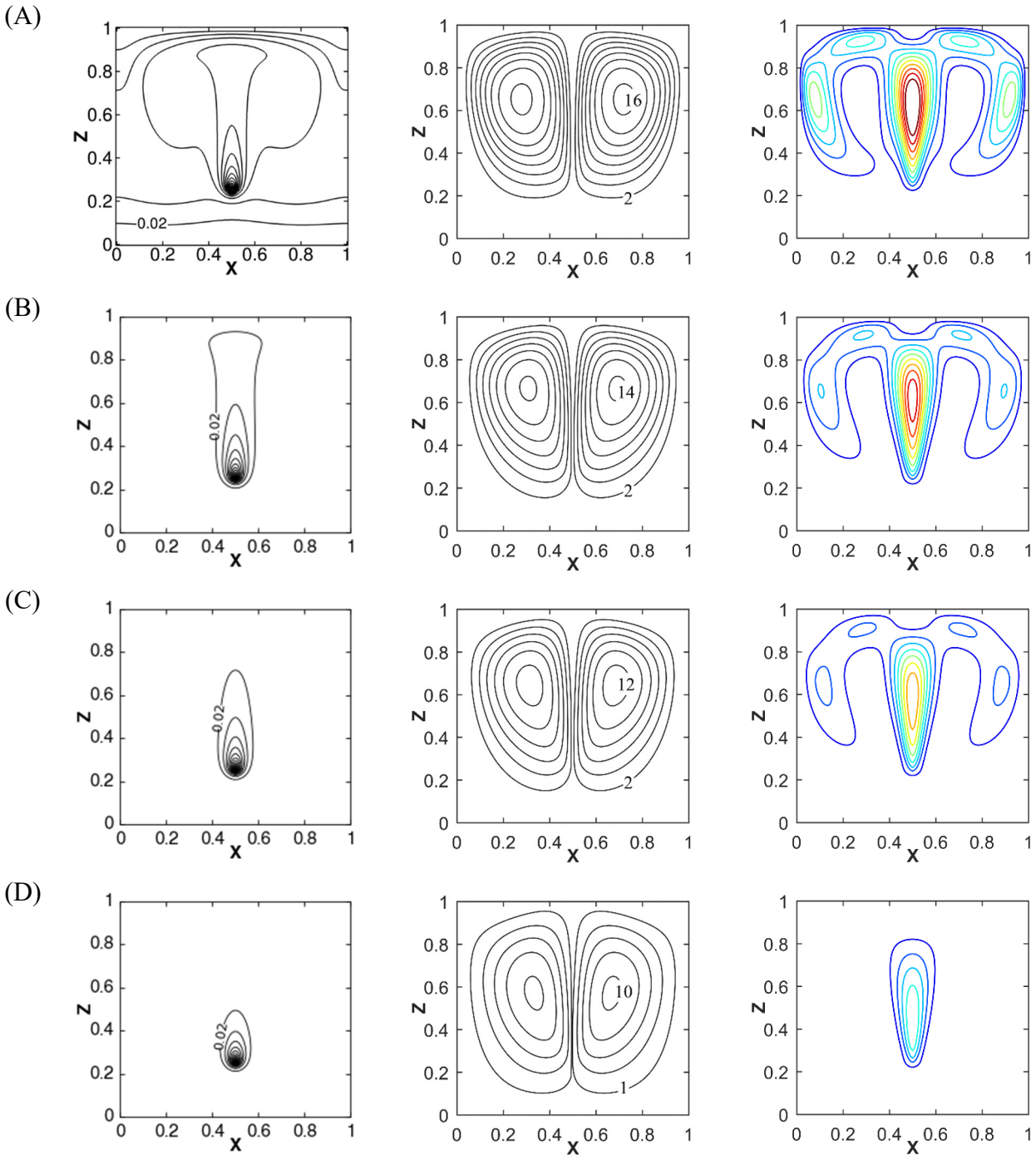

Figure 4.1. $\mathrm{Ra} = 10^6$. Iso-contours of temperature, stream function and kinetic energy in the mid-plane $y = 0.5$ for the different configurations. Contour levels of temperature $[0.02 : 0.02 : 0.4]$. Contour levels of kinetic energy [1000:1000:10000].

Figure 4.2 presents the distributions of radiative power ($-\varphi_r''' \times 10^6$) at mid-depth $y = 0.5$ for the different gray media. When the fluid is emitting heat, the radiative source term is negative ($-\varphi_r''' > 0$), while a positive value indicates regions of radiative absorption ($-\varphi_r''' < 0$). It can be seen from Figure 4.2 that the fluid in the inner part of the cavity mainly emits heat and in particular the whole plume zone. Conversely, fluid areas close to the walls absorb heat

by radiation, and the increase of τ induces a spatial extension of the absorption zones in the cavity. In addition, it is clearly visible that the radiative power is more important above the source due to the high temperature level it generates.

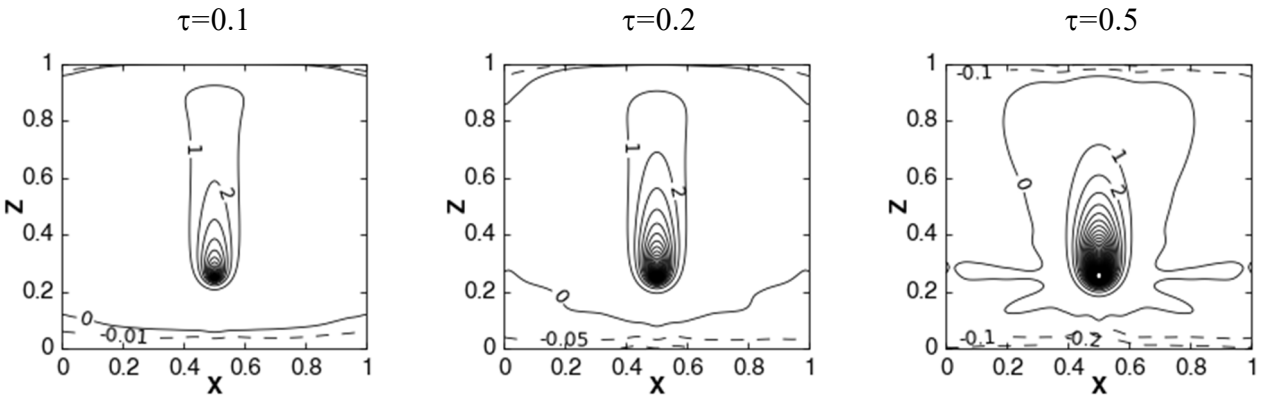

Figure 4.2. $\mathrm{Ra}=10^6$. Distribution of radiative power $(-\varphi_r'''\times 10^6)$ in the mid-plane $y=0.5$ at different optical thicknesses.

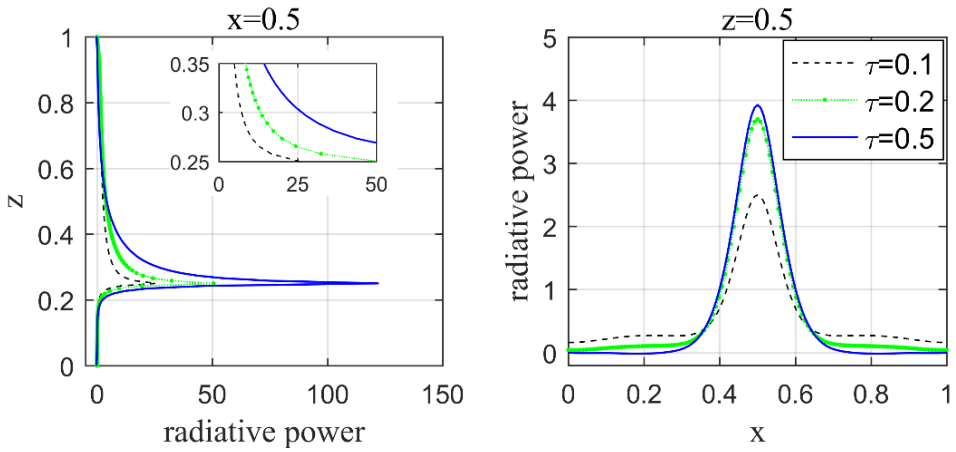

Figure 4.3. $\mathrm{Ra}=10^6$. Profiles of radiative power $(-\varphi_r'''\times 10^6)$ in the mid-plane $y=0.5$ along the lines $x=0.5$ (left) and $z=0.5$ (right) at different optical thicknesses.

The profiles of radiative power $(-\varphi_r'''\times 10^6)$ along the centerline $x=y=0.5$ are plotted in Figure 4.3 for the different gray media. As expected, the emitting radiative power reaches its higher values at and just above the heat source with very sharp gradients. The optically thicker the medium, the higher the emitting radiative power in the conduit of the plume (especially above the heat source) and the lower in the far field of the plume. It is also noticed that the radiative exchanges in the absorption region are very low when compared to the emission ones.

The vertical profiles of θ and w along the vertical centerline $x=0.5$ are shown in Figure 4.4. Because of the absorption/re-emission mechanisms in the medium, a rapid drop of the temperature is produced below and above the line heat source, comparatively to case (A). It

also results in a decrease of the temperature values and of the temperature gradients over the cavity, leading to a weakening of the thermal plume and to a reduction of its spatial spreading, as previously observed in Figure 4.1. Besides, increasing the optical thickness leads to a gradual disappearance of the thermal jet impingement on the ceiling (see Figure 4.1 and Figure 4.4 (a)). The weakening of thermal plume by radiation also causes a weakening of the fluid motion. As shown in Figure 4.4 (b), by increasing the optical thickness, the vertical velocity decreases monotonically along the plume axis.

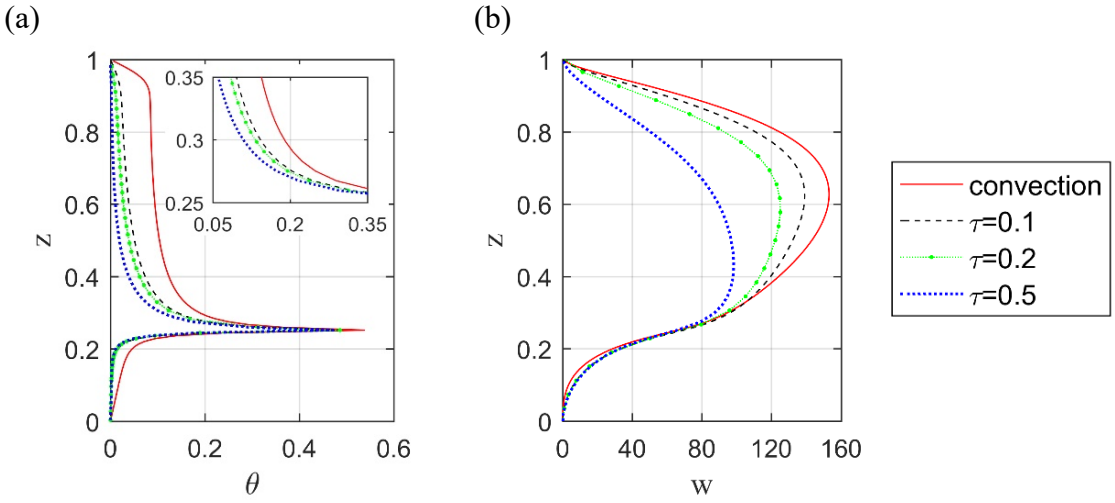

Figure 4.4. $\mathrm{Ra} = 10^6$. Vertical profiles of (a) temperature θ and (b) vertical velocity w along the line $x = y = 0.5$.

The horizontal profiles of θ and w are plotted in Figure 4.5 for the different configurations. At the different heights, there is a significant downward shift of temperature values when gas radiation is accounted for. Concerning the vertical velocity, the profiles are quite similar in all the cases at $z = 0.3$, where the fluid motion has just been initiated. For $z = 0.5$ and $z = 0.7$, a decrease of the vertical velocity maxima is observed with the growth of τ, indicating again that gas radiation reduces the strength of the plume.

In order to compare the plume structure, the profiles of the reduced temperature $\theta - \theta_{av}$, where θ_{av} is the x-averaged temperature along the cavity width, are plotted in Figure 4.6 at mid-height $z = 0.5$ of the mid plane $y = 0.5$. The maximum value of $\theta - \theta_{av}$ gradually decreases when τ increases in the middle part of plume ($0.4 \le x \le 0.6$), showing again the homogenization effect of gas radiation on temperature field.

In addition, it is found that the middle part of these profiles respects a Gaussian distribution. The full widths W_g of the Gaussian distribution at the mid maximum value ($W_g \approx 2.355\sigma$, σ being the standard deviation) are calculated for the different cases and increase with the

optical thickness of the gas: W = (A) 0.1107, (B) 0.1154, (C) 0.1201, (D) 0.1225, respectively.

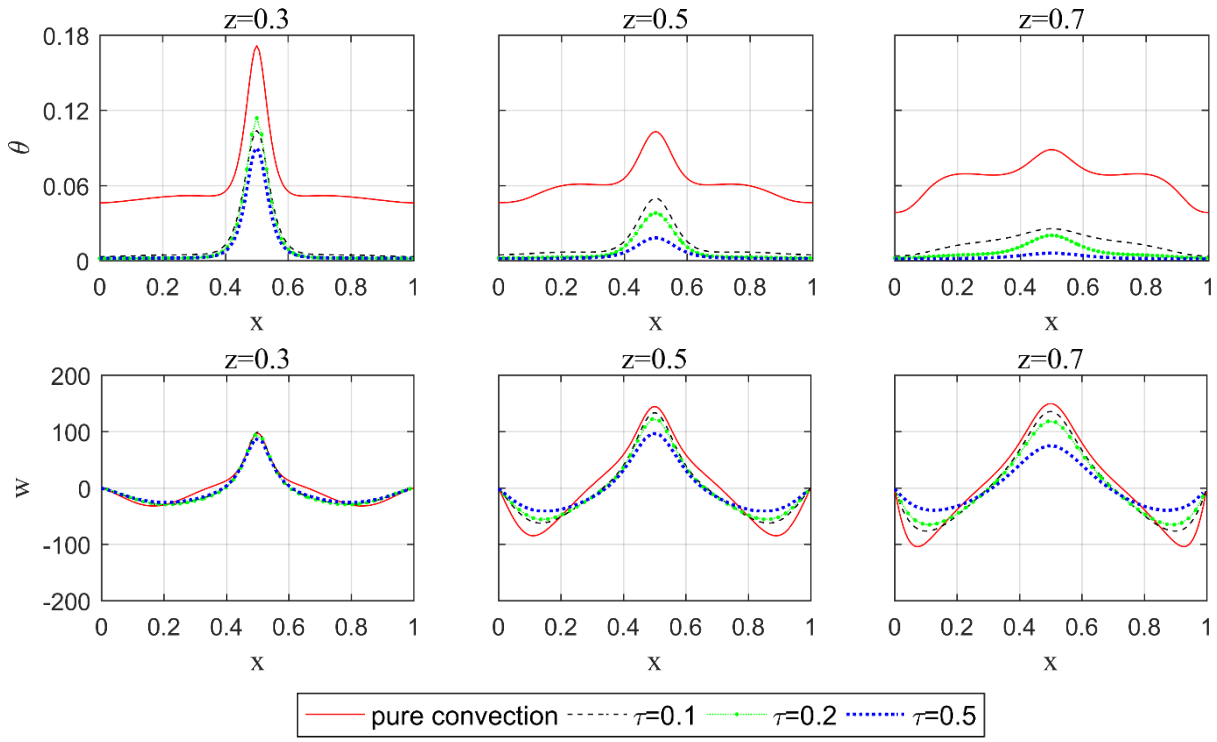

Figure 4.5. $\mathrm{Ra} = 10^6$. Horizontal profiles of temperature θ and vertical velocity w at various heights.

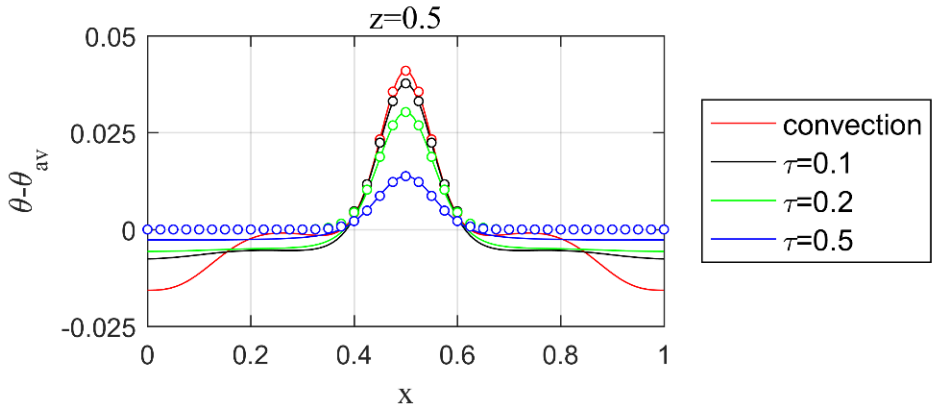

Figure 4.6. $\mathrm{Ra} = 10^6$. Profiles of the reduced temperature $\theta - \theta_{av}$ at the line $y = z = 0.5$. Circular marker: Gaussian distribution approximating the different profiles.

Table 4.4 compare the maximum values of temperature and velocity components in the mid-depth plane, as well as the convective and radiative Nusselt numbers on the isothermal walls. The axial velocity v is of order 10^{-8} for the different cases due to symmetry at the mid-depth. The maximum values of θ, u and w decrease when gas radiation is taken into account. Gas radiation also redistributes the energy transfer between radiative and convective parts along the isothermal walls: the convective flux at the top wall decreases rapidly as τ

increases due to the homogenization effect of radiation on the temperature field, and radiation gradually becomes the dominant mode of heat transfer.

Case	τ	θ_{max}	u_{max}	v_{max}	w_{max}	$Nu^{2D}_{c,\ bottom}$	$Nu^{2D}_{c,\ top}$	$Nu^{2D}_{r,\ bottom}$	$Nu^{2D}_{r,\ top}$
(A)	0	0.539	94.5	5.1×10^{-8}	153.9	0.192	0.807	0	0
(B)	0.1	0.489	79.5	9.6×10^{-8}	139.8	0.013	0.164	0.379	0.443
(C)	0.2	0.486	66.4	6.8×10^{-8}	125.9	0.016	0.069	0.447	0.467
(D)	0.5	0.471	37.2	3.6×10^{-8}	99.2	0.026	0.022	0.537	0.414

Table 4.3. $Ra = 10^6$. Comparative results between the different configurations. The maximum values are evaluated in the mid plane $y = 0.5$.

To study the evolution of the Nusselt numbers with the optical thickness, further simulations were performed at $Ra = 10^6$ for τ varying up to 3, as shown in Figure 4.7. It is observed that the convective fluxes at the top and the bottom walls drop down rapidly when radiation is considered. From $\tau = 0$ to 0.2, the radiative fluxes Nu_r increase on the top and bottom walls. Thereafter, the radiative flux at the top wall decreases with the optical thickness and becomes lower than that on the bottom wall. The reason is that the optical path (l) from the heat source is lower for the bottom wall than for the top wall, which results in a higher attenuation by absorption ($\exp(-\kappa l)$) in the region below the heat source. This phenomenon is enhanced for an optically thicker medium, which produces a greater radiative flux at the bottom wall.

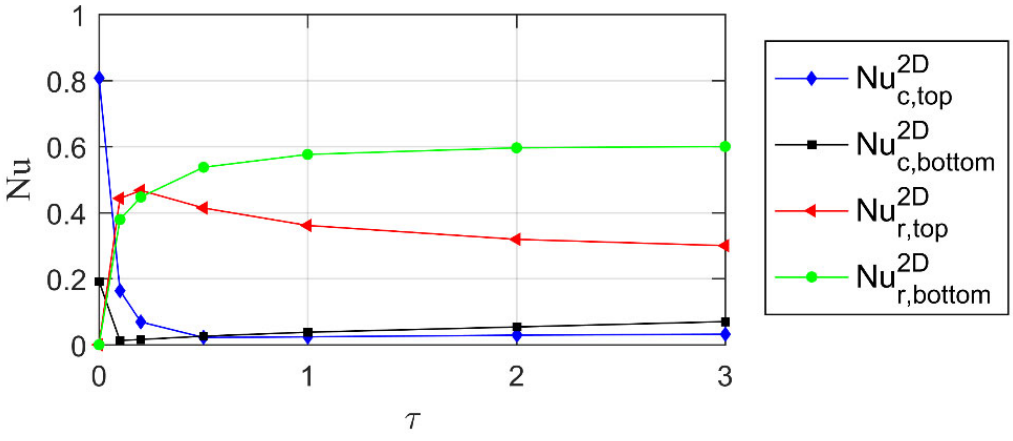

Figure 4.7. $Ra = 10^6$. Convective and radiative Nusselt numbers at different optical thicknesses.

Simulations have also been performed at higher Rayleigh numbers $Ra = 2\times10^6$ and 5×10^6. At these two Rayleigh numbers, a steady state regime is still observed for $\tau = 0.1$, 0.2 and 0.5, while an oscillating regime is present for a pure convective flow (cf. section

3.3.3). Table 4.4 gives a comparison in terms of maximum temperature, maximum velocities, convective and radiative heat transfer on the top and bottom walls at $\mathrm{Ra}=10^6$, 2×10^6 and 5×10^6 for all the gas media we considered (the results for the pure convective case are the time averaged results).

Case	(A)			(B)			(C)			(D)		
τ	0			0.1			0.2			0.5		
$\mathrm{Ra}/10^6$	1	2	5	1	2	5	1	2	5	1	2	5
$\theta_{\max}$	0.539	0.493	0.434	0.489	0.457	0.411	0.486	0.452	0.408	0.471	0.441	0.402
$u_{\max}$	94.5	125.2	191.4	79.5	122.4	202.1	66.4	108.9	188.7	37.2	73.3	150.7
$w_{\max}$	153.9	201.8	289.8	139.8	194.1	289.7	125.9	179.3	278.3	99.2	144.0	241.5
$\mathrm{Nu}^{2D}_{c,\,\mathrm{bottom}}$	0.192	0.185	0.151	0.013	0.014	0.014	0.016	0.014	0.013	0.026	0.025	0.022
$\mathrm{Nu}^{2D}_{c,\,\mathrm{top}}$	0.807	0.813	0.847	0.164	0.215	0.280	0.069	0.111	0.171	0.022	0.031	0.061
$\mathrm{Nu}^{2D}_{\mathrm{r},\,\mathrm{bottom}}$	0	0	0	0.379	0.346	0.312	0.447	0.407	0.363	0.537	0.503	0.450
$\mathrm{Nu}^{2D}_{\mathrm{r},\,\mathrm{top}}$	0	0	0	0.443	0.424	0.393	0.467	0.467	0.452	0.414	0.440	0.466

Table 4.4. Comparative results between the different gas media at three Rayleigh numbers. The maximum values are evaluated in the mid plane $y=0.5$.

The radiation effects and the main trends observed when varying the optical thickness, discussed in detail for $\mathrm{Ra}=10^6$, are also valid for the other two Rayleigh numbers:

(i) The global circulation and the maximum temperature decrease as τ increases;

(ii) Gas radiation stabilizes the plume flow, and then delays the transition to unsteadiness;

(iii) Gas radiation influences the heat transfer distribution at the isothermal walls, and the radiative fluxes become the dominant mode of heat exchanges at these walls;

(iv) The increase of the Rayleigh number strengthens the global circulation and the convective heat transfer at the top wall, as expected.

4.2.2 Real gas model

In this section, the real gas model is introduced by considering a gaseous mixture of dry air and water vapor at $\mathrm{Ra}=2\times10^6$. Two additional parameters are fixed: the Planck number at $\mathrm{Pl}=1.12\times10^{-6}$ and the temperature ratio at $\Theta_0=15236.5$. The molar fraction of water vapor is fixed at $X_a=2\%$ over the whole domain, and the reference temperature is

$T_{ref} = 300$ K. To examine the radiation behavior in real gas, solutions are compared to the configurations of pure convection and various gray gases.

The different considered configurations with the corresponding observed flow regimes are reported in Table 4.5. It is shown that, whatever gray media or real gaseous mixture, the transition to unsteadiness is delayed by gas radiation.

Configuration	(A)	(B)	(C)	(D)	(E)
Gas medium	Transparent $\tau = 0$	Gray gas $\tau = 0.1$	Gray gas $\tau = 0.2$	Gray gas $\tau = 0.5$	Real gas
Isotherm walls	$\varepsilon = 0$	$\varepsilon = 1$	$\varepsilon = 1$	$\varepsilon = 1$	$\varepsilon = 1$
Adiabatic walls	$\varepsilon = 0$	$\varepsilon = 0$	$\varepsilon = 0$	$\varepsilon = 0$	$\varepsilon = 0$
Regime	Unsteady	Steady	Steady	Steady	Steady

Table 4.5. $\mathrm{Ra} = 2\times10^6$. Different considered configurations and corresponding flow regimes.

Figure 4.8 displays the steady-state distributions of temperature, stream function, and 2D energy in the mid-plane $y = 0.5$ for the different participating media, and compared to the time-averaged results of the pure convective flow (case A). The presence of gas radiation leads to a decrease in the spatial spreading of the plume, as well as a weakening of the global flow, whatever gray media or real gas mixture. As described in section 4.2.1, this weakening effect is enhanced with the increase of the optical thickness for gray gases. The corresponding profiles of temperature θ and vertical velocity w along the centerline $x = 0.5$ are plotted in Figure 4.9. It is shown that the case (E) using a real gas model is more similar with the case (B), for the particular conditions considered here (given H, T_{ref}, X_a, etc.).

The distributions of the radiative power at mid-depth $y = 0.5$ are presented in Figure 4.10, and the corresponding profiles along the lines $x = 0.5$ and $z = 0.5$ are plotted in Figure 4.11. In gray media (case B to D), we observe again that the most part of the fluid emits heat, and the radiative emissions are stronger than those obtained at $\mathrm{Ra} = 10^6$ (cf. Figure 4.2). It is also seen that radiative exchanges in the absorption areas ($-\varphi_r''' < 0$) are almost negligible compared to emission areas, except for the real gas (case E), which shows as well, higher absorption levels than in the gray media. In the particular conditions considered for the real gas mixture, the emission regions observed for the real gas are close to the optically thin gray gas $\tau = 0.2$. However, the absorption dominant area observed for the real gas corresponds to the horizontal layer of cold fluid settled at the bottom part of the cavity, but also to a specific area surrounding the heat source and the base of the plume conduit.

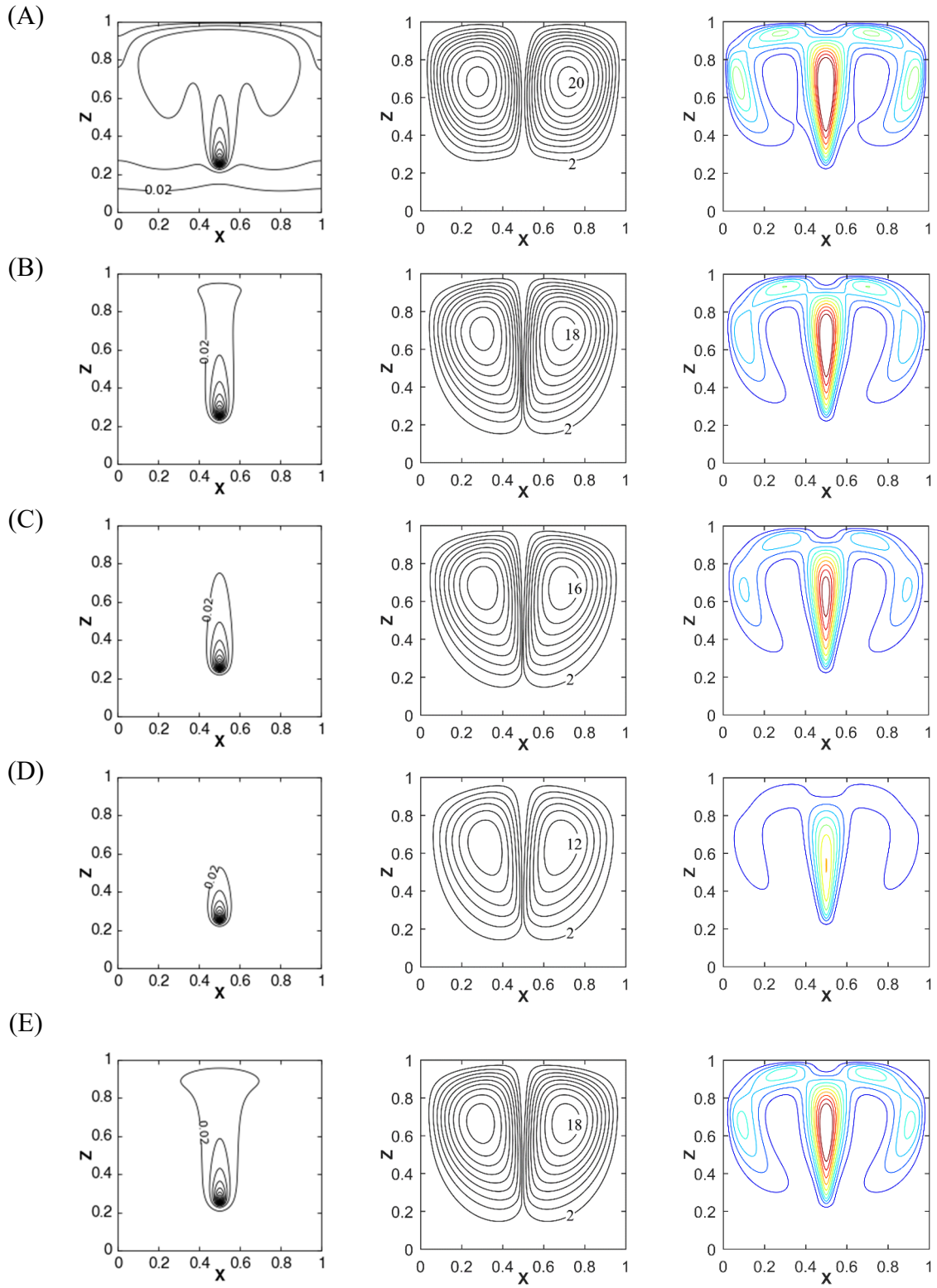

Figure 4.8. $\mathrm{Ra} = 2\times10^{6}$. Iso-contours of temperature, stream function and kinetic energy in the mid-plane $y = 0.5$ for the different configurations. Contour levels of temperature [0.02, 0.02, 0.4]. Contour levels of kinetic energy [1500:1500:15000].

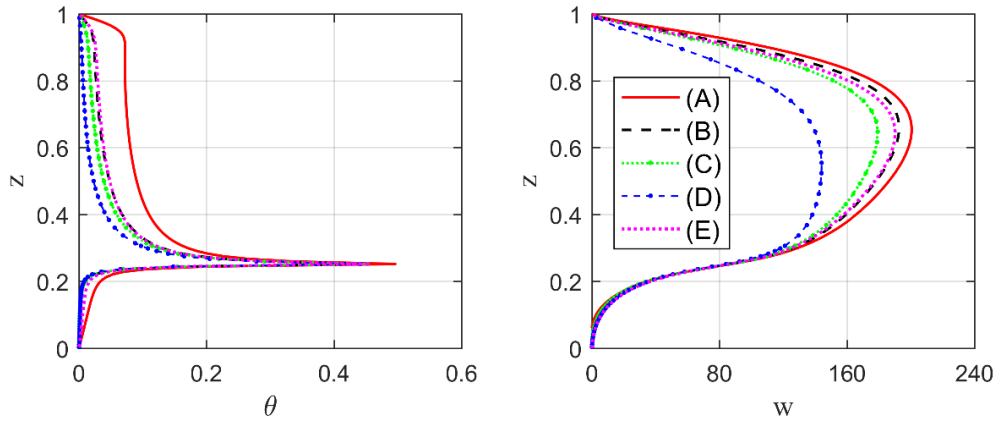

Figure 4.9. $\mathrm{Ra} = 2\times10^6$. Vertical profiles of temperature θ (left) and vertical velocity w (right) along the centerline $x = y = 0.5$.

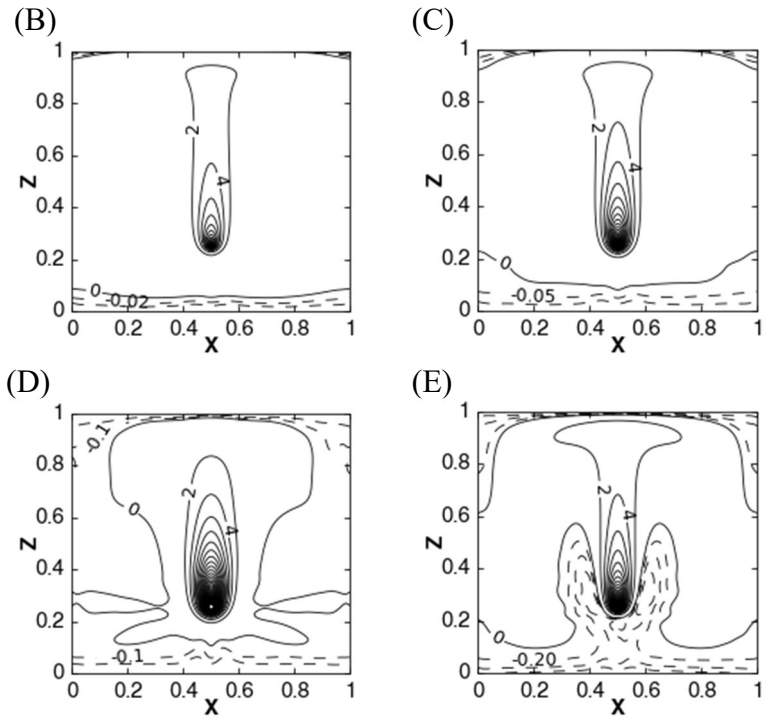

Figure 4.10. $\mathrm{Ra} = 2\times10^6$. Distribution of radiative power ($-\varphi_r'''\times10^6$) in the mid-plane $y = 0.5$ for the different participating gas.

From Figure 4.11, we also observe that the distribution of the radiative power along the centerline $x = 0.5$ more approaches that of the case $\tau = 0.2$. However, in the profile of $z = 0.5$, radiative absorption is present in case (E) for the outer regions of the plume, around $x = 0.4$ and 0.6, but absent for all the gray gases. On the contrary, the thermal and kinetic fields obtained in case (E) are more similar to those of case $\tau = 0.1$ (cf. Figure 4.9). This reflects the more complex behavior of this real gas model compared to simpler gray gas approximation.

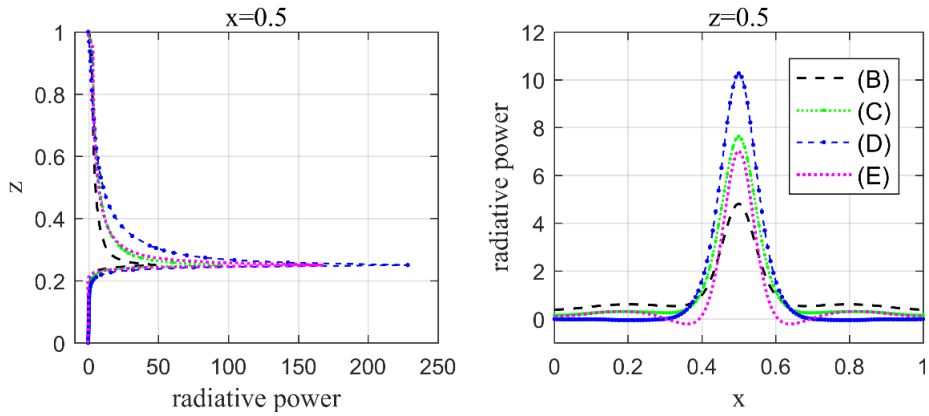

Figure 4.11. $\mathrm{Ra} = 2\times10^6$. Profiles of the radiative power ($-\varphi_r'''\times10^6$) in the mid-plane $y = 0.5$ along the lines $x = 0.5$ (left) and $z = 0.5$ (right) for the different participating media.

Table 4.6 summarizes the maximum temperature and velocities values at mid-depth, and the convective and radiative Nusselt numbers on the isothermal walls for the different cases. Compared with the pure convection (case A), the general radiation effects obtained in gray media are also found in real gas mixture: a reduction of the maximum temperature and the global circulation, and a redistribution of the heat transfer at the walls compared to the pure convective case. Besides, the radiative fluxes obtained for the real gas are lower than those of gray gases, and consequently leads to higher convective transfers.

Case	(A)	(B)	(C)	(D)	(E)
θ_{max}	0.493	0.457	0.452	0.441	0.457
u_{max}	125.2	122.4	108.9	73.3	119.4
w_{max}	201.8	194.1	179.3	144.0	191.5
$\mathrm{Nu}^{2D}_{c,\,bottom}$	0.185	0.014	0.014	0.025	0.064
$\mathrm{Nu}^{2D}_{c,\,top}$	0.813	0.215	0.111	0.031	0.258
$\mathrm{Nu}^{2D}_{r,\,bottom}$	0	0.346	0.407	0.503	0.287
$\mathrm{Nu}^{2D}_{r,\,top}$	0	0.424	0.467	0.440	0.388

Table 4.6. $\mathrm{Ra} = 2\times10^6$. Comparative results obtained in the different cases. The maximum values are evaluated in the mid plane $y = 0.5$.

4.2.3 Effects of the water vapor concentration

In this section, we focus on the effects of the water vapor concentration in the case of real gas mixture. Simulations were carried out at the reference temperature $T_{ref} = 500$ K which allows a higher saturated water content in air compared to $T_{ref} = 300$ K. Three different

values of the water vapor concentration are considered at $T_{ref} = 500$ K : $X_a = 2\%$, 10% and 20%, as reported in Table 4.7. At the new reference temperature, the Planck number is fixed at $\mathrm{Pl} = 2.44\times10^{-6}$ and the temperature ratio at $\Theta_0 = 2334.5$.

The configurations of pure convection and real gas at $X_a = 2\%$ and $T_{ref} = 300$ K are used as references to compare with these new configurations. The flow regimes corresponding to the different configurations are also given in Table 4.7, which reveals a steady sate for all radiative participating media while an unsteady state for pure convection.

Configuration	(A)	(B)	(C)	(D)	(E)
Gas medium	Transparent	Real gas	Real gas	Real gas	Real gas
Isotherm walls	$\varepsilon = 0$	$\varepsilon = 1$	$\varepsilon = 1$	$\varepsilon = 1$	$\varepsilon = 1$
Adiabatic walls	$\varepsilon = 0$	$\varepsilon = 0$	$\varepsilon = 0$	$\varepsilon = 0$	$\varepsilon = 0$
T_{ref}		500 K	500 K	500 K	300 K
X_a		2%	10%	20%	2%
ΔT		0.214 K	0.214 K	0.214 K	0.019 K
Regime	Unsteady	Steady	Steady	Steady	Steady

Table 4.7. $\mathrm{Ra} = 2\times10^6$. Configurations considered to study the effect of water vapor concentration.

Figure 4.12 displays the steady-state distributions of isotherms, stream function, and kinetic energy in the mid-plane $y = 0.5$ for the different real gaseous media compared to the time-averaged convective flow. Among the configurations at $T_{ref} = 500$ K, the growth of X_a drags a decrease of the spatial spreading of the thermal plume by increasing the absorption/emission effects of the mixture. Especially, at $X_a = 20\%$, the thermal plume is reduced in a very small region around the heat source. Consequently, the increase of X_a decreases the stream function maximum, the density of streamlines and also the kinetic energy. These observations in real gas mixture confirms the results obtained in gray media, i.e. gas radiation tends to reduce the spatial spreading of the thermal plume, and then homogenize the temperature field and weakens the global circulation. Besides, for cases (B) and (E), in which the water vapor concentration is fixed at 2%, it is noticed that the thermal plume is weakened at higher T_{ref}. The reason is that changing the reference temperature at a fixed Rayleigh number modifies the absorption properties of the medium.

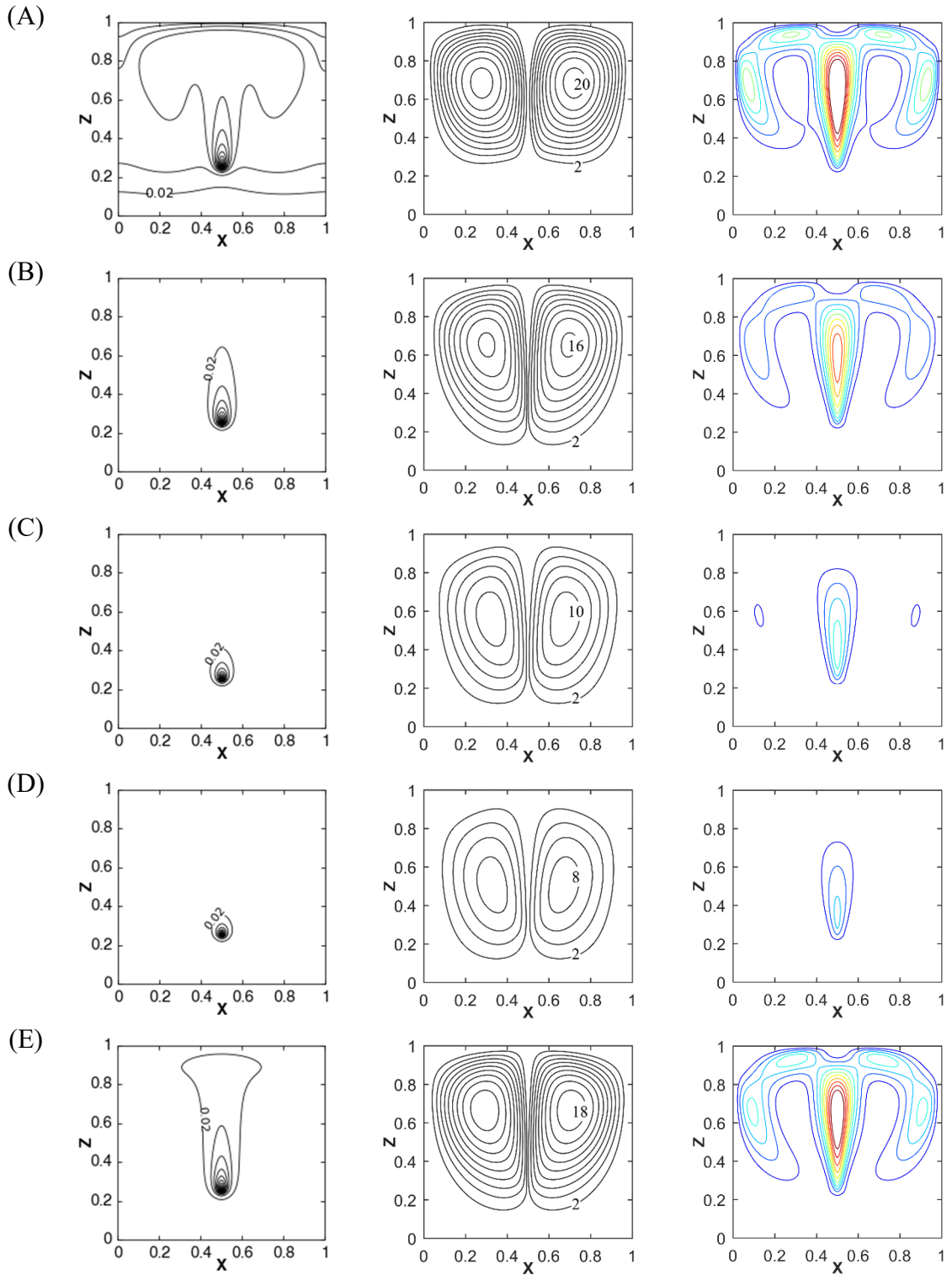

Figure 4.12. $\mathrm{Ra} = 2\times10^{6}$. Iso-contours of temperature, stream function and kinetic energy in the mid-plane $y = 0.5$ for the different configurations. Contour levels of temperature $[0.02 : 0.02 : 0.4]$. Contour levels of kinetic energy [1500:1500:15000].

Figure 4.13 presents the distributions of the radiative power ($-\varphi_r''' \times 10^{6}$) at mid-depth $y = 0.5$ for the different real gas mixtures. For configurations at $T_{ref} = 500$ K, when X_a increases, the iso-contours of dominant emission ($-\varphi_r''' > 0$) are more concentrated around

the heat source, while the radiation absorptions ($-\varphi_r''' < 0$) are more found in the regions outside the plume. Indeed, the higher is the water vapor concentration, the optically thicker is the gas medium, which leads to stronger radiative effects in the region close to the source supply.

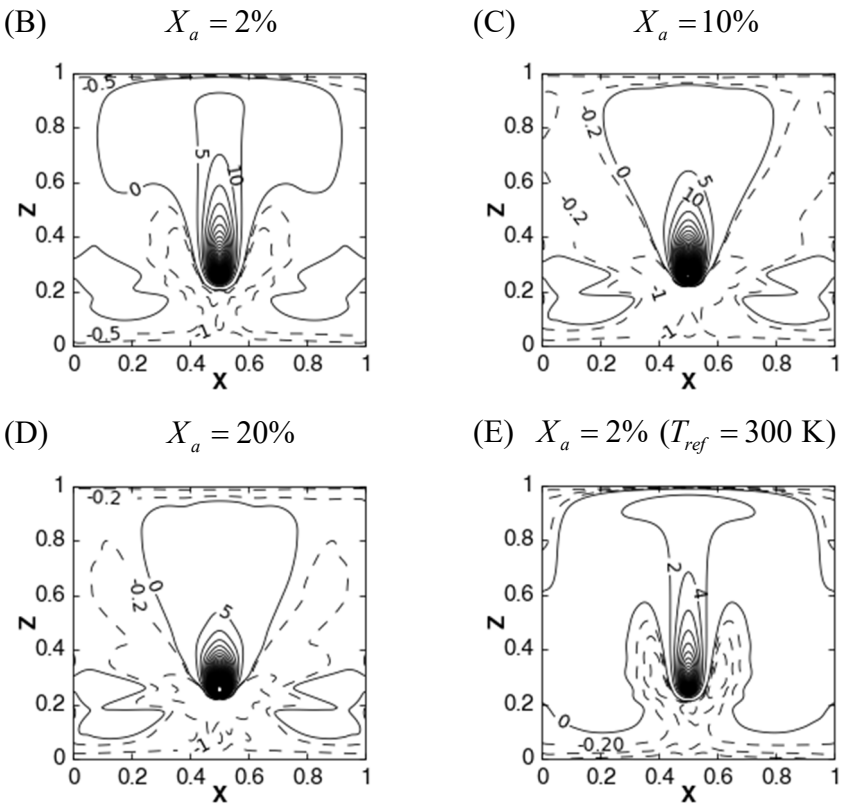

Figure 4.13. $\mathrm{Ra} = 2\times10^6$. Divergence of radiative flux ($-\varphi_r'''\times10^6$) at mid-depth $y = 0.5$ for the different configurations.

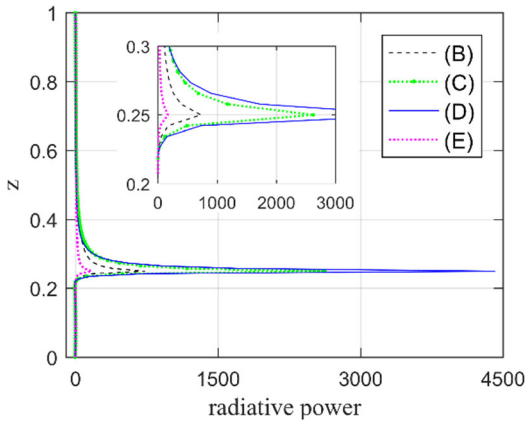

Figure 4.14. $\mathrm{Ra} = 2\times10^6$. Divergence of radiative flux ($-\varphi_r'''\times10^6$) along the centerline $x = 0.5$ at mid-depth for the different real gases.

The radiative power profiles along the centerline $x = y = 0.5$ are given in Figure 4.14. It is shown that the radiative power above the source position for $X_a = 2\%$ is much higher for

$T_{ref} = 500$ K (B) than for $T_{ref} = 300$ K (E), and increases rapidly with the growth of X_a (cases C and D). The stronger is the pic of the radiative emission, the higher is the decrease of the temperature above the source position and the reduction of the vertical velocity, as shown in Figure 4.15.

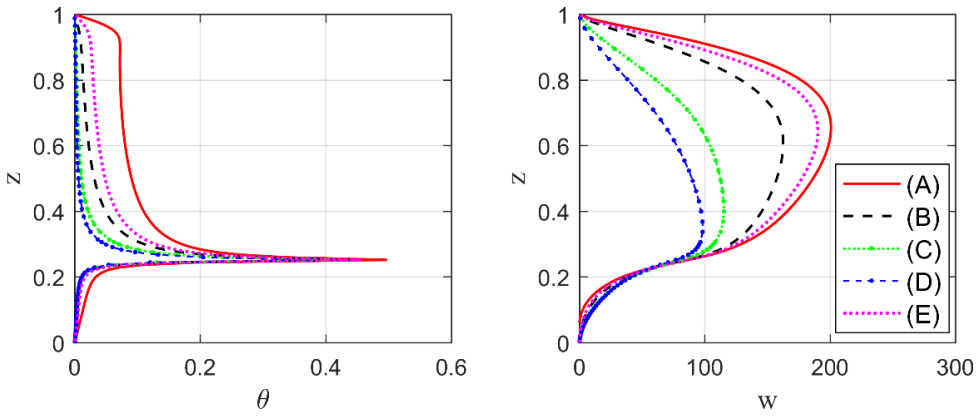

Figure 4.15. $\mathrm{Ra} = 2\times10^6$. Vertical profiles of temperature θ and vertical velocity w along the line $x = y = 0.5$.

Case	(A)	(B)	(C)	(D)	(E)
θ_{max}	0.493	0.442	0.404	0.375	0.457
u_{max}	125.2	93.6	45.4	30.5	119.4
w_{max}	201.8	163.6	116.6	99.9	191.5
$\mathrm{Nu}^{2D}_{c,\,bottom}$	0.185	0.046	0.054	0.055	0.064
$\mathrm{Nu}^{2D}_{c,\,top}$	0.813	0.089	0.030	0.025	0.258
$\mathrm{Nu}^{2D}_{r,\,bottom}$	0	0.422	0.545	0.576	0.287
$\mathrm{Nu}^{2D}_{r,\,top}$	0	0.442	0.370	0.343	0.388

Table 4.8. $\mathrm{Ra} = 2\times10^6$. Comparative results obtained in the different cases. The maximum values are evaluated in the mid plane $y = 0.5$.

The characteristic results of the maximum values at mid-depth, the convective and radiative Nusselt numbers in the different gas media are reported in Table 4.8. For all cases, the radiative fluxes are dominant in the heat exchanges at the isothermal walls. For configurations at $T_{ref} = 500$ K, with increasing X_a, the maximum temperature and velocities decrease rapidly due to the reinforced radiation effects. At $X_a = 2\%$, the wall radiative fluxes obtained at $T_{ref} = 500$ K (case B) are higher than those of $T_{ref} = 300$ K (case E), and the radiative heat transfers still increase with the water vapor concentration, and tends to more accumulate at the bottom wall.

4.3 Transitional regime

4.3.1 Periodical behavior

As described for the steady regime, gas radiation stabilizes the fluid motion and delays the transition to unsteadiness, we focus on the higher $\mathrm{Ra} = 1.2\times10^{7}$ to illustrate how the convection-radiation coupling changes the spatiotemporal dynamics of the plume and its surroundings. Two additional parameters are fixed: the Planck number at $\mathrm{Pl} = 6.73\times10^{-6}$ and the temperature ratio at $\Theta_0 = 2539.4$. Different gaseous media are investigated here: gray gases by varying the optical thickness τ and a real gas considering a small amount of water vapor in air ($X_a = 2\%$ and $T_{ref} = 300\mathrm{K}$).

Table 4.9 specifies the simulation characteristics for the different configurations. Case (A) corresponds to the pure convection configuration where the fluid is assumed to be transparent and all the walls purely reflective. As a consequence, $\varphi_r''' = 0$ in the whole domain and $q_r^{net} = 0$ at the walls. This case has been documented in the previous section 3.3.3, and will serve as a reference to assess the radiation effects.

The flow regimes corresponding to the different test cases are also given in Table 4.9. For gray gas, varying τ from 0 to 0.5 results in successive transitions from chaotic to steady state, indicating that gas radiation stabilizes the plume flow and greatly delays the transition to unsteadiness, as expected. The stabilization effect of gas radiation is also confirmed in the real gas case for which a periodic state is observed.

Configuration	(A)	(B)	(C)	(D)	(E)
Gas medium	Transparent ($\tau = 0$)	Gray gas ($\tau = 0.1$)	Gray gas ($\tau = 0.2$)	Gray gas ($\tau = 0.5$)	Real gas
Isotherm walls	$\varepsilon = 0$	$\varepsilon = 1$	$\varepsilon = 1$	$\varepsilon = 1$	$\varepsilon = 1$
Adiabatic walls	$\varepsilon = 0$	$\varepsilon = 0$	$\varepsilon = 0$	$\varepsilon = 0$	$\varepsilon = 0$
Regime	Chaotic	Periodic	Periodic	Steady	Periodic

Table 4.9. $\mathrm{Ra} = 1.2\times10^{7}$. Different configurations considered and corresponding flow regimes.

The time evolutions and spectra of total the Nusselt number for periodic plumes in the three periodic cases (B), (C) and (E) are presented in Figure 4.16. The values of the amplitudes and frequency peaks are reported in Table 4.10. It is clearly visible that the total heat flux at walls exhibits a periodic nature in the three cases. From $\tau = 0.1$ to 0.2, the oscillation amplitude is greatly reduced as well as the associated frequency.

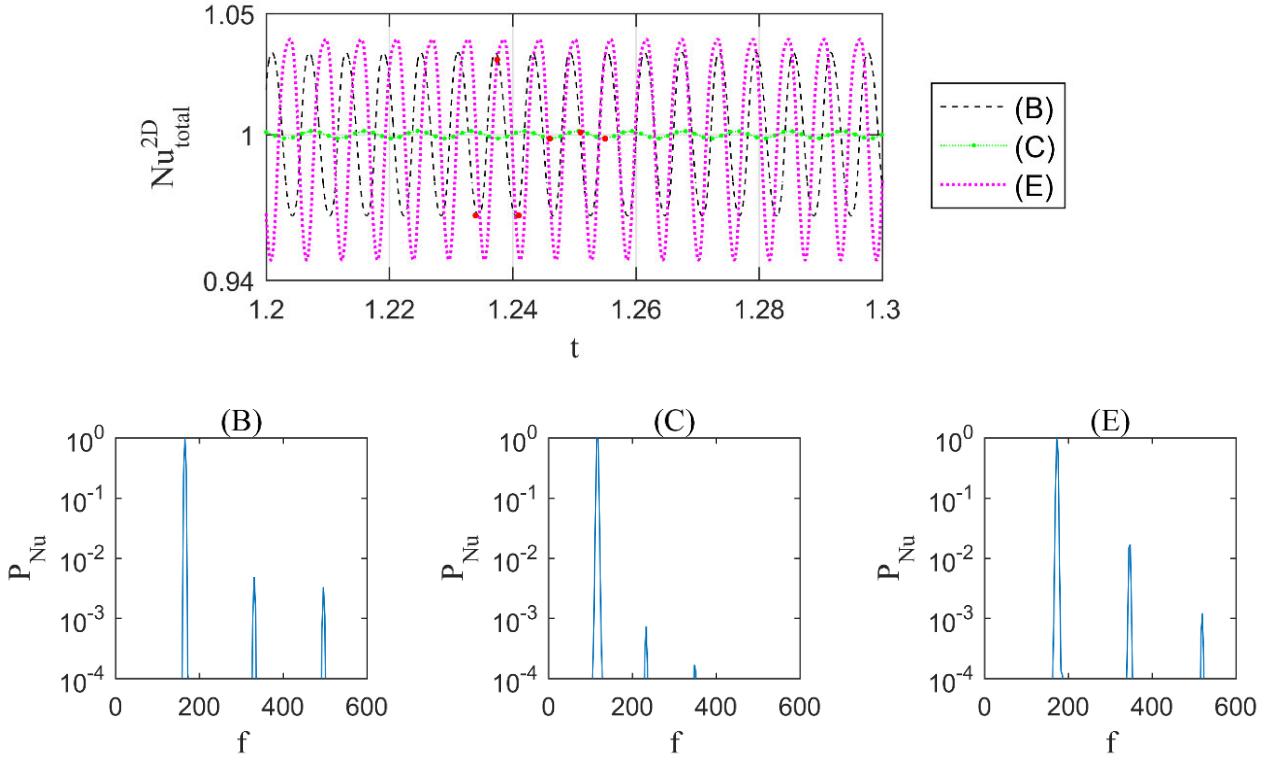

Figure 4.16. $\mathrm{Ra} = 1.2\times10^{7}$. Time evolution and spectra of total Nusselt number Nu^{2D}_{total} for (B) gray gas $\tau = 0.1$, (C) gray gas $\tau = 0.2$ and (E) real gas.

Case	(B)	(C)	(E)
Amplitude	0.0674	0.0035	0.0907
Frequency	165.30	116.35	172.10

Table 4.10. $\mathrm{Ra} = 1.2\times10^{7}$. Amplitudes and frequencies for periodic flows.

Instantaneous temperature fields in the three different planes $y = [0.25;\ 0.5;\ 0.75]$ at different times within one period, marked in Figure 4.16 (red dots) for the cases of $\tau = 0.1$ and 0.2, are visualized in Figure 4.17 and Figure 4.18. The antisymmetric mode described in the pure convective plume is also observed here: the plume oscillates in each plane apart the mid one relatively to the vertical centerline $x = 0.5$, with opposite phases. With the augmentation of τ, the gas radiation effects are strengthened, so that the plume spreading and its lateral oscillations are reduced.

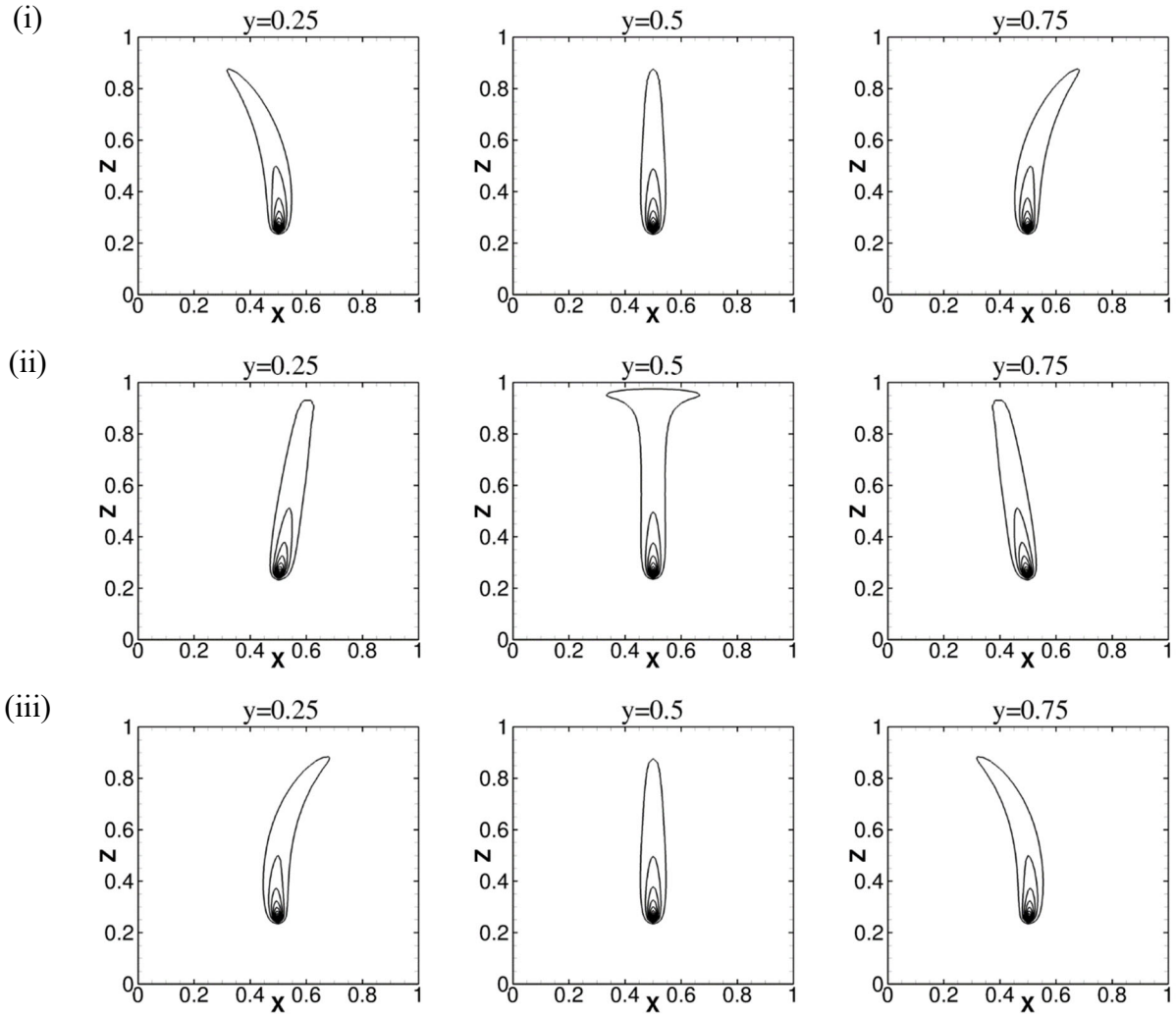

Figure 4.17. $\mathrm{Ra} = 1.2\times10^{7}$. Snapshots of the iso-contours of temperature at three depths $y = [0.25;\ 0.5;\ 0.75]$ over one cycle of oscillation for $\tau = 0.1$. Contour levels (0.02:0.02:0.4).

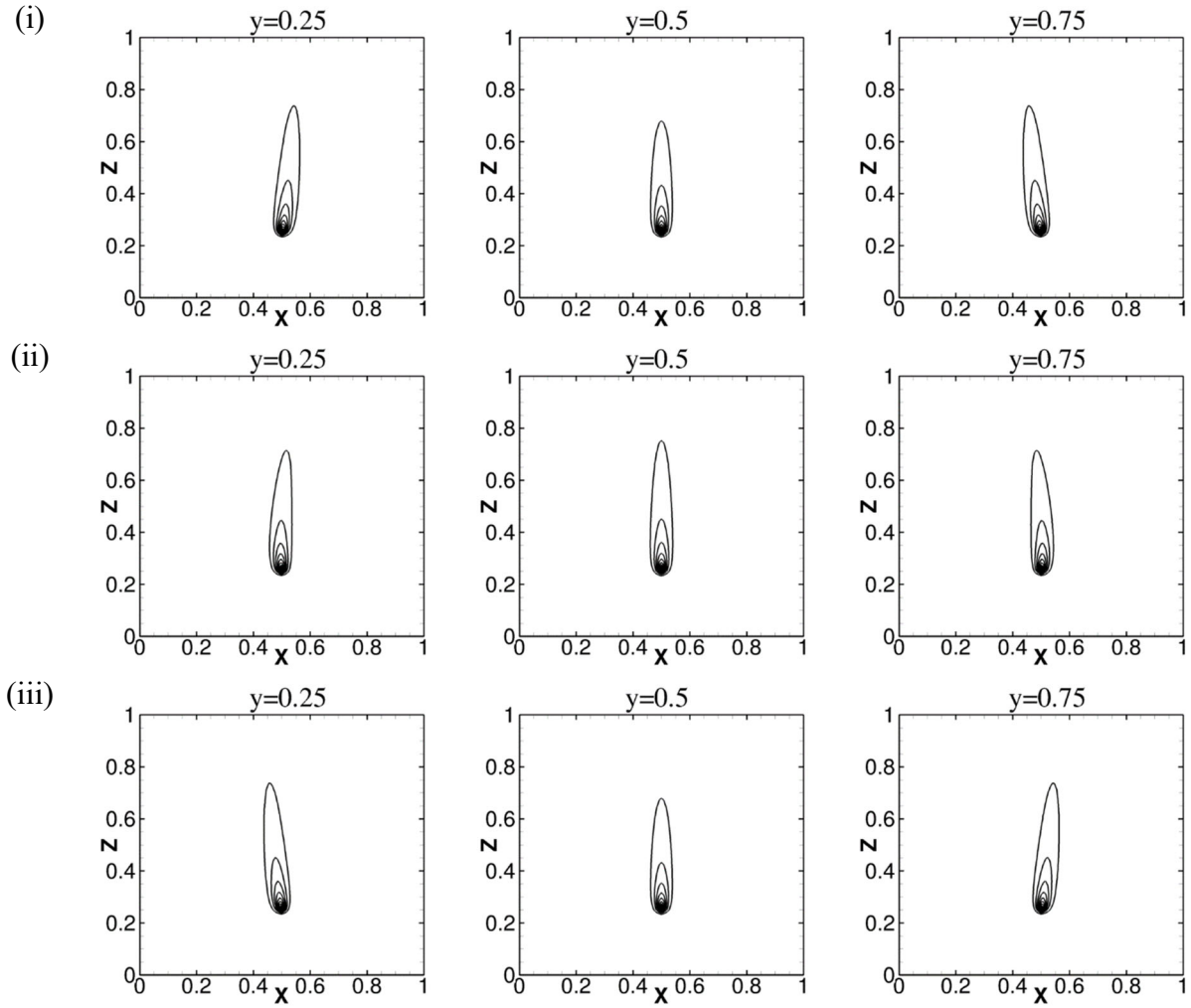

Figure 4.18. $\mathrm{Ra} = 1.2\times10^{7}$. Snapshots of the iso-contours of temperature at three depths $y = [0.25;\ 0.5;\ 0.75]$ over one cycle of oscillation for $\tau = 0.2$. Contour levels (0.02:0.02:0.4).

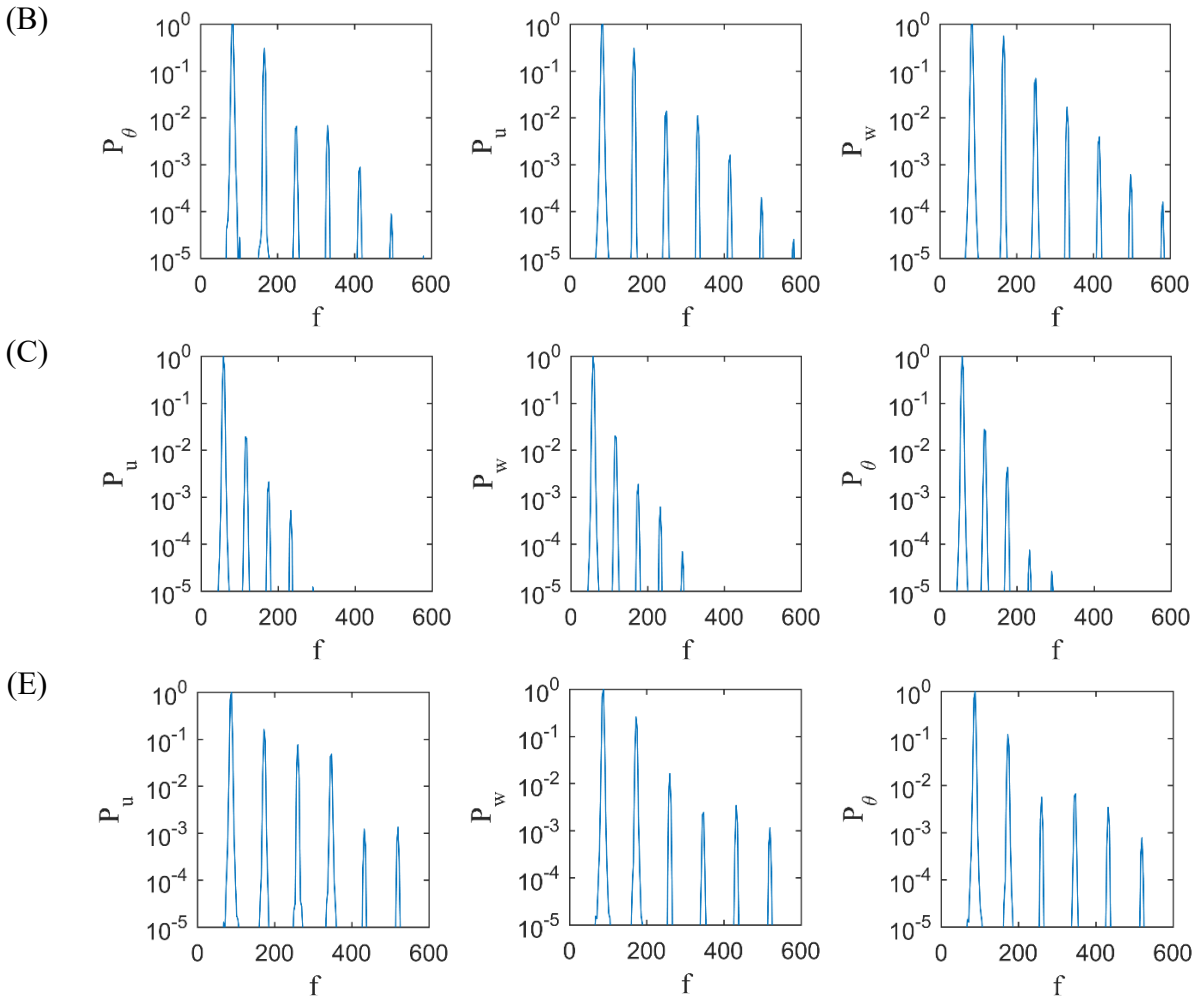

Figure 4.19. $\mathrm{Ra} = 1.2\times10^{7}$. Density power spectra of u, w and θ at the point A_1 for the different configurations.

Case	Variable	f_1	$2f_1$	$3f_1$	$4f_1$
(B)	u	82.65	165.30	247.95	330.60
	w	82.65	165.30	247.95	330.60
	θ	82.65	165.30	247.95	330.60
(C)	u	58.17	116.35	174.53	232.71
	w	58.17	116.35	174.53	232.71
	θ	58.17	116.35	174.53	232.71
(E)	u	86.05	172.10	258.16	344.21
	w	86.05	172.10	258.16	344.21
	θ	86.05	172.10	258.16	344.21

Table 4.11. $\mathrm{Ra} = 1.2\times10^{7}$. Frequency peaks at the monitoring point A_1 for the different configurations.

Figure 4.19 and Figure 4.20 present the power spectra of u, w and θ for the periodic flows at the monitoring points A_1 and B_1, respectively. Note again that point A_1 is located laterally away from the centerline of the plane $y = 0.25$ and the point B_1 is in the centerline (cf. Figure 3.1). From Figure 4.19, it is observed that at the point A_1, for each case separately, the three variables u, w and θ have the same fundamental frequency and harmonics, as reported in Table 4.11. We observe that as τ increases, the frequency f_1 decreases and the number of harmonics is reduced, meaning that the plume motion is stabilized by gas radiation. At the point B_1, only f_1 and its odd harmonics are present in the u-spectrum while only even harmonics are present for w and θ. The reason is the symmetry of the fluid motion already described in the pure convective case.

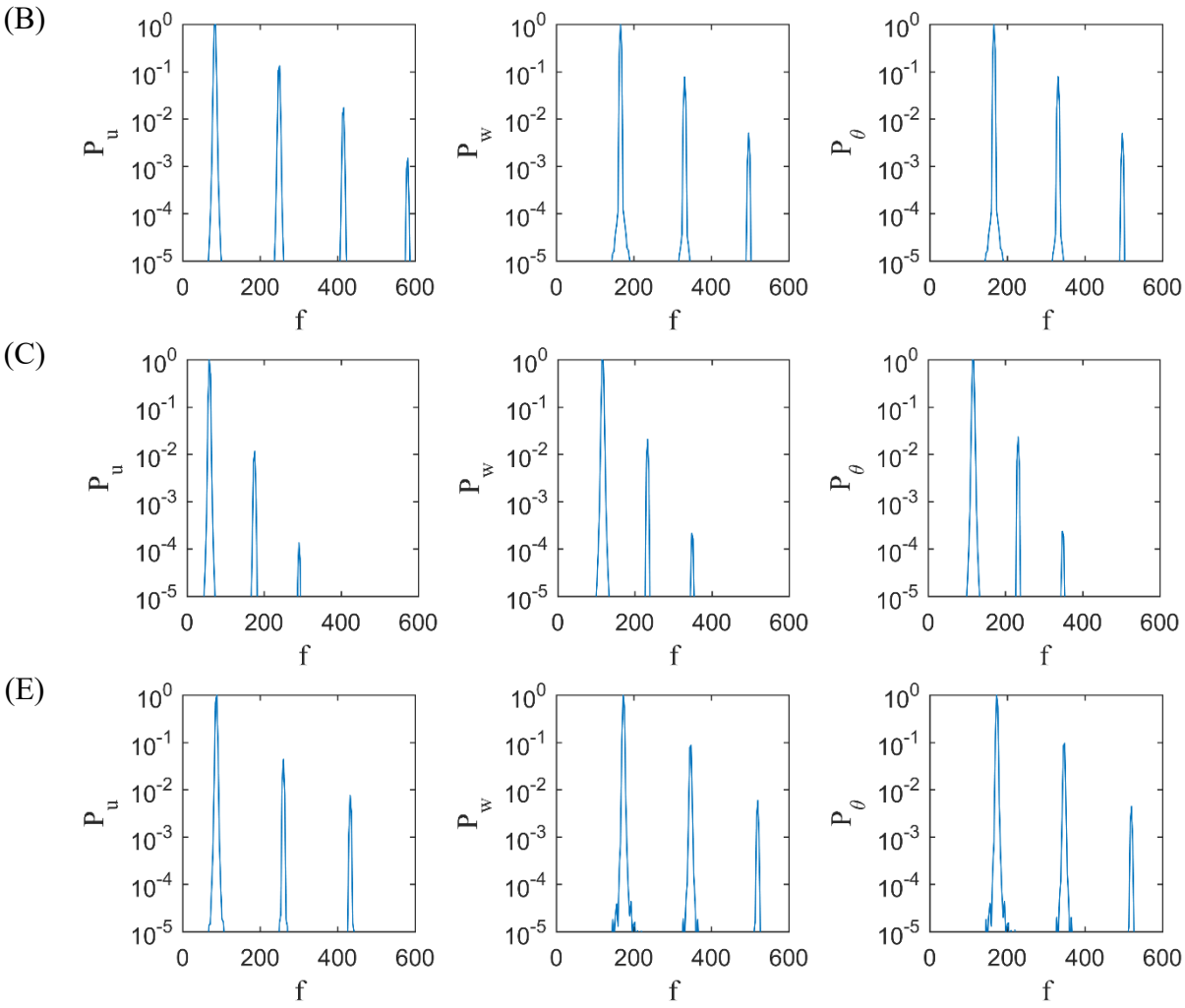

Figure 4.20. $\mathrm{Ra} = 1.2 \times 10^7$. Density power spectra of u, w and θ at the point B_1 for the different configurations.

Case	Variable	f_1	$2f_1$	$3f_1$	$4f_1$
(B)	u	82.65		247.95	
	w		165.30		330.60
	θ		165.30		330.60
(C)	u	58.17		174.53	
	w		116.35		232.71
	θ		116.35		232.71
(E)	u	86.05		258.16	
	w		172.10		344.21
	θ		172.10		344.21

Table 4.12. $\mathrm{Ra} = 1.2 \times 10^7$. Frequency peaks at the monitoring point B_1 for the different configurations.

4.3.2 Time-averaged fields

Figure 4.21 displays the spatial distributions of time-averaged fields of temperature $\overline{\theta}$, 2D kinetic energy $\overline{E}_k = (\overline{u}^2 + \overline{w}^2)/2$ and streamlines of the time-averaged flow in the mid-plane $y = 0.5$ for the different configurations. When gas radiation is involved, whatever gray media or real gas mixture, the spatial spreading of the thermal plume is reduced, as observed in the steady cases. With the increase of the optical thickness, the temperature field is gradually homogenized in the cavity, because radiation becomes the dominant heat transfer mode. Accounting gas radiation also changes the temperature distribution in the far-field of the plume. The fluid outside the plume plane is quasi-isothermal for the gray gases (cases B, C, D), and the thermal stratification established in the case A is not found in these cases. The real gas case (E) appears as an intermediate case between cases A and B, with a horizontal fluid layer of cold gas still present in the bottom part of the cavity.

Regarding the kinetic energy, the gas radiation effect is not monotonic. For weak values of τ (case B), $\overline{E}_k$ slightly increases when compared to the pure convective case A, in particular in the plume plane. For higher optical thicknesses τ (cases C and D), the radiation effects are enhanced and the kinetic energy $\overline{E}_k$ is weakened, but the global flow circulation still fills the domain above the source.

The dipole positions for the different configurations are [0.76, 0.77, 0.74, 0.73, 0.77] for respectively cases (A) to (E). The change of the dipole location follows the kinetic energy evolution, with a slight upward shift of the main vortices from the pure convection (case A) to cases $\tau = 0.1$ and real gas (cases B and E), and a moderate downward shift for τ varying from 0.1 to 0.5 (cases B to D). The horizontal profiles of temperature and velocity at different heights are then plotted in Figure 4.22. A downward shift is present in temperature profiles

at the different heights. For vertical velocity profiles, we notice that the profile shapes and the maxima are quite similar in all the cases, contrarily to the steady state cases (see Figure 4.5).

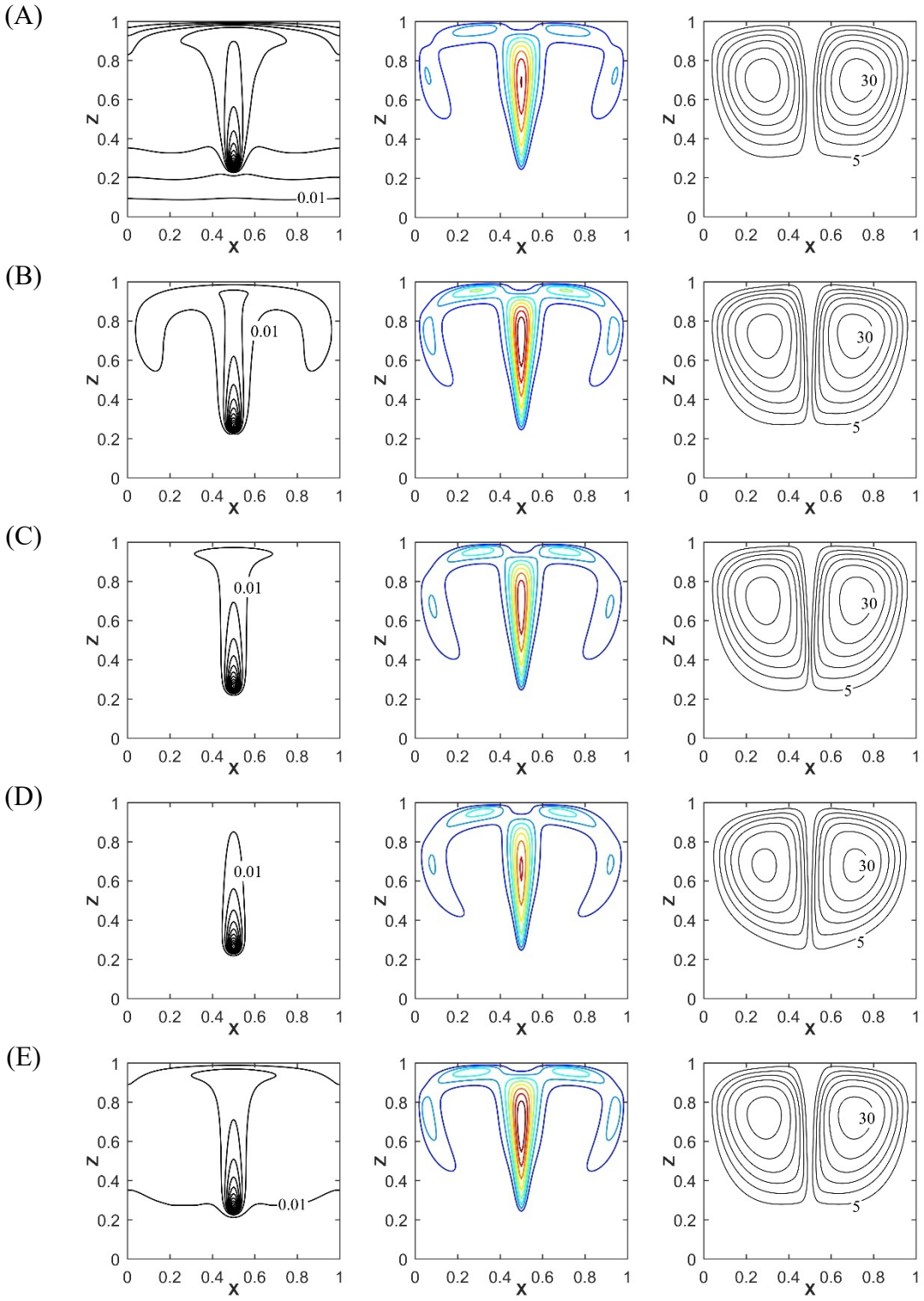

Figure 4.21. $\mathrm{Ra} = 1.2 \times 10^7$. Iso-contours of time-averaged temperature, stream function and kinetic energy in the mid-plane $y = 0.5$ for the different configurations. Contour levels of temperature [0.01:0.01:0.4]. Contour levels of kinetic energy [0:8000:80000].

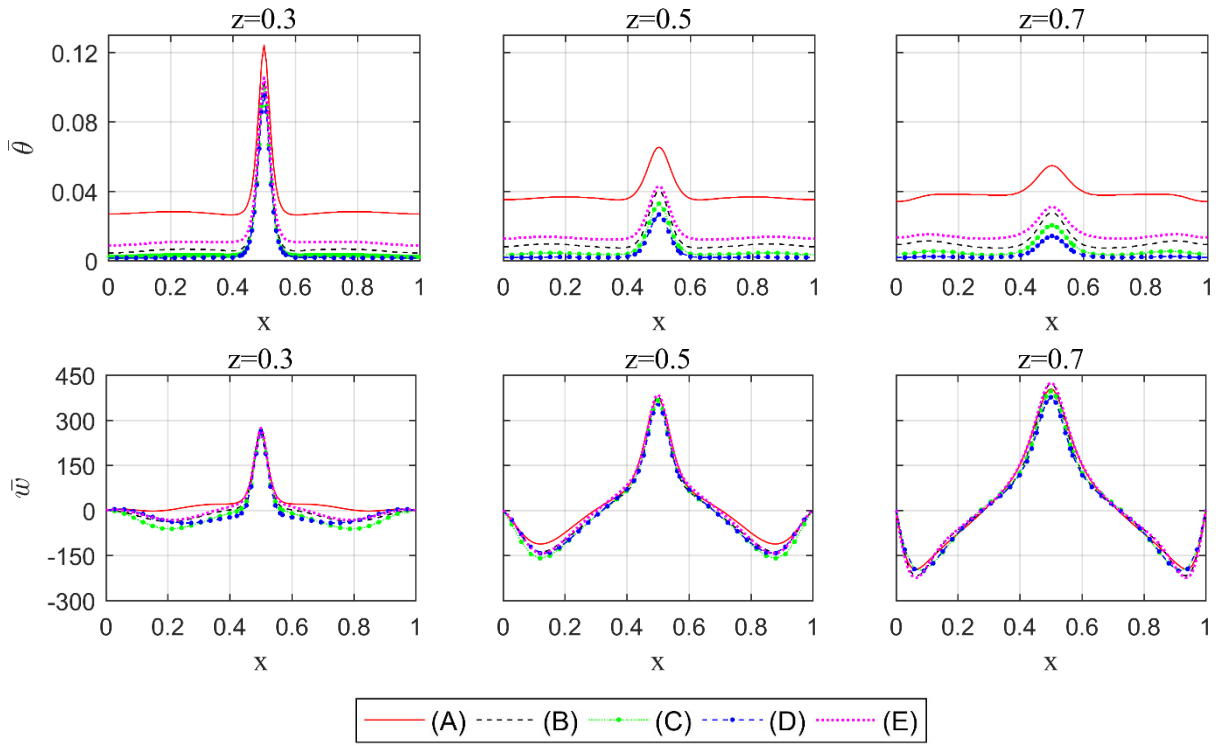

Figure 4.22. $\mathrm{Ra}=1.2\times10^{7}$. Horizontal profiles of temperature $\overline{\theta}$ and vertical velocity $\overline{w}$ at different heights.

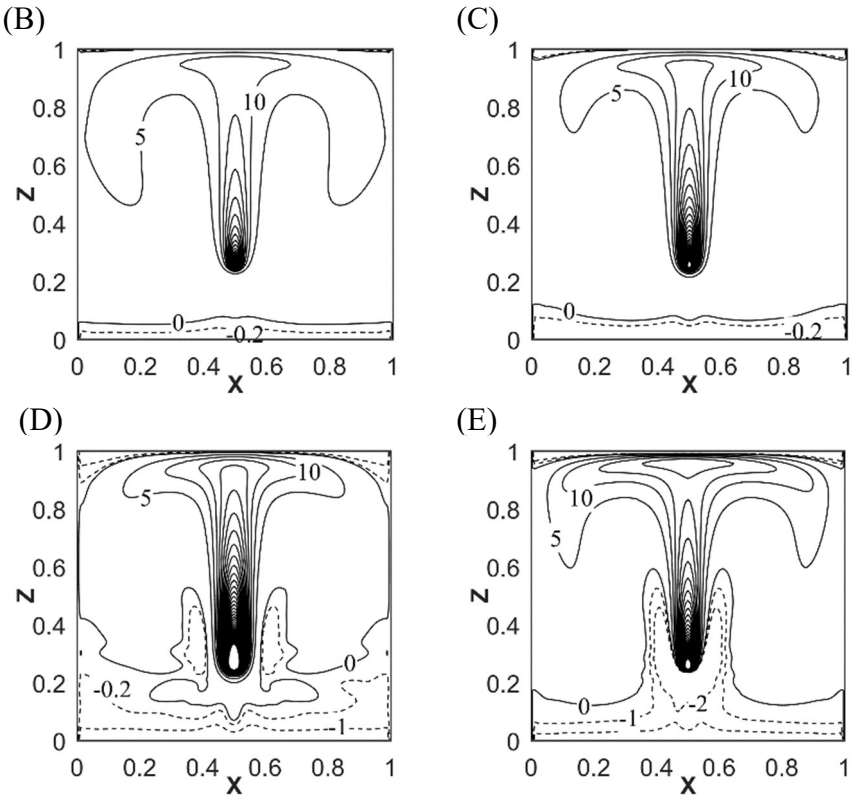

Figure 4.23. $\mathrm{Ra}=1.2\times10^{7}$. Distribution of radiative power ($-\overline{\varphi}_r'''\times10^{6}$) at mid-depth $y=0.5$ in different participating gas.

The distributions of the time-averaged radiative power ($-\overline{\varphi}_r'''\times10^6$) at mid-depth $y=0.5$ are presented in Figure 4.23, and the corresponding profiles along the lines $x=0.5$ and $z=0.5$ are plotted in Figure 4.24. They show that the fluid is mainly emitting ($-\overline{\varphi}_r'''>0$) in most part of the cavity while the regions of dominant absorption ($-\overline{\varphi}_r'''<0$) are reduced to the vicinity of the top wall and to the bottom part of the cavity, mainly under the source. The radiative power reaches its higher values above the source, and the horizontal spreading of the emission zone seems to be relatively unaffected by the radiative properties of the fluid (Figure 4.24 (b)). As observed in steady state cases ($\mathrm{Ra}=2\times10^6$), radiative exchanges in the absorption areas are almost negligible compared to emission areas, except for the real gas (case E). In this case, higher absorption levels are observed than in the other cases, and a specific absorption area is found surrounding the heat source.

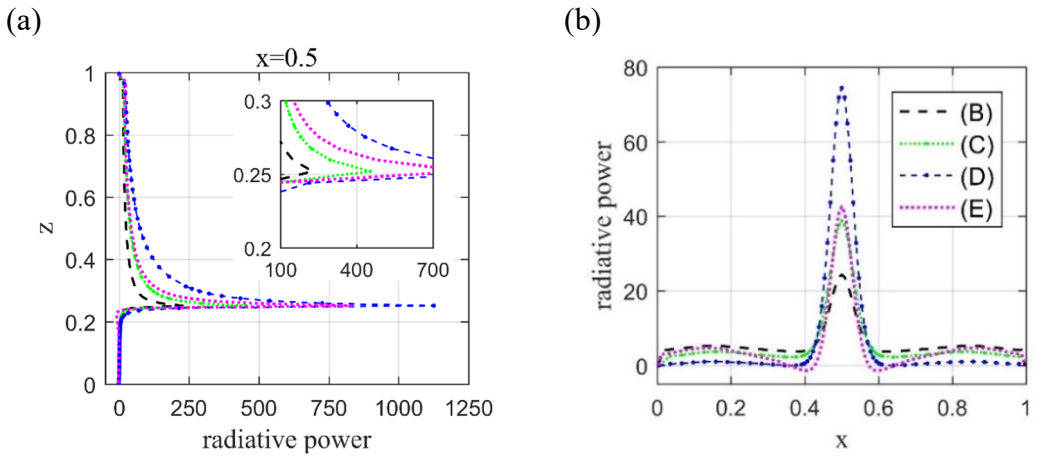

Figure 4.24. $\mathrm{Ra}=1.2\times10^7$. Profiles of radiative power ($-\overline{\varphi}_r'''\times10^6$) along the lines (a) $x=0.5$ and (b) $z=0.5$ in different participating gas.

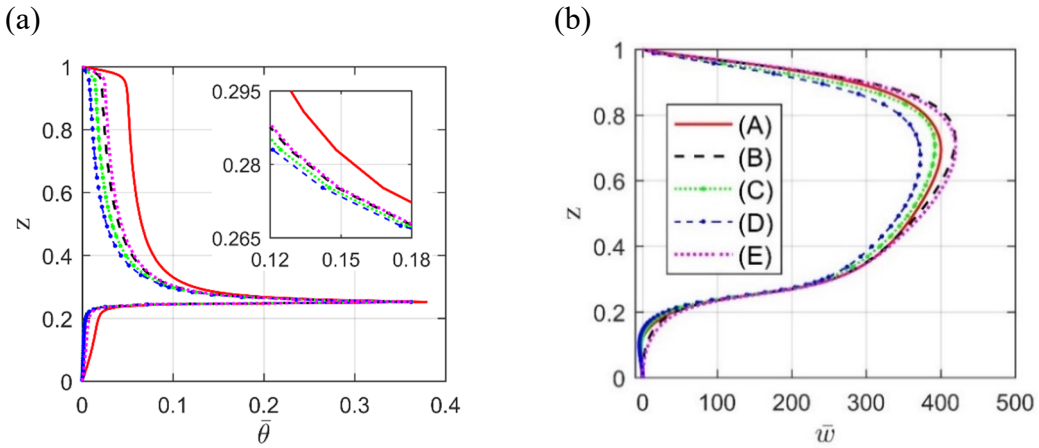

Figure 4.25. $\mathrm{Ra}=1.2\times10^7$. Vertical profiles of temperature $\overline{\theta}$ and vertical velocity $\overline{w}$ along the line $x=y=0.5$.

Because of the absorption/emission mechanisms in the medium, the optically thicker is the medium, the more important is the radiative power and the less is the slope of the radiative power profile at the source location (cf. Figure 4.24). Compared to the pure convective case, this induces a higher drop of the temperature profile as observed in Figure 4.25 (a), and then the weakening of the thermal plume and the reduction of its spatial extension.

The vertical velocity profiles along the centerline for the different cases are plotted in Figure 4.25 (b). For the transitional regime, the vertical velocity varies with the optical thickness in a different manner from that observed in steady state (Figure 4.4). The decrease in temperature differences in the cavity leads to a decrease in the plume velocity and the subsequent global flow for optically thicker ones (cases C and D), where the plume temperature is rapidly lower comparatively to case A. However, we observe an acceleration of the plume in the case of a thin optical medium (cases B and E), although the plume temperature is here again lower than in case A (but to a lesser extent than cases C and D). For the real gas mixture considered here, whereas the radiative absorption regions are close to those of case $\tau = 0.2$ and 0.5 (Figure 4.23), the resulting temperature and vertical velocity distributions finally much resembles to those of case $\tau = 0.1$, which again proves the more complex behavior of real gas model than the simplified gray gas approximation.

Case	(A)	(B)	(C)	(D)	(E)
Gas medium	Transparent $\tau = 0$	Gray gas $\tau = 0.1$	Gray gas $\tau = 0.2$	Gray gas $\tau = 0.5$	Real gas
$\overline{\theta}_{\max}$	0.379	0.3617	0.3624	0.3619	0.3614
$\overline{w}_{\max}$	404.4	424.3	397.1	378.0	424.5
$\overline{E}_{k,\max}$	8.04×10^4	9.0×10^4	7.88×10^4	7.14×10^4	9.01×10^4
$\overline{\mathrm{Nu}}^{2D}_{c,\text{ bottom}}$	0.135	0.014	0.012	0.019	0.056
$\overline{\mathrm{Nu}}^{2D}_{c,\text{ top}}$	0.863	0.311	0.230	0.106	0.346
$\overline{\mathrm{Nu}}^{2D}_{\mathrm{r,\ bottom}}$	0	0.297	0.330	0.401	0.242
$\overline{\mathrm{Nu}}^{2D}_{\mathrm{r,\ top}}$	0	0.376	0.427	0.472	0.355

Table 4.13. $\mathrm{Ra} = 1.2\times10^7$. Comparative results between the different configurations.

Table 4.13 summarizes the maximum values of temperature, vertical velocity and kinetic energy in the mid-depth plane as well as the Nusselt numbers on the isothermal walls for the different cases. When gas radiation is taken into account, the maximum of temperature is kept rather constant whatever the participating medium, but it is reduced of around 4% when compared to case (A). Gas radiation also redistributes the energy transfer along the isothermal walls between radiative and convective parts. As found in steady plumes, the growth of τ

decreases the convective heat transfer due to the homogenization effect of gas radiation on the temperature field, and radiation gradually becomes the dominant mode of heat transfer. In the particular conditions considered here (H, T_{ref}, X_{ref}, etc.), the results obtained for the real gas are comparable to those obtained for the thinner optical gray gas.

4.4 Turbulent regime

Finally, the effects of gas radiation on turbulent plumes are investigated at $\mathrm{Ra} = 10^9$ by considering three configurations, as listed in Table 4.14. Case (A) corresponds to pure natural convection, case (B) the gray gas approximation with $\tau = 0.1$, and a real gas case (C), with X_a fixed at 2% at a reference temperature $T_{ref} = 300$ K. The Planck number is fixed at $\mathrm{Pl} = 5.61 \times 10^{-4}$ and the temperature ratio at $\Theta_0 = 30.4$.

Configuration	(A)	(B)	(C)
Gas medium	Transparent	Gray gas ($\tau = 0.1$)	Real gas
Isotherm walls	$\varepsilon = 0$	$\varepsilon = 1$	$\varepsilon = 1$
Adiabatic walls	$\varepsilon = 0$	$\varepsilon = 0$	$\varepsilon = 0$
Transient time	0.07	0.04	0.04
Statistical time	0.09	0.09	0.09
Total CPU time	8, 000 h	16, 000 h	88,000h
Processors	64	512	512

Table 4.14. $\mathrm{Ra} = 10^9$. Different configurations considered and corresponding CPU time.

Simulations of cases (B) and (C) were performed on the supercomputer Jean-Zay of Idris center by using 512 processors of a 2.5 GHz Intel Cascade Lake 6248. The total CPU consumption for the different configurations are reported in Table 4.14. Statistics of the flow have been obtained over a dimensionless time interval of 0.09 for all cases.

4.4.1 Time and grid space convergence

Figure 4.26 shows the probability distribution functions (PDF) of the axial velocity v at the monitoring point B_2 obtained for the different configurations. It can be seen that all the PDF profiles have a null mean value. Besides, the PDF profiles are quite similar between gray gas and real gas cases, but differ from the transparent one.

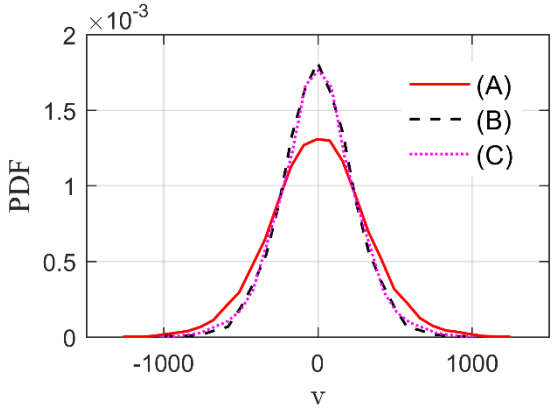

Figure 4.26. $\mathrm{Ra} = 10^9$. Normalized PDF of the axial velocity v at the point B_2 for the different configurations.

To ensure the grid resolution, the ratio between the grid size $\delta r = (\delta x \delta y \delta z)^{1/3}$ and the Kolmogorov scale η_k was checked *a posteriori* for each configuration. The maximum of this ratio $\delta r / \pi \eta_k$ is: case $(A) = 0.64$, case $(B) = 0.69$, case $(C) = 0.67$, which well satisfies the Grötzbach requirement for turbulent flow modelling (cf. section 1.2.5).

4.4.2 Instantaneous flow description

Temperature snapshots in the planes $y = 0.5$ and $z = 0.5$ are presented in Figure 4.27. When gas radiation is considered, the plume behavior appears to be less chaotic than that in the pure convective situation. It seems that in cases (B) and (C), the spatial structures are fewer and mainly located near the top wall.

Figure 4.28 displays a more global visualization of the flow structures for the different cases, by using the positive iso-value surfaces of the Q criterion (cf. section 3.4.2). In the more chaotic case (A), the vortices are produced within the ascending motion as well as the downstream motion after the impact on the top wall, and the transition to turbulence seems to occur around mid-height of the cavity.

For the participating media (B) and (C), gas radiation delays the transition to turbulence further upstream above the heat source, and induces less vortices in the cavity. It is also observed that these unsteady structures are mainly produced close to the top wall and may be related to the impact phenomenon, which is consistent with the observations in Figure 4.27, indicating again the stabilization effect of gas radiation on the flow.

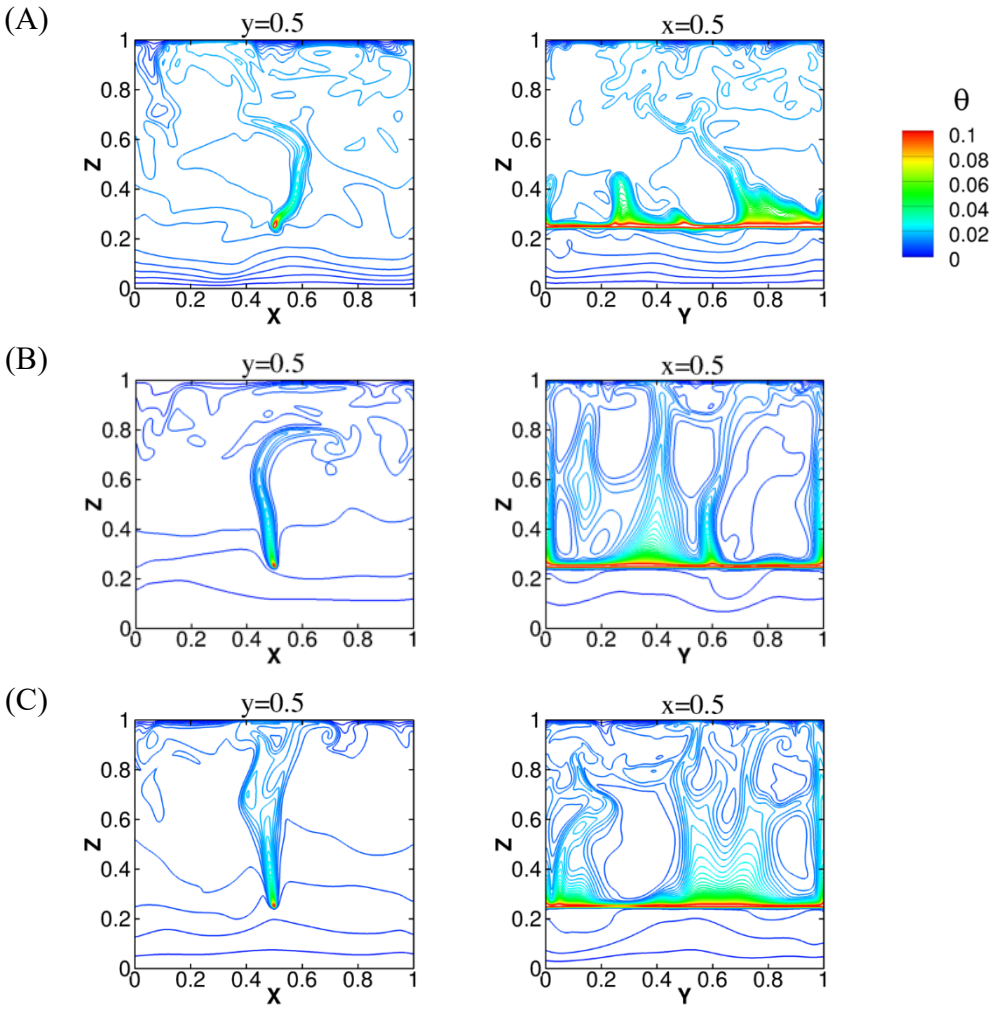

Figure 4.27. $\mathrm{Ra}=10^9$. Instantaneous fields of temperature θ in the planes $y=0.5$ and $x=0.5$ for the configurations (A) pure convection, (B) gray gas and (C) real gas.

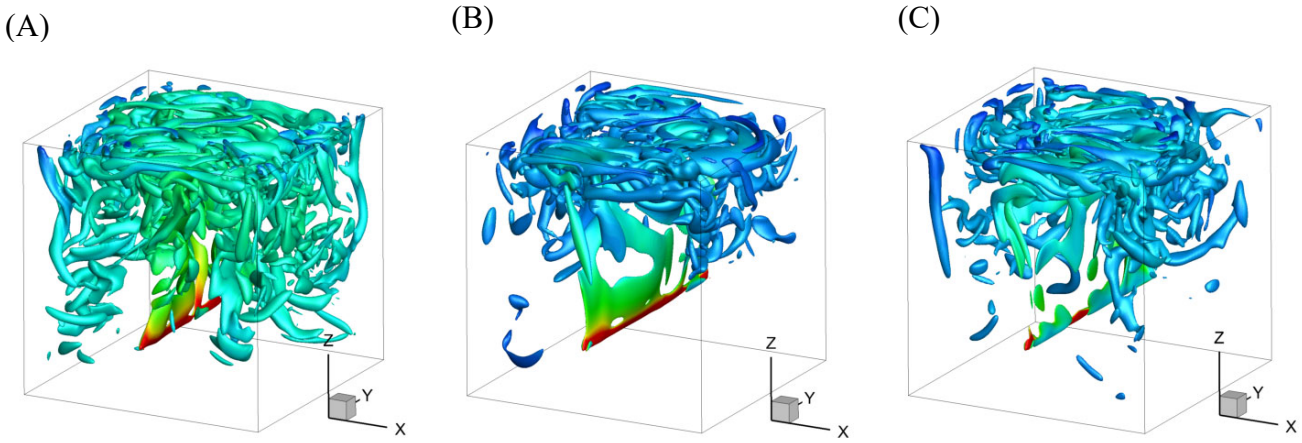

Figure 4.28. $\mathrm{Ra}=10^9$. Iso-surface of instantaneous Q criterion colored by temperature for the configurations (A) pure convection, (B) gray gas, and (C) real gas ($\mathrm{Q}=10^8$).

4.4.3 Time-averaged and fluctuating fields

Figure 4.29 and Figure 4.30 display the time-averaged temperature fields and the horizontal profiles at three heights in the mid-plane $y = 0.5$. As already observed in steady and transient regimes, gas radiation leads to a reduction of the temperature variations in the cavity and to the homogenization of the horizontal fluid layers near the isothermal walls. However, the decrease in the mean temperature values is not found in the area slightly above the heat source (see Figure 4.30 at $z = 0.3$). It should be noted that in the radiative participating media, the maximum temperature is almost the same when compared to pure convection (cf. Table 4.15).

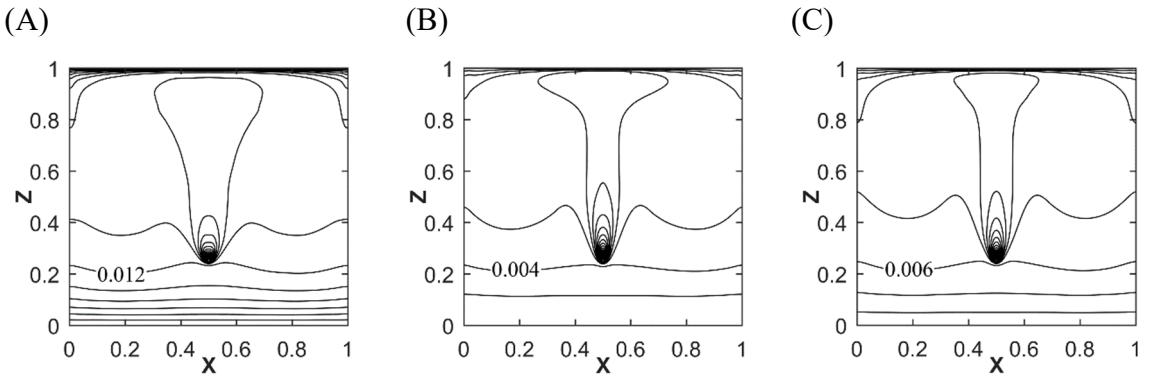

Figure 4.29. $\mathrm{Ra} = 10^9$. Time-averaged temperature contours $\overline{\theta}$ in the plane $y = 0.5$ for the different configurations at. Contour levels $\overline{\theta} = [0.002 : 0.002 : 0.1]$.

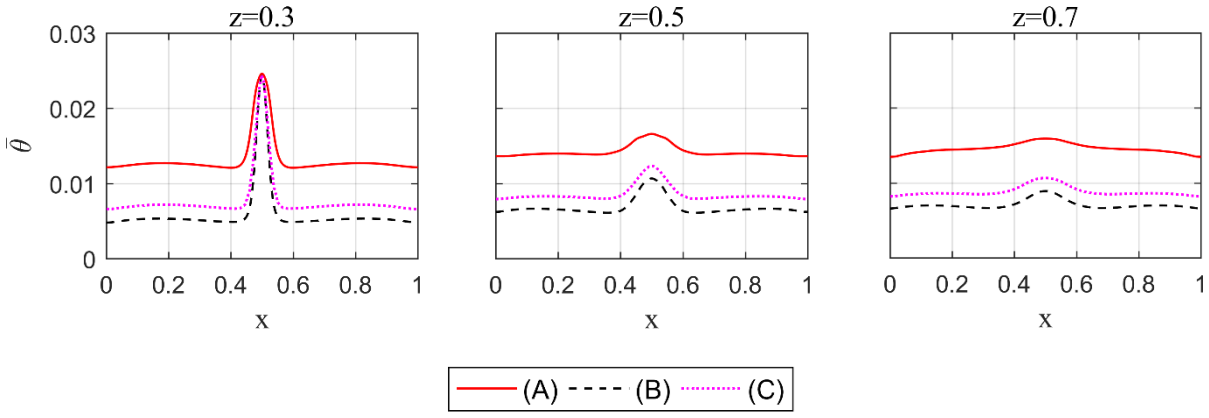

Figure 4.30. $\mathrm{Ra} = 10^9$. Horizontal profiles of temperature $\overline{\theta}$ at different heights.

The stream function of the time averaged flow and the 2D mean kinetic energy field in the mid-plane are shown in Figure 4.31 and Figure 4.32, respectively, as well as some horizontal profiles ($\overline{w}$, $\overline{u}$, and $\overline{E}_k$) in Figure 4.33. It can be seen that the general structure of the mean flow (vertical plume and lateral recirculation regions) is always preserved. But when

radiation is accounted for, the lateral expansion of the plume is narrowed (see Figure 4.32 and Figure 4.33 (c)). This narrowing of the fluid motion in the plume plane induces an acceleration of the flow above the source and then results in a higher kinetic energy in the plume plane, as found in the transitional cases that gas radiation enhances the flow dynamics in an optically thin medium.

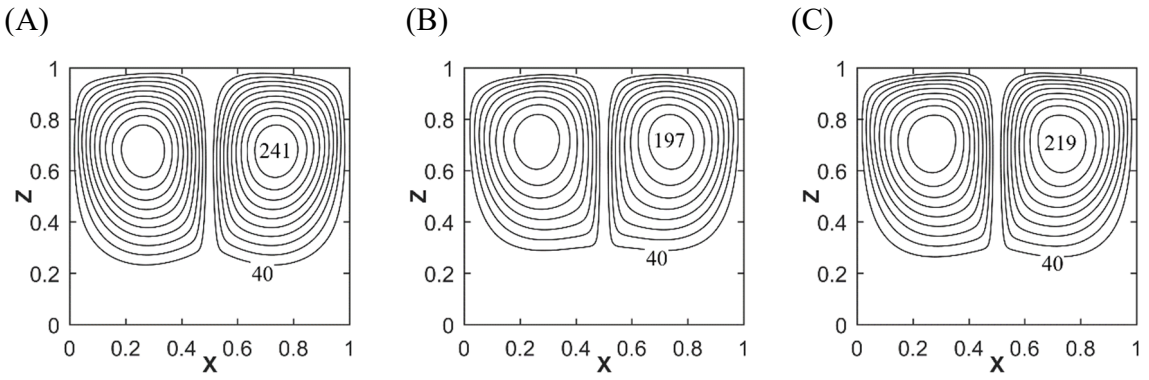

Figure 4.31. $\mathrm{Ra}=10^9$. Distributions of time-averaged streamlines $\overline{\psi}$ in the plane $y=0.5$ for the different configurations. Contour levels $\overline{\psi}=[40:20:220]$.

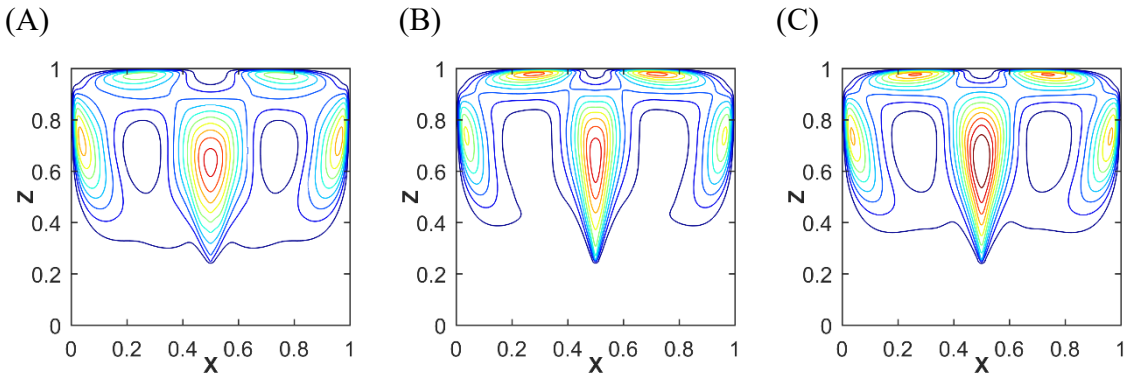

Figure 4.32. $\mathrm{Ra}=10^9$. Time-averaged 2D kinetic energy contours $\overline{E}_k$ in the plane $y=0.5$ for the different configurations. Contour levels $\overline{E}_k=[5\times10^4:5\times10^4:5.5\times10^5]$.

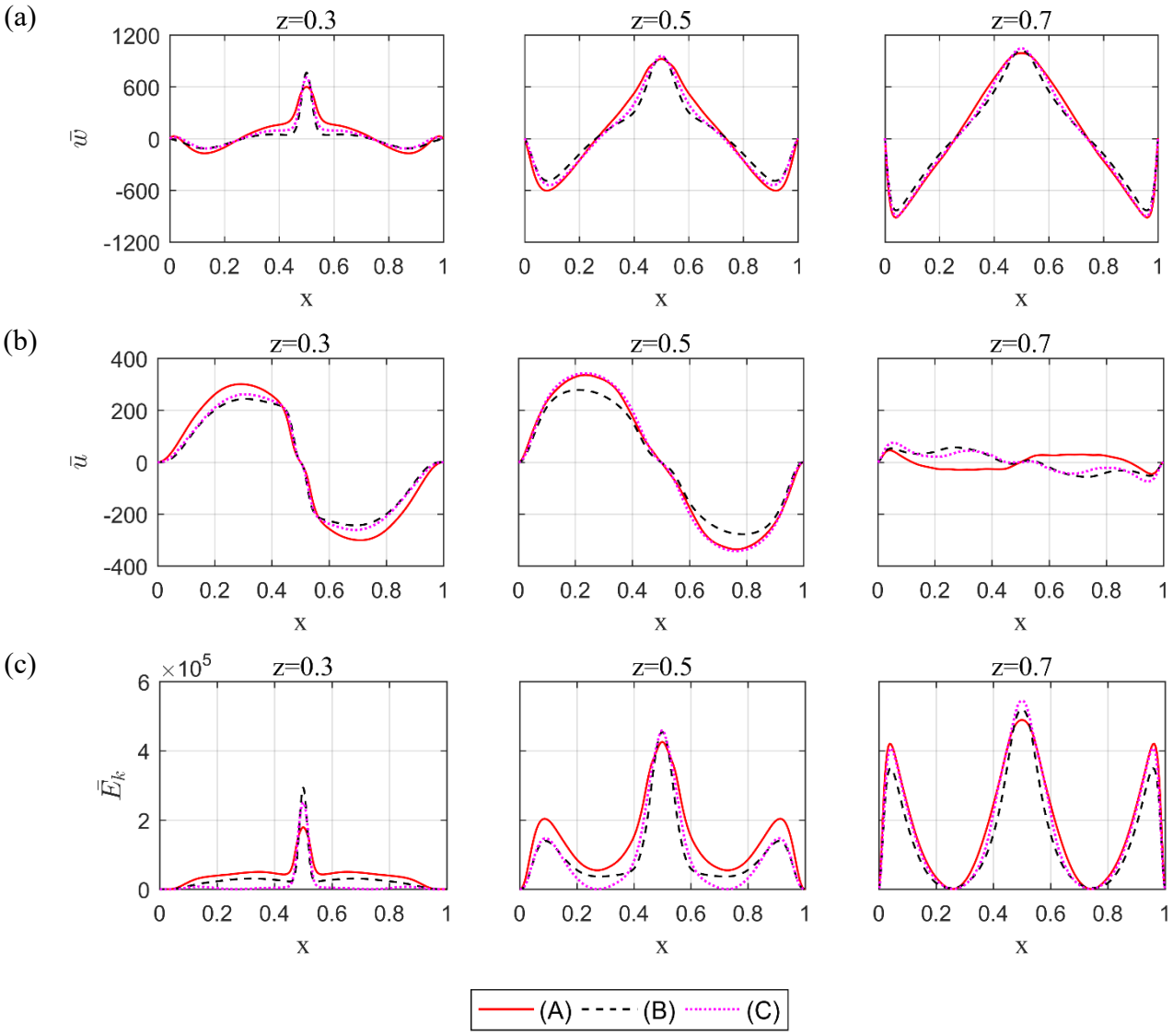

Figure 4.33. $\mathrm{Ra} = 10^9$. Horizontal profiles of (a) vertical velocity $\bar{w}$, (b) horizontal velocity $\bar{u}$ and (c) 2D kinetic energy $\bar{E}_k$ at different heights.

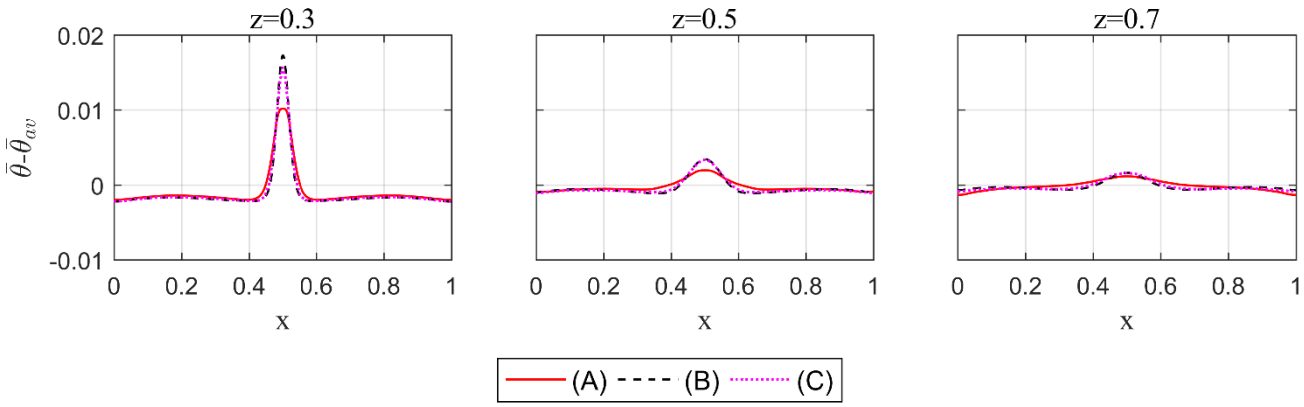

Figure 4.34. $\mathrm{Ra} = 10^9$. Horizontal profiles of reduced temperature $\overline{\theta} - \overline{\theta}_{av}$ at different heights.

The horizontal profiles of the reduced temperature $\overline{\theta} - \overline{\theta}_{av}$ are then plotted in Figure 4.34. Contrarily to what was found for the steady state (cf. Figure 4.6), the maximum values of $\overline{\theta} - \overline{\theta}_{av}$ are increased in cases (B) and (C) when compared with pure convection, which is probably because in the convective case, the higher turbulence level of plume flow tends to decrease the thermal stratification ($\partial\theta / \partial z$) outside the plume.

Figure 4.35 and Figure 4.36 show respectively the distributions of temperature fluctuations θ_{rms} and turbulence kinetic energy k in the mid-plane $y = 0.5$ for the different configurations. We can note the centerline symmetry of the fields is roughly preserved, which indicates a satisfactory degree of convergence of the statistics. For all the configurations, large thermal fluctuations are located around the heat source position, while the turbulent kinetic energy is more important in the upper part of the cavity, that is in the turbulent region of the plume and return flow.

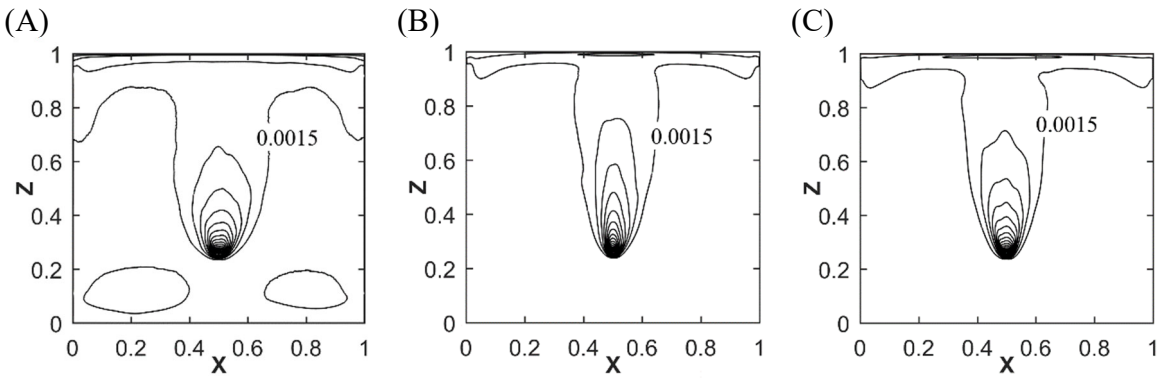

Figure 4.35. $\mathrm{Ra} = 10^9$. Distribution of temperature fluctations θ_{rms} in the mid-plane $y = 0.5$. Contour levels (0.0015:0.0015:0.03).

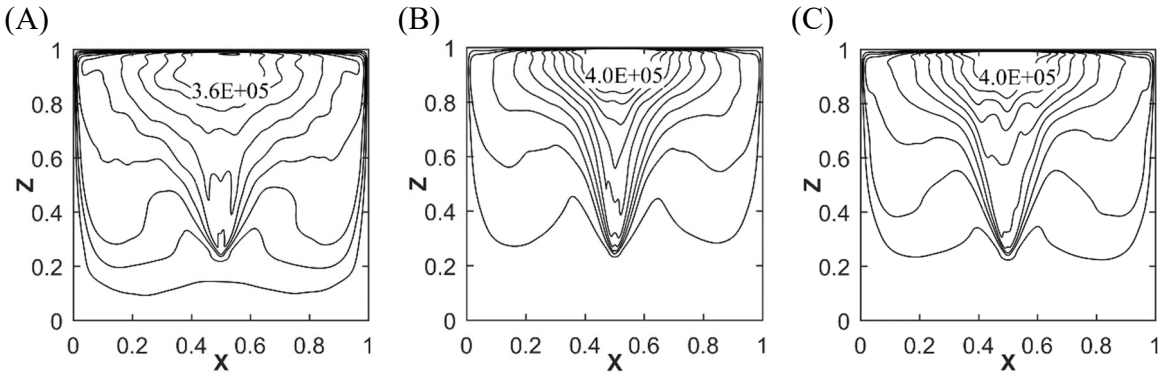

Figure 4.36. $\mathrm{Ra} = 10^9$. Distribution of turbulent kinetic energy k in the mid-plane $y = 0.5$. Contour levels ($4\times10^4 : 4\times10^4 : 4\times10^5$).

The corresponding profiles of θ_{rms} and k at different heights are given in Figure 4.37. In cases (B) and (C), the fluctuations exhibit higher maximum values and narrower distributions in the plume core when compared to the pure convective case. But the higher turbulent quantities levels outside the plume observed in the latter case and the broader spatial distribution (Figure 4.37 (b), $z = 0.7$) indicates a more developed turbulent flow than those obtained with radiation.

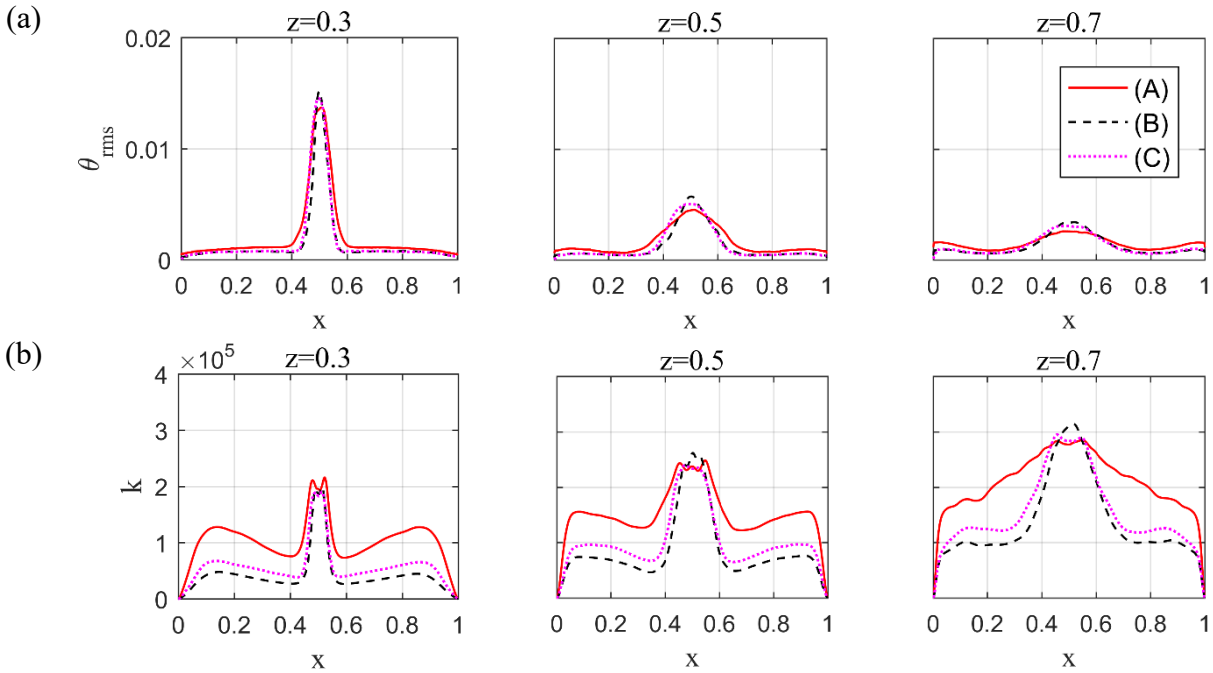

Figure 4.37. $\mathrm{Ra} = 10^9$. Horizontal profiles of (a) temperature fluctuation θ_{rms} and (b) turbulent kinetic energy k at different heights.

The description of the mean fields mentioned above only concerns the mid-depth plane $y = 0.5$. To examine the 3D structure of the flow, Figure 4.38 displays the time-averaged kinetic energy in different *x*-planes. Compared to the pure convective case, the kinetic energy fields in cases (B) and (C) are enhanced near the top wall while they are weakened near the left and right walls ($x = 0$ and 1), indicating that gas radiation changes the kinetic energy distribution in the overall cavity. It is also noticed that in the real gas mixture (case (C)), the kinetic energy fields are more concentrated around the mid-depth $y = 0.5$.

The redistribution of the mean kinetic energy can be related to the turbulence kinetic energy field, as shown in Figure 4.39. In accordance to what observed on the horizontal *k* profiles, turbulence is more present near the top wall and less developed in the lateral planes $x = 0.2$ and 0.8 for participating media.

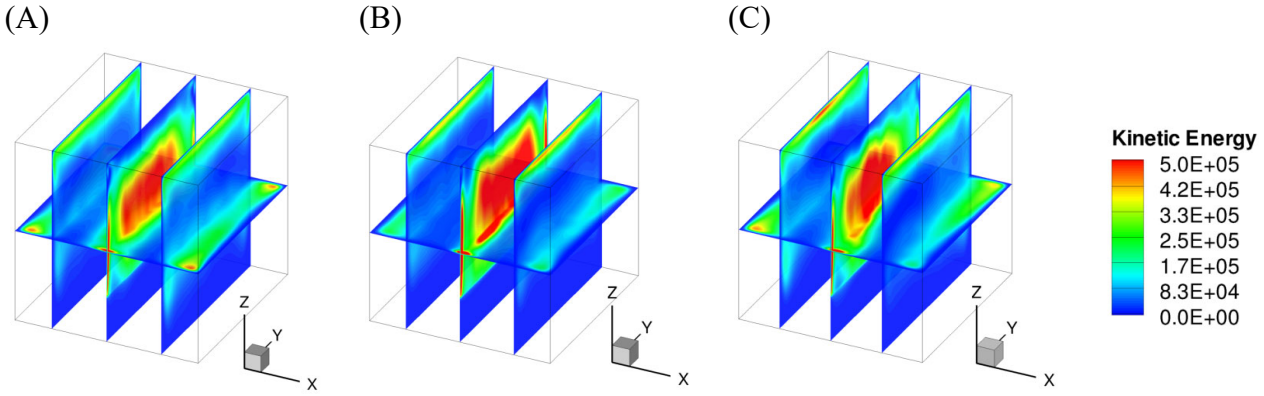

Figure 4.38. $\mathrm{Ra} = 10^9$. Spatial distribution of time-averaged kinetic energy in the planes $x = [0.2;\ 0.5;\ 0.8]$ and $z = 0.5$ for the different cases.

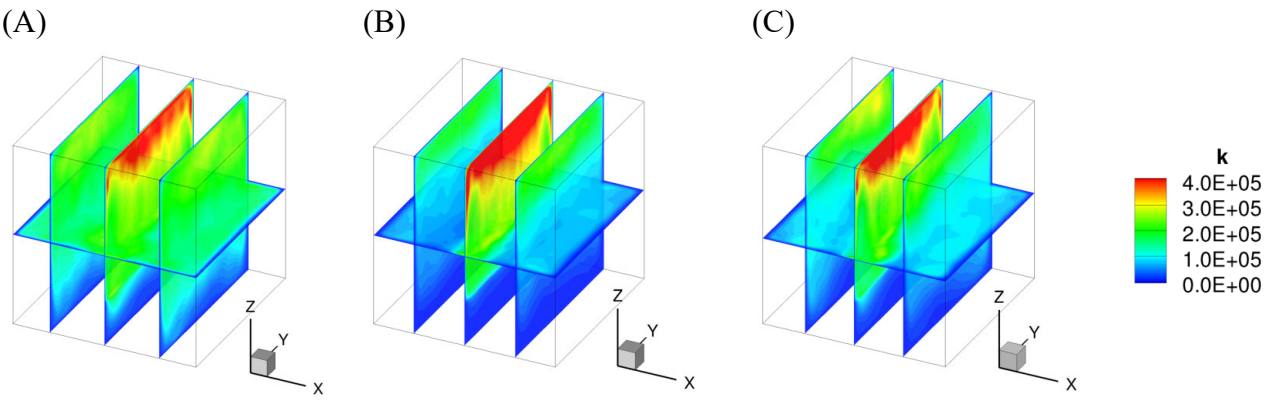

Figure 4.39. $\mathrm{Ra} = 10^9$. Spatial distribution of turbulence kinetic energy in the planes $x = [0.2;\ 0.5;\ 0.8]$ and $z = 0.5$ for the different cases.

The distributions of time-averaged radiative power ($-\overline{\varphi}_r''' \times 10^6$) at mid-depth $y = 0.5$ are presented in Figure 4.40, and the corresponding profiles along the lines $x = 0.5$ and $z = 0.5$ are shown in Figure 4.41. As observed at lower Ra numbers, the fluid is mainly emitting

($-\overline{\varphi}_r''' > 0$) in the most part of the cavity with an intensity much greater than that of the absorption regions. The radiative power reaches its maximum level above the heat source. For the real gas mixture (case (C)), the radiative power is much larger than that in case (B) for the area above the source supply. However, for the regions laterally away from the centerline, the radiative power obtained in case (C) is lower than that in case (B) (cf. Figure 4.41 (right)).

Figure 4.42 plots the distribution of mean temperature and vertical velocity along the centerline $x = y = 0.5$. It is shown that radiative heat transfer enhances the temperature decay rapidly, excepted for the source location, where the maximum temperature is slightly increased (see Table 4.15). Due to these energy redistributions and temperature evolutions, the plume dynamics are reinforced above the heat source, which was also observed in unsteady plumes for optically thin medium.

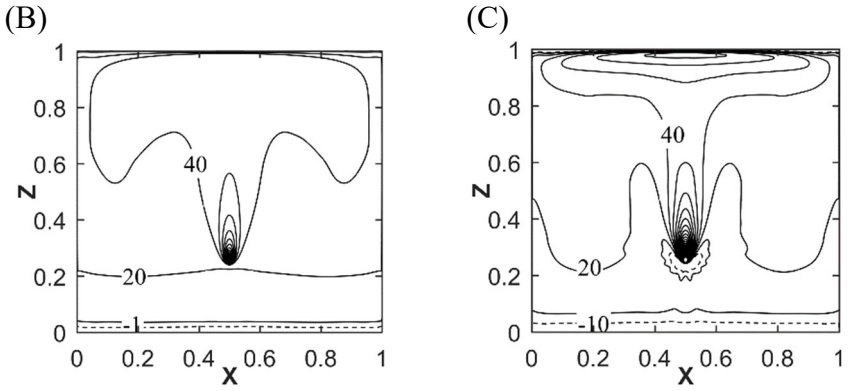

Figure 4.40. $\mathrm{Ra} = 10^9$. Distribution of the time-averaged radiative power ($-\overline{\varphi}_r''' \times 10^6$) at mid-depth $y = 0.5$ in the cases of gray medium and real gas mixture.

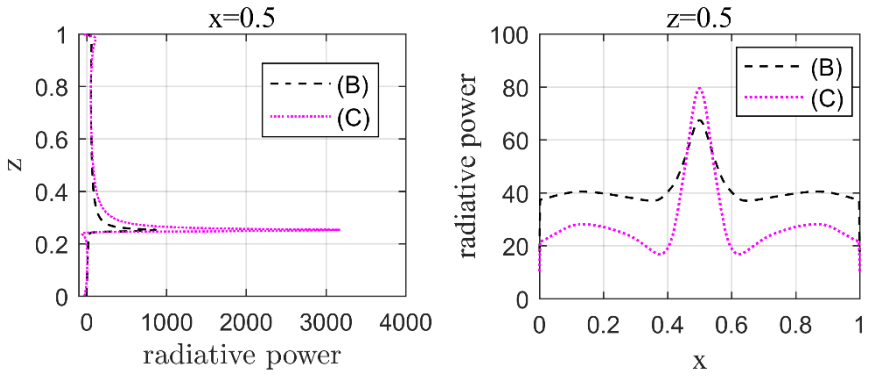

Figure 4.41. $\mathrm{Ra} = 10^9$. Profiles of mean radiative power ($-\overline{\varphi}_r''' \times 10^6$) along the lines $x = 0.5$ (left) and $z = 0.5$ (right) at the mid-depth $y = 0.5$ in the cases of gray medium and real gas mixture.

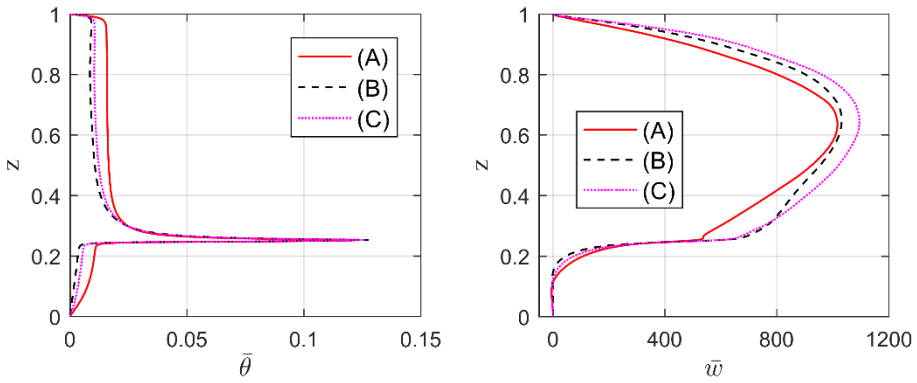

Figure 4.42. $\mathrm{Ra}=10^9$. Profiles of temperature $\bar{\theta}$ (left) and vertical velocity $\bar{w}$ (right) along the centerline $x=y=0.5$.

Table 4.15 summarizes the maximum temperature and velocity values at mid-depth $y=0.5$, and also the convective and radiative Nusselt numbers over the isothermal walls for the three cases. Due to the energy redistribution by gas radiation, there is an increase of the maximum vertical velocity and kinetic energy in the present real gas mixture or thin gray medium, when compared to the pure convective case. Gas radiation also influences the heat transfer along the isothermal walls by decreasing the convective fluxes.

Case	(A)	(B)	(C)
Gas medium	Transparent	Gray gas	Real gas
$\bar{\theta}_{\max}$	0.1249	0.1274	0.1260
$\bar{w}_{\max}$	1.01×10^3	1.03×10^3	1.09×10^3
$\bar{E}_{k,\max}$	5.17×10^5	5.32×10^5	5.99×10^5
$\overline{\mathrm{Nu}}^{2D}_{c,\mathrm{bottom}}$	0.109	0.017	0.048
$\overline{\mathrm{Nu}}^{2D}_{c,\mathrm{top}}$	0.890	0.511	0.570
$\overline{\mathrm{Nu}}^{2D}_{r,\mathrm{bottom}}$	0	0.211	0.154
$\overline{\mathrm{Nu}}^{2D}_{r,\mathrm{top}}$	0	0.260	0.227

Table 4.15. $\mathrm{Ra}=10^9$. Comparative results between the different configurations.

4.4.4 Time spectra

Figure 4.43 and Figure 4.44 presents the power spectra of vertical velocity and temperature at the monitoring points A_2 and B_2 in the mid-plane $y=0.5$ (see Figure 3.1 for their exact locations). In the convective case (A), the −5/3 power law of the Kolmogorov

decay is present in each spectrum, which corresponds to the inertial region of the spectrum. In the temperature fluctuations spectrum, a decay following a -3 power law appears at the two monitoring points due to the thermal turbulent dissipation.

When radiation is taken into account, the energy contained in the spectra of velocity and temperature spectra decreases on a smaller range of frequencies compared to the pure convective ones. We also notice that the existence range of $-5/3$ Kolmogorov power law is notably reduced in the spectra at the point A_2. It can be deduced that gas radiation reduces the appearance of both thermal and dynamic small-scale structures in the flow. Besides, the -3 power law is always present in the θ-spectra, but appears earlier for cases (B) and (C) at point A_2 when compared to pure convection. It suggests that gas radiation affects the conversion of the potential energy into kinetic energy and produces less chaos in the far field of the plume. At point B_2, located in the plume plane, the frequency domains of the spectra are slightly broader than at point A_2 for all the three cases, revealing a higher turbulence level in the plume plane despite the radiation effects.

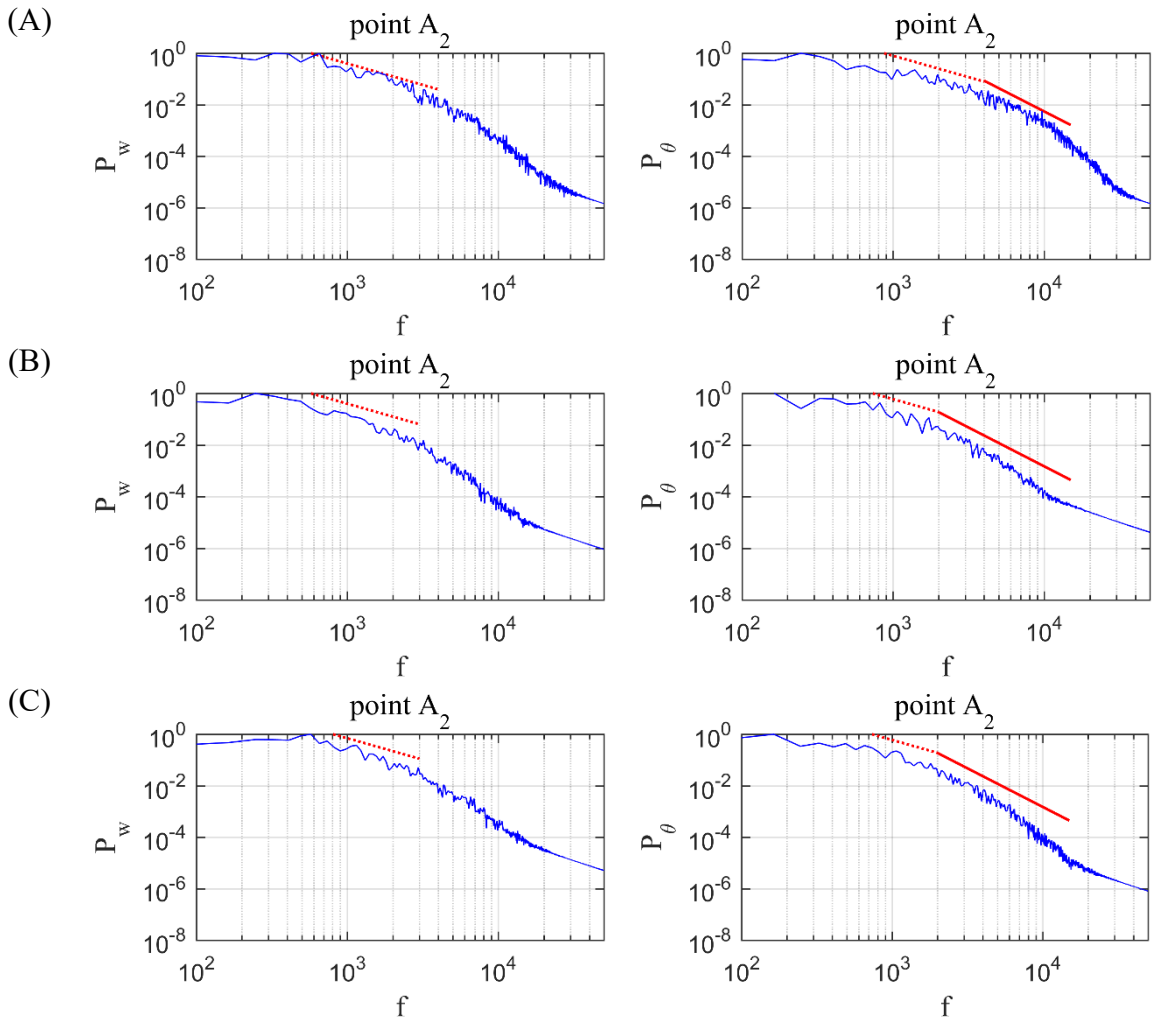

Figure 4.43. $Ra = 10^9$. Density power spectra of velocity components w and temperature θ at the point A_2. Dotted trendline: -5/3 power law, solid trendline: -3 power law.

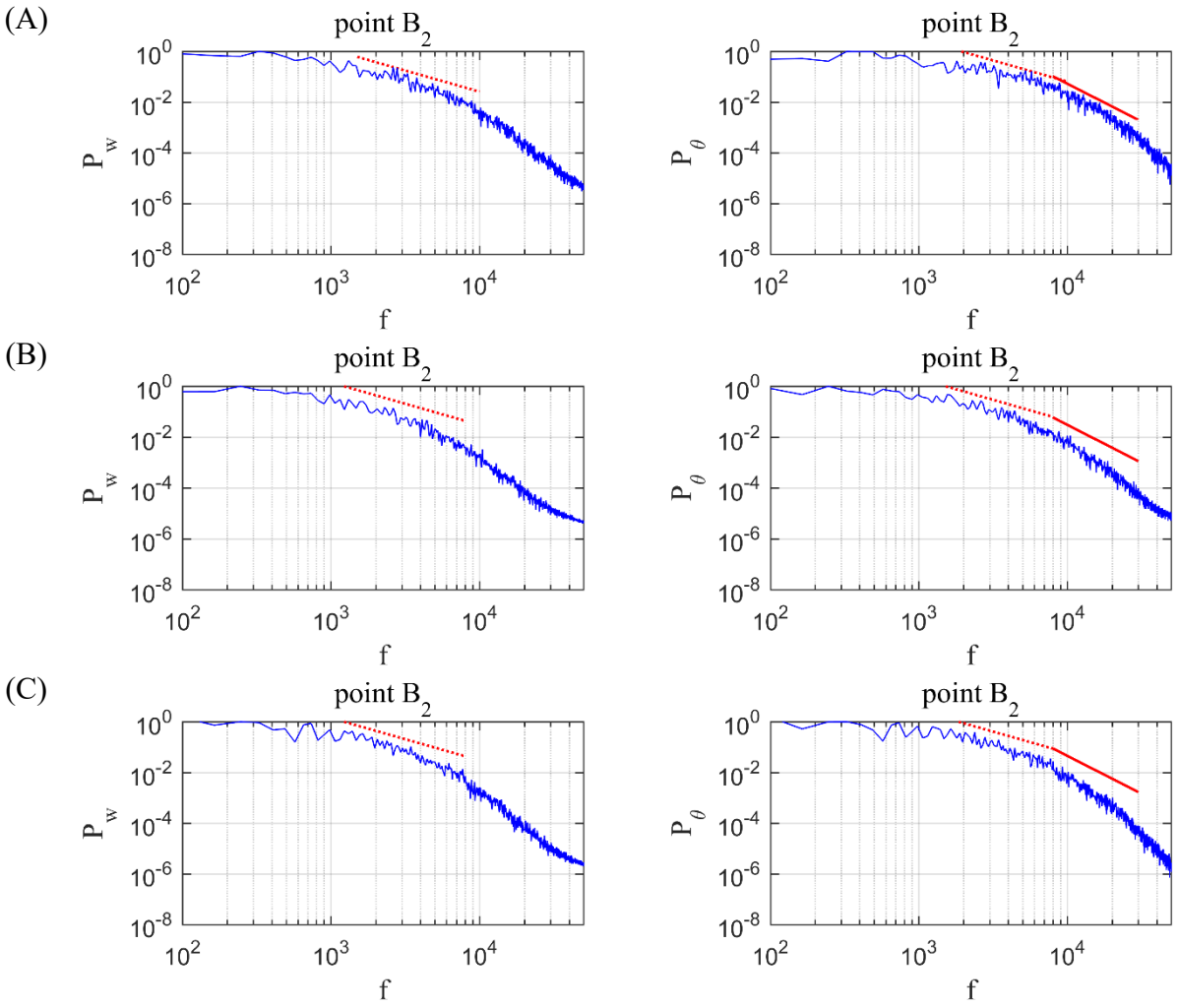

Figure 4.44. $\mathrm{Ra} = 10^9$. Density power spectra of velocity components w and temperature θ at the point B_2. Dotted trendline: -5/3 power law, solid trendline: -3 power law.

4.5 Transfers at the walls

In order to investigate the evolution of the relative influence between convection and radiation in the thermal transfers at the top and bottom walls, the radiative and convective Nusselt numbers are compared in Figure 4.45 and Figure 4.46 at the different Rayleigh numbers considered for the cases: (A) pure convection; (B) gray gas ($\tau = 0.1$) and (C) real gas mixture ($X_a = 2\%$ and $T_{ref} = 300$ K). We remind that in all the cases, the total of the heat exchanges at the walls equals 1. For case (A), the convective flux increases at the top wall and decreases at the bottom wall with increasing Rayleigh numbers. When radiation is accounted for (cases B and C), the total radiative transfers are higher than the convective ones in a first step, but when Ra is increased, the convective transfers grow up and progressively exceed the radiative ones. This occurs at $\mathrm{Ra} \approx 5\times10^8$ for the gray gas (case B) and at $\mathrm{Ra} \approx 9\times10^7$ for the real gas (case C).

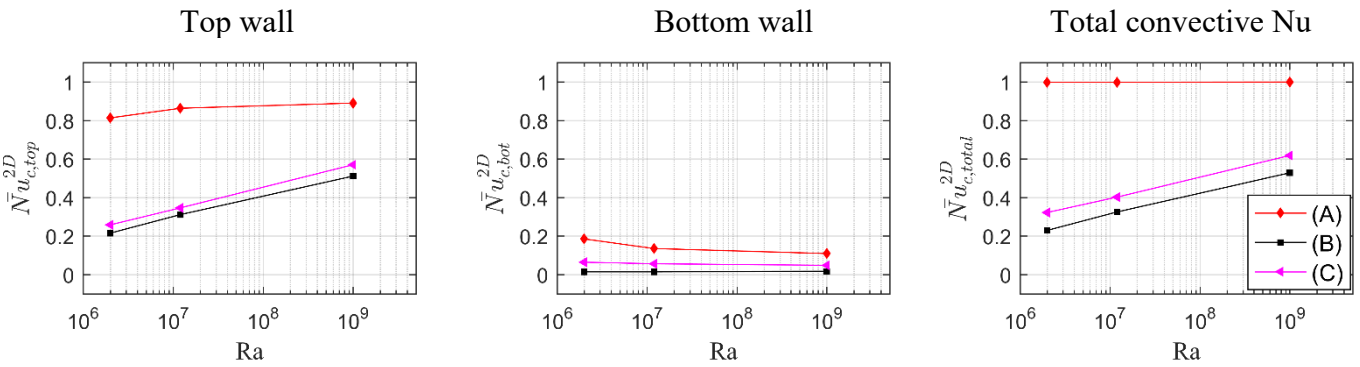

Figure 4.45. Convective Nusselt number at the top and bottom walls, and the total convective Nusselt number at different Rayleigh numbers for the three cases.

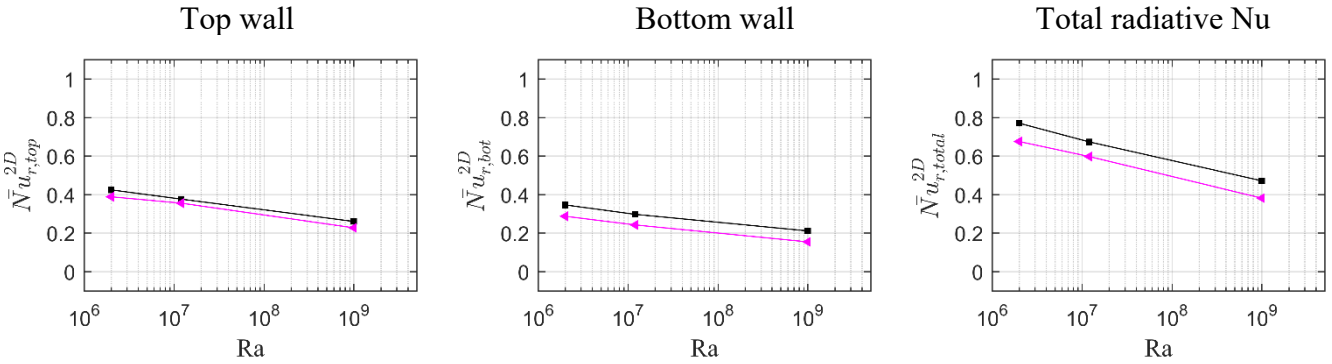

Figure 4.46. Radiative Nusselt number at the top and bottom walls, and the total radiative Nusselt number at different Rayleigh numbers for cases (B) and (C).

4.6 Conclusion

In this chapter, the convection-radiation coupling was simulated in different gas media, and it was found that the gas radiation effects on thermal and kinetic fields of plume depends on the flow regime. For steady state flow, gas radiation tends to reduce the spatial spreading of the thermal plume and to homogenize the temperature field away from the heat source. Gas radiation also results in a weakening of the global circulation and then delays the transition to unsteadiness.

For transient state, gas radiation greatly decreases the time oscillation amplitude as well as the associated frequency. The time-averaged results of the unsteady flows show that gas radiation still weakens the thermal field of the plume, but has little effects on the mean kinetic field. Nevertheless, the flow is accelerated in the central core of the plume for the optically thinner media ($\tau = 0.1$ and real gas), and decelerates for optically thicker ones ($\tau = 0.2$ and 0.5), compared to the pure convective situation.

For turbulent regime, accounting for radiation leads to a less chaotic behavior of the plume, compared to pure convection. Radiative heat transfer induces a smoothing of the mean temperature field in most of the cavity, except in the region around the heat source, where

the maximum temperature slightly increases. Moreover, the reinforcement of flow dynamics observed in the transitional case is also observed in turbulent plume.

Conclusions and perspectives

The general objective of this thesis was to characterize the evolution of a 3D confined plume from steady state to turbulent behavior, and to assess a better understanding and prediction of the influence of gas radiation on the thermal plume in different flow regimes: steady, transitional and turbulent. Different gas media were studied in this work: transparent medium, gray gas approximation and real gaseous mixture (dry air - water vapor). The numerical approach based on the CFD SUNFLUIDH code coupled to the ROCCOCO radiative module proved to be efficient to deal with radiation-convection problems, and simulations were carried out for a range of Rayleigh number varying from 10^6 up to 10^9.

Main conclusions

The pure convective case (i.e. neither gas nor wall radiation) was investigated first. The plume behavior was examined in different flow regimes. For steady state flows, two symmetrical fluid loops are formed in the cavity. In each transverse plane of this 3D cubic cavity, the thermal and kinetic properties of the flow are very similar to those of the 2D case in the most part of the cavity, excepting the regions close to the front and rear walls. By increasing the Rayleigh number, the transition to unsteadiness occurs through a supercritical Hopf bifurcation, which is more than a decade before that in the 2D case. In the succeeding time periodic regime, the flow structure combines an antisymmetric stationary plane wave along the heat source direction with respect to the vertical mid-plane and a swaying motion of the plume in each transverse plane with respect to the vertical centerline. Then, turbulent behavior was studied at $\mathrm{Ra} = 10^9$. The plume is first laminar just above the heat source, and then undergoes a transition with the creation of small structures in the upper part of the cavity where the plume becomes fully turbulent. The well-known -5/3 Kolmogorov power law is shown in the velocity and temperature spectra, followed by a -3 power law due to the turbulent thermal dissipation.

The influence of gas radiation was then studied by introducing different gaseous media: fictious gray gases with various optical thickness and real gaseous mixture (dry air - water vapor). Simulations of convection-radiation coupled phenomena were performed in the same range of Rayleigh numbers than for the pure convective case.

In steady regime, gas radiation tends to homogenize the temperature field away from the source. This leads to a decrease of the spatial extension of the thermal plume and to a progressive disappearing of the thermal jet impingement at the roof. Gas radiation also induces a weakening of the global circulation and then delays the transition to unsteadiness. The heat transfer at the isothermal walls is strongly affected by gas radiation, and the radiative flux becomes the dominant mode of heat exchange. By using the gray gas approximation, it was found that the increase of the optical thickness enhances gas radiation effects on the thermal plume. Next, for the real gas mixture, a parametric study conducted for water vapor concentration and reference temperature, confirms that the optically thicker is the medium, the stronger is the attenuation of the thermal and kinetic fields of the flow.

For the transitional pure convective situation ($\mathrm{Ra} = 1.2\times10^{7}$), the increase of the optical thickness produces successively periodic flow and steady flow, instead of the chaotic behavior observed in pure convection. This indicates again that gas radiation stabilizes the plume flow and delays the transition to unsteadiness. When periodic flows are observed for both gray and real gases, the fundamental frequency and the oscillation amplitude decrease with the growth of the optical thickness. Once again, gas radiation reduces the spatial extension of the thermal plume and homogenizes the mean temperature field, but contrarily to the steady state results, the structure of the mean kinetic field is almost unchanged. Nevertheless, gas radiation leads to an acceleration of the fluid for the thinner optical media, and to a deceleration for optically thicker ones.

In turbulent regime ($\mathrm{Ra} = 10^{9}$), the distribution of the vortex structures shows that the chaotic behavior of the plume is reduced with radiative participating media. Due to radiation effects, both thermal and mechanical RMS fluctuations are decreased in the downstream recirculation region after the impingement on the top wall. A weakening of the mean thermal field is observed in radiative participating media, except at the heat source location where the maximum temperature grows. Gas radiation also reinforces the dynamics of the mean flow above the source, as observed in the transitional case.

Perspectives

Extending the study of the influence of water vapor concentration to turbulent plumes can be a future extension of this work in order to consider a more pronounced influence of radiation on the turbulent regime. This could be done, as an example by considering a real gas mixture with higher water vapor concentration (for example $X_a = 10\%$) at the reference temperature $T_{ref} = 500$ K and at the same injected energy Q'_s.

Another perspective is the investigation of gas radiation effects on double-diffusive plume in a real gas mixture. The double-diffusive phenomenon has already been investigated in the

case of a differentially heated cavity. Moufekkir et al. (2012), as an example, studied numerically the double diffusion in a differentially heated square cavity filled with a binary gray gas. They observed that, when the solutal buoyancy is dominant, the influence of radiation is considerable on the thermal field and negligible on the kinetic and concentration fields. However, when thermal buoyancy is dominant, radiation influences significantly the flow structure, as well as the concentration and the temperature fields. In the same configuration, Laouar-Meftah et al. (2014) studied the double-diffusive convection in an air-H_2O mixture. They found that the variation of the gas absorption with the local concentration of H_2O induces a strong coupling between the concentration and thermal fields. These works proved that radiation has an important influence on double diffusive convection, and this comprehensive problem is worth studying.

There is also a need to carry out simulations for more realistic of practical situations, at higher Rayleigh numbers and/or temperature differences. This requires to use alternative approaches to DNS. Large Eddy Simulation (LES) is an attractive choice in reducing the computational effort, and has yet been applied to turbulent thermal plumes (Bastiaans et al., 2000; Zhou et al., 2001; Pham et al., 2007; Yan, 2007). However, compared to DNS, LES approach requires the modelling of the sub-grid scales, so it is necessary to evaluate the performance of different sub-grid models, with potentially, the influence of the radiative heat transfer on the small scale.

Appendix A
Numerical simulations parameters

This appendix serves to provide the lists of the simulations presented in this work, and also to give the numerical parameters applied in simulations of pure convective case and convection-radiation coupling.

A.1 Simulations of pure convective case

The parameters of the numerical simulations in pure convection for 2D and 3D cases at the different regimes are reported in Table A.1. The simulations of 2D configuration are studied in section 2.2.1 to validate the numerical code, while those of 3D configuration are analyzed in Chapter 3. In 3D configuration, the spatial discretization, chosen for the $10^6 < \mathrm{Ra} < 1.2\times10^7$ range, is consistent with those of 2D configuration. For the highest Ra number ($\mathrm{Ra} = 10^9$), a non-uniform mesh is used to refine the regions near the lateral walls and the heat source, and the parameters applied in mesh are detailed in section 3.1. All simulations were carried out with a fixed timestep which corresponds to a maximum of CFL number of 0.45.

Dimension	Regime	Ra	Mesh	Timestep	Initial solution
2D	Steady	10^6	129×129	2.0×10^{-5}	$u_i = 0,\ \theta = 0$
		2.7×10^7	129×129	5.0×10^{-6}	10^6 -2D converged
	Periodic	2.81×10^7	129×129	5.0×10^{-6}	2.7×10^7 -2D converged
3D	Steady	10^6	$(3\times43)\times(3\times43)\times129$	2.0×10^{-5}	$u_i = 0,\ \theta = 0$
	Periodic	1.2×10^6	$(3\times43)\times(3\times43)\times129$	2.0×10^{-5}	$u_i = 0,\ \theta = 0$
	Transitional	2×10^6	$(3\times43)\times(3\times43)\times129$	1.6×10^{-5}	10^6 -3D converged
		5×10^6	$(3\times43)\times(3\times43)\times129$	1.0×10^{-5}	2×10^6 -3D converged
		1.2×10^7	$(3\times43)\times(3\times43)\times129$	7.5×10^{-6}	5×10^6 -3D converged
	Turbulent	10^9	$(4\times48)\times(4\times48)\times(4\times128)$	3.0×10^{-7}	10^8 -3D converged

Table A.1. List of simulations and numerical parameters in pure convective case.

A.2 Simulations of convection-radiation coupling

The parameters of the numerical simulations considering gas radiation, analyzed in Chapter 4, are shown in Table A.2. For unsteady flows, the dimensionless time period for obtaining the statistical values, Δt_{stat} , is given. The radiation and convection are solved on the same grids, but the radiative problem is solved every 5 convective time steps.

Ra	Case	Gas medium	τ	T_{ref} (K)	X_a	Regime	Mesh	Convective time step	Δt_{stat}	Initial solution
10^6	A	Transparent	0	-	-	Steady	$(3\times43)\times(3\times43)\times129$	2×10^{-5}	-	$u_i=0,\ \theta=0$
	B	Gray gas	0.1	-	-	Steady	$(3\times43)\times(3\times43)\times129$	2×10^{-5}	-	10^6 -A converged
	C	Gray gas	0.2	-	-	Steady	$(3\times43)\times(3\times43)\times129$	2×10^{-5}	-	10^6 -B converged
	D	Gray gas	0.5	-	-	Steady	$(3\times43)\times(3\times43)\times129$	2×10^{-5}	-	10^6 -C converged
(a) 2×10^6	A	Transparent	0	-	-	Transitional	$(3\times43)\times(3\times43)\times129$	1.6×10^{-5}	0.16	10^6 -A converged
	B	Gray gas	0.1	-	-	Steady	$(3\times43)\times(3\times43)\times129$	1.6×10^{-5}	-	(a) 2×10^6 -A converged
	C	Gray gas	0.2	-	-	Steady	$(3\times43)\times(3\times43)\times129$	1.6×10^{-5}	-	(a) 2×10^6 -B converged
	D	Gray gas	0.5	-	-	Steady	$(3\times43)\times(3\times43)\times129$	1.6×10^{-5}	-	(a) 2×10^6 -C converged
	E	Real gas	-	300	2%	Steady	$(3\times43)\times(3\times43)\times129$	1.6×10^{-5}	-	(a) 2×10^6 -A converged
(b) 2×10^6	A	Transparent	0	-	-	Transitional	$(3\times43)\times(3\times43)\times129$	1.6×10^{-5}	0.16	10^6 -A converged
	B	Real gas	-	500	2%	Steady	$(3\times43)\times(3\times43)\times129$	1.6×10^{-5}	-	(b) 2×10^6 -A converged
	C	Real gas	-	500	10%	Steady	$(3\times43)\times(3\times43)\times129$	1.6×10^{-5}	-	(b) 2×10^6 -B converged
	D	Real gas	-	500	20%	Steady	$(3\times43)\times(3\times43)\times129$	1.6×10^{-5}	-	(b) 2×10^6 -C converged
	E	Real gas	-	300	2%	Steady	$(3\times43)\times(3\times43)\times129$	1.6×10^{-5}	-	(b) 2×10^6 -A converged
1.2×10^7	A	Transparent	0	-	-	Transitional	$(3\times43)\times(3\times43)\times129$	7.5×10^{-6}	0.06	5×10^6 -A converged
	B	Gray gas	0.1	-	-	Periodic	$(3\times43)\times(3\times43)\times129$	7.5×10^{-6}	0.06	1.2×10^7 -A converged
	C	Gray gas	0.2	-	-	Periodic	$(3\times43)\times(3\times43)\times129$	7.5×10^{-6}	0.06	1.2×10^7 -B converged
	D	Gray gas	0.5	-	-	Steady	$(3\times43)\times(3\times43)\times129$	7.5×10^{-6}	-	1.2×10^7 -C converged
	E	Real gas	-	300	2%	Periodic	$(3\times43)\times(3\times43)\times129$	7.5×10^{-6}	0.06	1.2×10^7 -B converged
10^9	A	Transparent	0	-	-	Turbulent	$(4\times48)\times(4\times48)\times(4\times128)$	3.0×10^{-7}	0.09	10^8 -A converged
	B	Gray gas	0.1	-	-	Turbulent	$(8\times24)\times(8\times24)\times(8\times64)$	3.0×10^{-7}	0.09	10^9 -A converged
	C	Real gas	-	300	2%	Turbulent	$(8\times24)\times(8\times24)\times(8\times64)$	3.0×10^{-7}	0.09	10^9 -B converged

Table A.2. List of simulations and numerical parameters in convection-radiation coupling and compared to the pure convective case.

For convection-radiation coupled simulations, the RTE equation is solved by the DOM method. The convergence of the total number of discrete directions is confirmed in the case of gray gas at $\tau = 0.5$ and $\mathrm{Ra} = 10^6$ by comparing S_8- and S_{12}-approximation. Figure A.1 plots the volumetric radiative power along the lines $x = 0.5$ and $z = 0.5$ in the vertical mid-plane, implying that the S_8-approximation is sufficient for the discretization of the DOM method which is used for all simulations considering radiation.

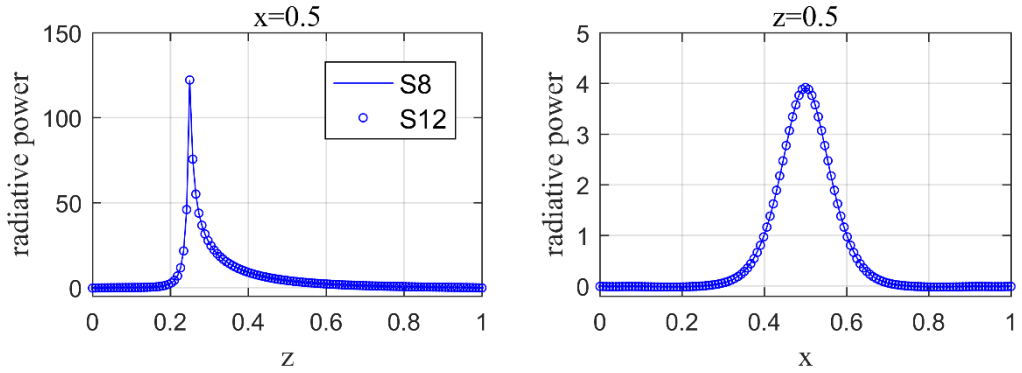

Figure A.1. Comparison of S_8- and S_{12}-approximation. Profiles of radiative power along the lines $x = 0.5$ and $z = 0.5$ at $\tau = 0.5$ and $\mathrm{Ra} = 10^6$.

In the cases of real gaseous mixture, various molar fractions X_a of water vapor in air are considered, as well as different reference temperatures T_{ref}. In order to predict radiative properties of gaseous mixtures, the SLW model is applied with a Lathrop scheme in this work. In the case of real gas at $T_{ref} = 300\mathrm{K}$, the radiative properties are estimated by considering 8 gray gases, including one clear component and seven others whose optical thickness varies in the range [0.01, 10^4]. As for the cases at $T_{ref} = 500\mathrm{K}$, the range for the 7 absorbing component is extended to $\tau \in [0.01, 10^5]$. Table A.3 reports the optical thickness of each gray gas using in SLW model.

T_{ref} (K)	X_a	τ_1	τ_2	τ_3	τ_4	τ_5	τ_6	τ_7	τ_8
300	2%	0	0.026	0.19	1.3	10	70	501	3612
500	2~10%	0	0.031	0.31	3.1	31	310	3100	31000

Table A.3. Optical thicknesses evaluated at the reference temperature for the SLW model.

Appendix B
SUNFLUIDH performances

The simulations presented in this work were completed by using a local machine for the $10^6 < \mathrm{Ra} < 1.2\times10^7$ range, or a supercomputer of Idris center for $\mathrm{Ra} = 10^9$, as reported in Table B.1. The calculating performance of code SUNFLUIDH is also given in Table B.1, according to the different gas media.

Gas medium	**Machine**	**Processors**		**Performance (s/(cell.timestep))**
Transparent	Local machine	2.0 GHz Intel Xeon(R) E5-26200	9	9.6×10^{-7}
Gray gas				1.5×10^{-6}
Real gas				5.9×10^{-6}
Transparent	Cluster Ada (Idris center)	2.67 GHz IBM x3750M4	64	4.6×10^{-8}
Gray Gas	Cluster Jean-zay (Idris center)	2.5 GHz Intel Cascade Lake 6248	512	1.4×10^{-8}
Real gas	Cluster Jean-zay (Idris center)	2.5 GHz Intel Cascade Lake 6248	512	7.4×10^{-8}

Table B.1. SUNFLUIDH performances.

References

Abdalla, I. E., Cook, M. J., & Hunt, G. R. (2009). Numerical study of thermal plume characteristics and entrainment in an enclosure with a point heat source. *Engineering Applications of Computational Fluid Mechanics*, 3(4):608-630.

Balsara, D. (2001). Fast and accurate discrete ordinates methods for multidimensional radiative transfer. Part I, basic methods. *Journal of Quantitative Spectroscopy Radiative Transfer*, 69(6):671-707.

Bastiaans, R. J. M., Rindt, C. C. M., Nieuwstadt, F. T. M., & Van Steenhoven, A. A. (2000). Direct and large-eddy simulation of the transition of two-and three-dimensional plane plumes in a confined enclosure. *International Journal of Heat and Mass Transfer*, 43(13):2375-2393.

Billaud, Y., Saury, D., & Lemonnier, D. (2017). Numerical investigation of coupled natural convection and radiation in a differentially heated cubic cavity filled with humid air. Effects of the cavity size. *Numerical Heat Transfer, Part A: Applications*, 72(7):495-518.

Cadet, L. (2015). Etude du couplage convection-rayonnement en cavité différentiellement chauffée à haut nombre de Rayleigh en ambiances habitables. *PhD thesis, La Rochelle University*.

Cadet, L., Joubert, P., Lemonnier, D., Fraigneau, Y., Sergent, A., & Saury, D. (2016). ROCOCO: Finite volume Navier-Stokes solver coupled with a DOM approach of RTE. *In French software Licensing Agency (APP)*.

Chandrasekhar, S. (1960). Radiative Transfer. *Dover Publications*.

Coelho, P. J. (2002). Numerical simulation of radiative heat transfer from non-gray gases in three-dimensional enclosures. *Journal of Quantitative Spectroscopy Radiative Transfer*, 74(3):307-328.

Collin, A., Boulet, P., Lacroix, D., & Jeandel, G. (2005). On radiative transfer in water spray curtains using the discrete ordinates method. *Journal of Quantitative Spectroscopy*, 92(1):85-110.

Colomer, G., Consul, R., & Oliva, A. (2007). Coupled radiation and natural convection: Different approaches of the SLW model for a non-gray gas mixture. *Journal of Quantitative Spectroscopy Radiative Transfer*, 107(1):30-46.

Colomer, G., Costa, M., Consul, R., & Oliva, A. (2004). Three-dimensional numerical simulation of convection and radiation in a differentially heated cavity using the discrete ordinates method. *International Journal of Heat and Mass Transfer*, 47(2):257-269.

Denison, M. K., & Webb, B. W. (1993). A spectral line-based weighted-sum-of-gray-gases model for arbitrary RTE solvers. *Journal of Heat Transfer*, 115(4):1004-1012.

Denison, M. K., & Webb, B. W. (1995). Development and application of an absorptionline blackbody distribution function for CO2. *International Journal of Heat and Mass Transfer*, 38(10):1813-1821.

Desrayaud, G., & Lauriat, G. (1993). Unsteady confined buoyant plumes. *Journal of Fluid Mechanics*, 252:617-646.

Draoui, A., Allard, F., & Beghein, C. (1991). Numerical analysis of heat transfer by natural convection and radiation in participating fluids enclosed in square cavities. *Numerical Heat Transfer, Part A: Applications*, 20(2):253-261.

Edwards, D. K. (1976). Molecular gas band radiation. *Advances in Heat Transfer*, 12:115-193.

Edwards, D. K., & Menard, W. A. (1964). Comparison of models for correlation of total band absorption. *Applied Optics*, 3(5):621-625.

Eichhorn, R., & Vedhanayagam, M. (1982). *The swaying frequency of line source plumes.* Paper presented at the Proc. Seventh International Heat Transfer Conf., Munich.

Fiscaletti, D., Angeli, D., Tarozzi, L., & Barozzi, G. S. (2013). Buoyancy-induced transitional flows around an enclosed horizontal cylinder: an experiment. *International Journal of Heat Mass Transfer*, 58(1-2):619-631.

Forstrom, R. J., & Sparrow, E. M. (1966). Experiments on the buoyant plume above a heated horizontal wire. *International Journal of Heat and Mass Transfer*, 10(3):321-331.

Fraigneau, Y. (2013). Principes de base des méthodes numériques utilisées dans le code SUNFLUIDH pour la simulation des écoulements incompressibles et à faible nombre de mach. *Tech. Rep. 2013-09*, LIMSI.

Fujii, T., Morioka, I., & Uehara, H. (1973). Buoyant plume above a horizontal line heat source. *International Journal of Heat and Mass Transfer*, 16(4):755-768.

Gebhart, B., Jaluria, Y., Mahajan, R. L., & Sammakia, B. (1988). *Buoyancy-induced flows and transport*. United States.

Geurts, B. J. (2003). *Elements of direct and large eddy simulation*. USA: R.T. Edwards, Inc.

Goody, R., West, R., Chen, L., Crisp, D., & Transfer, R. (1989). The correlated-k method for radiation calculations in nonhomogeneous atmospheres. *Journal of Quantitative Spectroscopy*, 42(6):539-550.

Goutiere, V., Liu, F., & Charette, A. (2000). An assessment of real-gas modelling in 2D enclosures. *Journal of Quantitative Spectroscopy and Radiative Transfer*, 64(3):299-326.

Grafsrønningen, S., & Jensen, A. (2017). Large eddy simulations of a buoyant plume above a heated horizontal cylinder at intermediate Rayleigh numbers. *International Journal of Thermal Sciences*, 112:104-117.

Grötzbach, G. (1983). Spatial resolution requirements for direct numerical simulation of the Rayleigh-Bénard convection. *Journal of Computational Physics*, 49(2):241-264.

Hartmann, J. M., Di Leon, R. L., & Taine, J. (1984). Line-by-line and narrow-band statistical model calculations for H2O. *Journal of Quantitative Spectroscopy and Radiative Transfer*, 32(2):119-127.

Hernández, R. H. (2015). Natural convection in thermal plumes emerging from a single heat source. *International Journal of Thermal Sciences*, 98:81-89.

Hirsch, C. (1998). *Numerical computation of internal and external flows: The fundamentals of computational fluid dynamics*. USA: Elsevier.

Hottel, H. C., & Sarofim, A. F. (1967). *Radiative transfer*. New York: McGraw-Hill.

Howell, J. R. (1969). Application of Monte Carlo to heat transfer problems. In *Advances in Heat Transfer* (Vol. 5, pp. 1-54): Elsevier.

Hunt, J. C. R., Wray, A. A., & Moin, P. (1988). Eddies, streams, and convergence zones in turbulent flows. *Center for Turbulence Research Report CTR-S88*:193-208.

Ibrahim, A., Saury, D., & Lemonnier, D. (2013). Coupling of turbulent natural convection with radiation in an air-filled differentially-heated cavity at Ra=1.5×109. *Computers & Fluids*, 88:115-125.

Jeans, J. H. (1917). The equations of radiative transfer of energy. *Monthly Notices of the Royal Astronomical Society*, 78:28-36.

Jiménez, J. (2003). Computing high-reynolds-number turbulence: will simulations ever replace experiments? *Journal of Turbulence*, 4(22):1-14.

Kaczorowski, M., & Wagner, C. (2009). Analysis of the thermal plumes in turbulent Rayleigh–Bénard convection based on well-resolved numerical simulations. *Journal of Fluid Mechanics*, 618:89-112.

Kim, T. K., Menart, J. A., & Lee, H. S. (1991). Nongray radiative gas analyses using the SN discrete ordinates method. *Journal of Heat Transfer*, 113(4):946-952.

Kotsovinos, N. E. (1991). Turbulence spectra in free convection flow. *Physics of Fluids A: Fluid Dynamics*, 3(1):163-167.

Landau, L. D. (1944). *On the problem of turbulence.* Paper presented at the Dokl. Akad. Nauk USSR.

Laouar-Meftah, S., Cherifi, M., Lemonnier, D., & Benbrik, A. (2014). Gas radiation effects on opposing double-diffusive convection in a non-gray air–H2O mixture. *International Journal of Thermal Sciences*, 77:38-46.

Lari, K., Baneshi, M., Nassab, S. G., Komiya, A., & Maruyama, S. (2011). Combined heat transfer of radiation and natural convection in a square cavity containing participating gases. *International Journal of Heat and Mass Transfer*, 54(23-24):5087-5099.

Lathrop, K. D. (1969). Spatial differencing of the transport equation: positivity vs accuracy. *Journal of Computational Physics*, 4(4):475-498.

Lauriat, G. (1982). Combined radiation-convection in gray fluids enclosed in vertical cavities. *Journal of Heat Transfer*, 104(4):609-615.

Lesieur, M. (1990). *Turbulence in fluids*: Kluwer academic publishers.

Liñán, A., & Kurdyumov, V. N. (1998). Laminar free convection induced by a line heat source, and heat transfer from wires at small Grashof numbers. *Journal of Fluid Mechanics*, 362:199-227.

Liu, F., Gülder, Ö. L., Smallwood, G. J., & Ju, Y. (1998). Non-grey gas radiative transfer analyses using the statistical narrow-band model. *International Journal of Heat and Mass Transfer*, 41(14):2227-2236.

Lyakhov, Y. N. (1970). Experimental investigation of free convection above a heated horizontal wire. *Journal of Applied Mechanics and Technical Physics*, 11(2):355-359.

McCracken, M., & Marsden, J. E. (1976). *The Hopf bifurcation and its applications*. New York: Springer-Verlag.

Modest, M. F. (2003). *Radiative heat transfer*. Boston: Academic press.

Moufekkir, F., Moussaoui, M. A., Mezrhab, A., Naji, H., & Bouzidi, M. (2012). Numerical study of double diffusive convection in presence of radiating gas in a square cavity. *Fluid Dynamics Materials Processing*, 8(2):129-153.

Pera, L., & Gebhart, B. (1971). On the stability of laminar plumes: some numerical solutions and experiments. *International Journal of Heat and Mass Transfer*, 14(7):975-984.

Pham, M. V., Plourde, F., & Doan, K. S. (2007). Direct and large-eddy simulations of a pure thermal plume. *Physics of Fluids*, 19(12):125103.

Rivière, P., Soufiani, A., Perrin, M. Y., Riad, H., & Gleizes, A. (1996). Air mixture radiative property modelling in the temperature range 10,000–40,000 K. *Journal of Quantitative Spectroscopy Radiative Transfer*, 56(1):29-45.

Rouse, H., Yih, C. S., & Humphreys, H. W. (1952). Gravitational convection from a boundary source. *Tellus*, 4:201-210.

Saury, D., Rouger, N., Djanna, F., & Penot, F. (2011). Natural convection in an air-filled cavity: Experimental results at large Rayleigh numbers. *International Communications on Heat & Mass Transfer*, 38(6):679-687.

Schmidt, W. (1941). Turbulent propagation of a stream of heated air. *ZAMM-Journal of Applied Mathematics and Mechanics*, 21:265-278.

Schorr, A. W., & Gebhart, B. (1970). An experimental investigation of natural convection wakes above a line heat source. *International Journal of Heat and Mass Transfer*, 13(3):557-571.

Solovjov, V. P., Lemonnier, D., & Webb, B. W. (2014). Extension of the exact SLW model to non-isothermal gaseous media. *Journal of Quantitative Spectroscopy & Radiative Transfer*, 143:83-91.

Soucasse, L., Rivière, P., & Soufiani, A. (2013). Monte Carlo methods for radiative transfer in quasi-isothermal participating media. *Journal of Quantitative Spectroscopy & Radiative Transfer*, 128:34-42.

Soucasse, L., Rivière, P., & Soufiani, A. (2016). Natural convection in a differentially heated cubical cavity under the effects of wall and molecular gas radiation at Rayleigh numbers up to 3×109. *International Journal of Heat and Fluid Flow*, 61:510-530.

Soucasse, L., Rivière, P., Xin, S., Le Quéré, P., & Soufiani, A. (2012). Numerical study of coupled molecular gas radiation and natural convection in a differentially heated cubical cavity. *Computational Thermal Sciences*, 4(4).

Soufiani, A., & Taine, J. (1987). Application of statistical narrow-band model to coupled radiation and convection at high temperature. *International Journal of Heat and Mass Transfer*, 30(3):437-447.

Soufiani, A., & Taine, J. (1997). High temperature gas radiative property parameters of statistical narrow-band model for H2O, CO2 and CO, and correlated-K model for H2O and CO2. *International Journal of Heat and Mass Transfer*, 40(4):987-991.

Turner, J. S. (1986). Turbulent entrainment: the development of the entrainment assumption, and its application to geophysical flows. *Journal of Fluid Mechanics*, 173:431-471.

Urakawa, K., Morioka, I., & Kiyota, M. (1983). *Swaying motion of the buoyant plume above a horizontal line heat source.* Paper presented at the Proc. 1st ASME-JSME Thermal Engineering Conf., Honlulu. HI.

Versteeg, H. K., & Malalasekera, W. (2007). *An introduction to computational fluid dynamics: the finite volume method*: Pearson education.

Vincent, A. P., Yuen, D. A., Munger, D., & Zhu, G. (2012). On the dynamics of 3-D single thermal plumes at various Prandtl numbers and Rayleigh numbers. *Geophysical Astrophysical Fluid Dynamics*, 106(2):138-156.

Xin, S., Duluc, M.-C., Lusseyran, F., & Le Quéré, P. (2004). Numerical simulations of natural convection around a line-source. *International Journal of Numerical Methods for Heat & Fluid Flow*, 14(7):830-850.

Yan, Z. H. (2007). Large eddy simulations of a turbulent thermal plume. *Heat and Mass Transfer*, 43(6):503-514.

Yücel, A., Acharya, S., & Williams, M. L. (1989). Natural convection and radiation in a square enclosure. *Numerical Heat Transfer, Part A: Applications*, 15(2):261-278.

Zeldovich, Y. B. (1937). Limiting laws of freely rising convection currents. *Zh. Eksp. Teor. Fiz.*, 7(12):1463-1465.

Zhou, X., Luo, K. H., & Williams, J. J. R. (2001). Large-eddy simulation of a turbulent forced plume. *European Journal of Mechanics B-Fluids*, 20(2):233-254.

Simulations numériques de panaches thermiques dans une cavité confinée en présence de couplage convection-rayonnement volumique

Résumé :

Ce travail est une étude numérique d'un panache thermique confiné en présence de rayonnement de gaz. Le panache est généré par une source de chaleur linéaire immergée dans une cavité cubique remplie d'air. Le but principal est de caractériser l'évolution du panache tout au long de sa transition depuis le régime stationnaire jusqu'à la turbulence, et d'explorer les effets du rayonnement de gaz sur la stabilité, les transferts de chaleur, les champs thermiques et cinétiques du panache.

Les simulations numériques DNS sont effectuées pour des nombres de Rayleigh de 10^6 à 10^9 avec un logiciel CFD de volumes finis couplé à un module de transferts radiatifs. La situation de convection pure est étudiée en premier lieu pour caractériser les champs thermiques et cinétiques du panache dans différents régimes d'écoulement. Ensuite, le couplage convection-rayonnement est introduit en considérant un gaz gris ou un gaz réel (mélange air – vapeur d'eau). Les effets de l'épaisseur optique sont analysés en détail pour le modèle de gaz gris. Les résultats montrent que le rayonnement stabilise le panache et retarde la transition à l'instationnarité. Le rayonnement homogénéise également le champ thermique et réduit l'extension spatiale du panache. Cependant, l'effet sur le champ cinétique dépend du régime d'écoulement. A l'état stationnaire, le rayonnement de gaz diminue la circulation globale tandis que pour les états transitoires et turbulents, il augmente la dynamique de l'écoulement pour des milieux optiques minces. Ces tendances générales sont confirmées pour le mélange de gaz réel par une étude paramétrique de la concentration de vapeur d'eau et de la température de référence.

Mots clés : panache thermique, couplage convection-rayonnement de gaz, modèle de gaz réel, DNS, transition à l'instationnarité, turbulence

Numerical study of a confined thermal plume at different flow regimes under the influence of gas radiation

Summary :

This work presents a numerical investigation of a confined thermal plume under the influence of gas radiation. Plume flow is generated by a linear heat source of constant power density immersed in a cubic cavity. The main aim of this thesis is to characterize the evolution of the plume throughout its transition from steady-state to turbulent regime, and to explore the gas radiation effects on flow stability, heat transfers, thermal and kinetic fields of the plume.

DNS numerical simulations are performed over a Rayleigh number range from 10^6 to 10^9 by applying a finite volume CFD software coupled to a module for radiative heat transfer calculations. The pure convective situation is studied first to characterize the thermal and kinetic fields of the plume in different flow regimes. Next, the convection-radiation coupling is introduced by considering either gray gas or real gas (air - H2O mixture) media. The effects of optical thickness are analyzed in details for gray gas model. Results show that gas radiation stabilizes the plume flow and delays the onset of unsteadiness. Gas radiation also homogenizes the thermal field and reduces its spatial spreading. However, radiation effect on the kinetic field depends on the flow state. For steady state, gas radiation decreases the global flow circulation while for transient and turbulent states, it enhances the flow dynamics in optically thin medium. These general trends of radiation are also confirmed in real gas mixture through a parametric study of water vapor concentration and reference temperature.

Keywords : thermal plume, convection-radiation coupling, gas radiation, real gas model, DNS, transition to unsteadiness, turbulence

La Rochelle Université

LaSIE
(Laboratoire des Sciences de l'Ingénieur pour l'Environnement)
UMR CNRS 7356, Avenue Michel Crépeau
17042 LA ROCHELLE CEDEX

LaSIE UMR CNRS 7356 Université La Rochelle